

## ABSTRACT

SHEN, CHEN. Design of Acoustic Metamaterials and Metasurfaces. (Under the direction of Dr. Yun Jing).

Acoustic metamaterials are artificially engineered materials or structures that exhibit exotic properties which do not exist in nature. The recent emergence of acoustic metasurfaces, as a sub-genre of acoustic metamaterials, opens up new possibilities in controlling acoustic waves. They are subwavelength acoustic surfaces/screens that are commonly associated with unique transmission/reflection behavior. Numerous novel or improved applications have been realized by acoustic metamaterials and metasurfaces which are otherwise difficult or impossible to achieve with conventional structures.

In this thesis, we start from two unique types of acoustic metamaterial, namely negative density acoustic metamaterials and negative modulus acoustic metamaterials. The negative effective density is introduced by periodically arranged plates in a waveguide and the negative effective modulus stems from open-ended side holes. The underlying physics of negative effective density and modulus are studied. Also, we present a design of utilizing multiple branch openings to broaden the bandwidth of side-branch based negative modulus metamaterials. A lumped model is developed for theoretical analysis and as much as 100% increase over the traditional single branch opening structure in bandwidth is achieved.

By placing plates in only one direction, a broadband acoustic hyperbolic metamaterial can be formed, where opposite signs of effective density in the  $x$  and  $y$  directions are achieved below a certain cutoff frequency. The hyperbolic dispersion relation is obtained by calculating the effective densities along orthogonal directions and numerical simulations. Partial focusing and subwavelength imaging are demonstrated both

numerically and experimentally at frequencies between 1.0 and 2.5 kHz. The effect of material loss in the plates is also studied.

Furthermore, by combining the two types of acoustic metamaterials, an anisotropic complementary metamaterial can be realized, which leads to dramatically reduced acoustic field distortion and enhanced sound transmission through aberrating layers with proper designs. In the example where a focused beam is studied, the acoustic intensity at the focus is increased from 28% to 88% of the intensity in the control case which is in the absence of the aberrating layer and the complementary metamaterial. The potentials of acoustic cloaking and canceling out multiple aberrating layers are also studied numerically.

In the acoustic metasurfaces part, two kinds of acoustic metasurfaces with different functionalities are designed and experimentally verified. A design of acoustic metasurfaces yielding asymmetric transmission within a certain frequency band is presented, which consists of a layer of gradient-index metasurface and a layer of near-zero index metasurface. Numerical simulations and experiments are carried out to verify this phenomenon. In another particular example of acoustic metasurfaces, they are used to construct an acoustic hologram. A series of unit cells are designed and are able to modulate the transmitted phase across the cells. With an iteration-based algorithm, certain images can be formed by manipulating the acoustic phase across the hologram. We propose the design and experimental demonstration of an acoustic hologram and a multifocus lens.

© Copyright 2016 Chen Shen

All Rights Reserved

Design of Acoustic Metamaterials and Metasurfaces

by  
Chen Shen

A dissertation submitted to the Graduate Faculty of  
North Carolina State University  
In partial fulfillment of the  
Requirements for the degree of  
Doctor of Philosophy

Mechanical Engineering

Raleigh, North Carolina

2016

APPROVED BY:

---

Dr. Yun Jing  
Committee Chair

---

Dr. Steven A. Cummer

---

Dr. Paul I. Ro

---

Dr. Richard Keltie

## BIOGRAPHY

Chen Shen was born on Dec 18, 1989 in Wuhan, Hubei Province, China. He graduated from No.1 Middle School affiliated to Central China Normal University in 2008 and in the same year, he was admitted to Nanjing University, Jiangsu, China in department of acoustics. In 2012, He was admitted to the direct doctoral program in Department of Mechanical and Aerospace Engineering in North Carolina State University. Under the direction of Dr. Yun Jing, he conducted research in acoustic metamaterials. In 2014, he received a MS degree from Mechanical Engineering.

## Publications

- Yangbo Xie\*, **Chen Shen**\*, Wenqi Wang, Junfei Li, Dingjie Suo, Bogdan-Ioan Popa, Yun Jing, and Steven A. Cummer, 2D acoustic Metasurface for Holographic Reconstruction, (\*co-first author, under review, 2016).
- **Chen Shen** and Yun Jing, Loss-induced enhanced transmission in anisotropic density-near-zero acoustic metamaterials, (under review, 2016).
- Tai-Yun Huang, **Chen Shen** and Yun Jing, On the Evaluation of Effective Density for Plate- and Membrane-type Acoustic Metamaterials Without Mass Attached, *J. Acoust. Soc. Am.* **140**, 908 (2016).
- **Chen Shen**\*, Yangbo Xie\*, Junfei Li, Steven A. Cummer, and Yun Jing, Acoustic Metasurfaces for Asymmetric Transmission, *Appl. Phys. Lett.* **108**, 223502 (2016). (\*co-first author)
- Tai-Yun Huang, **Chen Shen** and Yun Jing, Membrane- and Plate-type Acoustic Metamaterials, *J. Acoust. Soc. Am.* **139**, 3240 (2016).
- **Chen Shen**, Yangbo Xie, Ni Sui, Wenqi Wang, Steven A. Cummer, and Yun Jing, Broadband Acoustic Hyperbolic Metamaterial, *Phys. Rev. Lett.* **115**, 254301 (2015).
- **Chen Shen**, Jun Xu, Nicholas X. Fang, and Yun Jing, Anisotropic Complementary Acoustic Metamaterial for Canceling out Aberrating Layers, *Phys. Rev. X* **4**, 041033 (2014).
- **Chen Shen** and Yun Jing, Side branch-based acoustic metamaterials with a broad-band negative bulk modulus, *Appl. Phys. A.* **117**, 1885 (2014).

## ACKNOWLEDGEMENTS

Foremost, I would like to express my sincere gratitude to my advisor Dr. Yun Jing for his continuous support and help for my Ph.D. study and research. His guidance, knowledge, enthusiasm, and encouragement have been a great aid throughout my Ph.D. study. He also gave me the freedom to pursue various research projects with different directions. It helped me a lot to build my research ability and the interest of exploring the unknowns. I can never have earned my doctoral degree without his patience and insightful discussions he provided. It is my great honor and pleasure to have the opportunity to work with him and have his guidance on my research and career.

I would also like to express my sincere appreciation to the other committee members, Dr. Steven A. Cummer, Dr. Paul I. Ro, Dr. Richard Keltie, and Dr. Don Brenner, who had offered me invaluable suggestions in my dissertation and research. Special thanks to Dr. Steven A. Cummer, who had provided me great research opportunities and freedom to conduct experiments and work with people in Duke University.

I would like to thank Mr. Yangbo Xie for all the discussions and generous help on my research and the friendship we share. Special thanks to Dr. Yong Li, Dr. Xiang Yan, Dr. Rui Zhu, Dr. Nicholas Fang, Dr. Jun Xu, Ms. Wenqi Wang, Mr. Junfei Li, Dr. Bogdan Popa, Mr. Xun Wu, Mr. Sibol Li, Mr. Xiao Zhang for their help and suggestions.

I also want to thank my colleagues in the Acoustics and Ultrasonics Lab for their continuous help and the happy time we spent together: Mr. Tianren Wang, Mr. Neeraj Gole, Mr. Dingjie Suo, Mr. Tai-Yun Huang, Mr. Sean Maguire, Mrs. Ni Sui, Ms. Juanjuan Gu, and Mr. Yong Yang.

Last but not least, my deepest gratitude to my parents and my wife for their generous love and support, especially for these years of studying abroad.

## TABLE OF CONTENTS

LIST OF FIGURES .....	vi
LIST OF TABLES .....	x
Chapter 1 Introduction.....	1
1.1 Acoustic Metamaterials and Metasurfaces .....	1
1.2 Research Motivation and Objective .....	4
Chapter 2 Acoustic Metamaterial with Negative Modulus .....	7
2.1 Side-branch Based Acoustic Metamaterial.....	7
2.2 Multiple Branch Openings for Broader Bandwidth .....	9
2.2.1 Lumped Model .....	9
2.2.2 Numerical Simulations .....	15
2.3 Summary .....	21
Chapter 3 Acoustic Metamaterial with Negative Density .....	22
3.1 Membrane- and Plate-type Acoustic Metamaterials.....	23
3.2 Hyperbolic Acoustic Metamaterial.....	27
3.2.1 Hyperbolic Dispersion Relation .....	28
3.2.2 Negative Refraction.....	32
3.2.3 Partial Focusing and Subwavelength Imaging .....	34
3.3 Material Loss in Anisotropic Density Near-zero Metamaterials.....	43
3.3.1 Loss-induced Enhanced Transmission .....	44
3.3.2 Numerical Simulations .....	47
3.4 Summary .....	51
Chapter 4 Complementary Acoustic Metamaterial .....	53
4.1 Background and Motivation .....	54
4.2 Anisotropic Complementary Metamaterial .....	55
4.2.1 Transformation Acoustics .....	56
4.2.2 Structure Design .....	62
4.2.3 Numerical Simulations .....	66
4.3 Summary .....	74
Chapter 5 Acoustic Metasurfaces with Asymmetric Transmission.....	75
5.1 Gradient-index Metasurface and Near-zero Index Metasurface.....	76
5.2 Simulation and Measurement Results .....	79

5.3	Summary .....	86
Chapter 6 Acoustic Hologram Based on Metasurfaces .....		88
6.1	Weighted Gerchberg-Saxton Algorithgm.....	89
6.2	Acoustic Hologram with Phase Modulation.....	91
6.2.1	Characterization of the Unit Cells .....	92
6.2.2	Numerical Simulations .....	94
6.2.3	Experimental Results.....	98
6.3	Multifocus Lens.....	102
6.4	Summary .....	104
Chapter 7 Concluding Remarks and Future Work .....		106
7.1	Conclusions and Contributions.....	106
7.2	Future Work .....	107
BIBLIOGRAPHY .....		109
APPENDICES.....		118
A.	Description of the finite difference method for the effective density and compressibility of acoustic metamaterials.....	119
B.	Band structure of 2D acoustic metamaterial lattice.....	122
C.	Description of the inverse method for the properties of acoustic metamaterials.....	125

## LIST OF FIGURES

Figure 2.1 Geometry of a side-branch based acoustic metamaterial. ....	9
Figure 2.2 Schematics of single branch and multiple branch opening metamaterials. (a) Single branch. (b) Double branch. (c) Quadruple branch. Ten unit cells are included in each structure. (d) The side view and dimensions of three unit cells with single branch openings. ....	10
Figure 2.3 Lumped model of the proposed structures. (a) Single branch. (b) Double branch. (c) Quadruple branch .....	11
Figure 2.4 Transmission coefficients for a unit cell with single branch opening. Inset shows the geometry of the structure.....	15
Figure 2.5 Normalized bulk moduli of different branch structures. (a) Single branch opening. (b) Double branch opening. (c) Quadruple branch opening. The metamaterials have negative bulk moduli below cutoff frequencies where $E_{eff} / E_0 = 0$ . ....	17
Figure 2.6 Transmission coefficients for different structures with unit cell number $n = 1$ . (a) Single branch opening. (b) Double branch opening. (c) Quadruple branch opening. ....	19
Figure 2.7 Transmission coefficients for different structures with unit cells number $n = 10$ . The arrows indicate the cutoff frequencies predicted by Eq. (2.12). (a) Single branch opening. (b) Double branch opening. (c) Quadruple branch opening.....	20
Figure 3.1 A membrane or plate clamped in a waveguide. (a) Without mass attached. (b)With mass attached.....	24
Figure 3.2 Transmission loss of the plate sample. The first resonance frequency is at 4360 Hz. .	25
Figure 3.3 Effective density of the square plate with width $a = 20$ mm. ....	27
Figure 3.4 Snapshots of the AHMM. (a) Physical structure of the AHMM. To study the effective acoustic properties, the 2D AHMM can be decoupled into two waveguides in each direction: one contains periodically arranged plates (y-direction) and the other one does not (x-direction). (b) Photo of the fabricated sample. ....	29
Figure 3.5 Calculated EFC at two selected frequencies which are both below the cutoff frequency. Solid line: lumped model. Circle mark: retrieved from numerical simulations. ....	30
Figure 3.6 Band structure of the AHMM unit cell. The inset illustrates the unit cell and the plates. ....	31
Figure 3.7 The simulation setup for negative refraction. This behavior can be quantitatively evaluated by examining the shifted distance $\Delta x$ of the beam. ....	33

Figure 3.8 (a) Numerical demonstration of negative refraction using at 2450 Hz. (b) Theoretical and simulated shifted distances. ....	34
Figure 3.9 Experiment setup for partial focusing. ....	37
Figure 3.10 Simulated and measured acoustic fields showing partial focusing at 2440 Hz. ....	38
Figure 3.11 Normalized pressure magnitude distributions on the exiting surface of the AHMM. ....	39
Figure 3.12 Simulated and measured acoustic fields at 2.9 kHz. ....	40
Figure 3.13 Measured acoustic fields demonstrating subwavelength imaging. (a) Imaging performance of the AHMM at 1.1 kHz. (b) The broadband performance of subwavelength imaging of the AHMM. ....	41
Figure 3.14 Enhanced transmission of evanescent waves across the AHMM sample at 1.1 kHz. ....	43
Figure 3.15 EFC of an ADNZ medium with low, moderate and high losses. Dashed line represents the free space. ....	44
Figure 3.16 (a) Transmission coefficients of the ADNZ medium with various losses. (b) The $x$ -direction wave impedance of the ADNZ medium with various losses. ....	46
Figure 3.17 Effective density along the $y$ -direction with different losses. ....	48
Figure 3.18 The acoustic pressure and intensity fields. Top: acoustic pressure fields from real structure. Middle: acoustic pressure fields from effective medium. Bottom: acoustic intensity fields from real structure. (a) Low loss. (b) Moderate loss. (c) High loss. ....	50
Figure 3.19 Pressure amplitude distribution on the image plane for different loss factors. ....	51
Figure 4.1 (a) Schematic of the CMM, the aberrating layer, and the background medium. (b) Concept of the CMM for enhancing the sound transmission. ....	55
Figure 4.2 Schematic of the CMM and aberrating layers and the background medium. ....	59
Figure 4.3 Schematic of acoustic cloaking using CMMs. ....	61
Figure 4.4 (a) Schematic of a portion of the quasi-2D CMM. (b) Schematic of a 1D side branch and plate-type metamaterial. (c) Equivalent acoustic circuit of a single unit cell of the 1D structure in (b). ....	63
Figure 4.5 Effective densities and compressibility extracted from full-wave simulations and predicted by the lumped model. (a) Effective densities in $x$ - and $y$ -directions. (b) Effective compressibility. ....	66
Figure 4.6 Acoustic intensity field for a curved array (focused beam). Three cases are presented: (a) the skull only, (b) homogeneous medium, and (c) with CMM and the skull. Acoustic intensity field for a linear array (unfocused beam). Three cases are presented: (d) skull only, (e) homogeneous medium, and (f) with CMM and the skull. ....	68

Figure 4.7 (a) Focused beam, homogeneous medium. (b) Focused beam. (c) Unfocused beam, homogeneous medium. (d) Unfocused beam. ....	69
Figure 4.8 Acoustic intensity field of a curved array (focused beam). Three cases are presented: (a) Aberrating layers only. (b) Homogeneous medium. (c) With CMM and aberrating layers. ....	72
Figure 4.9 Acoustic pressure fields for a point source which is blocked by a slab. (a) Slab only. (b) Homogeneous medium. (c) With cloaking device adjacent to the slab. ....	73
Figure 5.1 Acoustic pressure field of an incoming wave transmitting through a GIM. ....	77
Figure 5.2 Schematic of the working principle of the device. (a) Low transmission case where the incident wave faces the GIM. (b) k-space diagram showing that the rotation of momentum vector causes its mismatch in transverse components, leading to the low transmission. (c) High transmission case where the incident wave faces the ZIM. ....	78
Figure 5.3 Geometry of the metasurfaces (a) ZIM. (b) GIM. ....	79
Figure 5.4 Retrieved refractive index of a ZIM unit cell. ....	81
Figure 5.5 Simulation and experimental setup. Inset shows the photo of the fabricated sample. .	82
Figure 5.6 Simulated and measured acoustic fields at 3.1 kHz for incident waves in different directions. Axis unit: cm. (a) Incident beam is facing the GIM, corresponds to low transmission case. (b) Incident beam is facing the ZIM, corresponds to high transmission case. ....	83
Figure 5.7 Normalized transmission for different directions of incoming waves. ....	85
Figure 5.8 Normalized intensity transmission as a function of the incident angle. ....	86
Figure 6.1 Transmitted phase for different types of unit cells. ....	93
Figure 6.2 Transmission coefficient of different types of unit cells. ....	94
Figure 6.3 (a) Ideal image to be projected. (b) Calculated image using GSW algorithm. (c) Ideal phase on the source plane. ....	95
Figure 6.4 Simulation setup in COMSOL. Unit: mm. ....	96
Figure 6.5 Generation of acoustic intensity fields at different focal depth from ASA. White arrow denotes the ideal distance from the image plane. ....	97
Figure 6.6 Generation of acoustic intensity fields at different focal depth from COMSOL. White arrow denotes the ideal distance from the image plane. ....	98
Figure 6.7 Photo of the assembled hologram. ....	99
Figure 6.8 Experiment setup of the hologram measurement. ....	100
Figure 6.9 (a) Ideal and (b) Measured phase behind the hologram. ....	101
Figure 6.10 Generation of the acoustic pressure fields at different focal depth from measurements. ....	102

Figure 6.11 (a) Ideal focal pattern. (b) Ideal phase behind the multifocus lens. (c) Measured phase behind the multifocus lens.....	103
Figure 6.12 Simulation and measurement results of the acoustic intensity fields of the multifocus lens. Focal depth: left: 10 cm, middle: 20 cm, right: 30 cm. ....	104
Figure A.1 Unit cell of a plate-type acoustic metamaterial for calculating effective density. ....	120
Figure A.2 Unit cell of a plate-type acoustic metamaterial for calculating effective bulk modulus. ....	121
Figure B.1 Geometry of the unit cell in COMSOL. Unit: m. ....	122
Figure B.2 Boundary conditions of the unit cell. ....	123
Figure B.3 Setting of the parametric sweep study in COMSOL. ....	123
Figure B.4 Band structure of a plate-type acoustic metamaterial unit cell.....	124
Figure C.1 Unit cell of a labyrinthine acoustic metamaterial. ....	126

## LIST OF TABLES

Table 2-1 Background medium properties and structure dimensions used in the simulation .....	15
Table 6-1 Design parameters of the acoustic hologram .....	91

## Chapter 1 Introduction

For centuries, researchers and scientists have been trying to study and control the wave propagation behaviors. In conventional approaches, people tried to find or develop material or composites with satisfactory properties to manipulate classical waves. For instance, optical lenses were developed for focusing in electromagnetic waves and porous materials were found to be useful in absorption for acoustic waves. However, the natural resources are limited and the desired properties may not be possible to be achieved using conventional materials. A question arises inevitably: can we design materials/structures that have constitutive parameters not found in nature? The answer was yes and the emergence of metamaterials brought the wave manipulation techniques to a new horizon that was not previously imagined.

### 1.1 Acoustic Metamaterials and Metasurfaces

It is not an entirely new idea to design composite materials/structures with tailored building blocks in order to yield an effective parameter. However, it was the emergence of metamaterials that eventually realized the material properties that were not attainable in nature. It was first promised theoretically that an effective medium with simultaneously negative permittivity and permeability does not contradict the Maxwell's equations for electromagnetic waves<sup>1</sup>. This type of material was first characterized as "left-handed" material since it disobeys the Doppler effect, Cherenkov radiation and Snell's law, and is possible in principle with a refractive index to be negative. Later on, Pendry *et al.* demonstrated that a 3D array of thin metal wires could exhibit negative permittivity in gigahertz (GHz) range<sup>2</sup>, and nonmagnetic thin sheets of metal is possible

to achieve a wide range of permeabilities, which may be negative close to the resonance frequency<sup>3</sup>. Subsequently, a composite medium of simultaneously negative permeability and permittivity was proposed experimentally, which was a breakthrough in the field of physics<sup>4</sup>.

Inspired by the work in electromagnetic waves, in 2000, Liu *et al.* proposed the first realization of acoustic metamaterials, which consist of a matrix of silicone rubber-coated lead spheres<sup>5</sup>. The first resonance frequency is around 400 Hz and the size of the structure is two orders of magnitude smaller than the corresponding wavelength, thus bringing the long existed concept of phononic crystals into the acoustic metamaterials realm. The strong dispersion in the dynamic mass density, either extremely large or negative, breaks the mass-density law of sound transmission. This revolutionized the way we treat and manipulate acoustic waves. With a time span of less than twenty years, the field of acoustic metamaterials has propelled and numerous exciting possibilities have been realized.

The two key material parameters dictating the acoustic wave behavior is the density and bulk modulus, as can be seen of the acoustic wave equation in a homogeneous medium without loss in an isentropic manner:

$$\nabla^2 p - \frac{\rho}{B} \frac{\partial^2 p}{\partial t^2} = 0 \quad (1.1)$$

where  $p$  is the acoustic pressure and  $B$  is the scalar bulk modulus of the medium. The acoustic wave velocity  $c$  is given by  $\sqrt{B/\rho}$ . By controlling these two parameters, the propagation of acoustic waves can be identified. For example, either negative density or negative modulus will make the wave vector imaginary, as implied by:

$$k^2 = \omega^2 \frac{\rho}{B} \quad (1.2)$$

An imaginary wave vector means that the acoustic waves propagating inside such a medium is evanescent and will decay exponentially. In this way, negative density/negative modulus acoustic metamaterials can be useful in sound insulation, especially at low frequencies, as they break the mass law. The acoustic metamaterials, which exhibit exotic constitutive parameters in the effective medium sense, can therefore control the acoustic waves in an unusual manner unprecedented. By taking the effective medium theory, the size of the unit cells of the acoustic metamaterials generally needs to be sufficiently smaller compared to the operating wavelength (typically about ten times smaller). In this way, the internal behavior of a single unit cell is dominant and the acoustic metamaterial can be regarded as a homogeneous medium. It should be pointed out that although the building blocks of acoustic metamaterials were first designed using resonant structures, resonance is not necessarily required to yield extreme material properties. In some situations, the non-resonant units may be even more favorable as they potentially have wider bandwidth compared to the resonance ones.

Acoustic metasurfaces, as a sub-category of acoustic metamaterials, is a newly developed concept developed in recent years<sup>6</sup>. Similar to acoustic metamaterials, this idea is also first introduced in electromagnetic waves<sup>7</sup>. The key feature of metasurfaces is that compared the bulk structures that are commonly associated with acoustic metamaterials, they usually have a thin thickness, which greatly reduce the geometric complication. With various design techniques, acoustic metasurfaces typically possess promising functionalities on the transmission/reflection behavior for incoming acoustic waves.

## 1.2 Research Motivation and Objective

To circumvent the limits of classical acoustics in controlling acoustic waves, the acoustic metamaterials imposes new strategies in dealing with wave propagation behaviors. For example, the resolution of an acoustic image is always below the diffraction limit. However, using acoustic metamaterials one can construct an acoustic lens that is able to overcome the diffraction limit which is not possible for conventional lens systems<sup>8,9</sup>. Another interesting example is acoustic cloaking, which means to hide an object so that it will not distort the acoustic field in which it is immersed, and one will not be able to detect its existence through acoustic waves. Using the powerful tool of coordinate transformation, this has been experimentally realized in both two-dimensional (2D) and three-dimensional (3D) scenarios<sup>10,11</sup>. Acoustic metasurfaces, on the other hand, showed versatile capacities on phase modulation and absorptions, and has aroused much research intention.

The field of acoustic metamaterials is rapidly growing, and although a lot of progress has been made in recent years, more potentials remains unclear and needs to be further explored. In this dissertation, the main objective is to give a comprehensive study on the design and applications of acoustic metamaterials and metasurfaces. Different types of acoustic metamaterials and metasurfaces, possessing various applications, will be investigated both theoretically and numerically. For some of the structures, they will be further validated by experiments. The contributions to this field are summarized as below:

- Presented theoretical investigations and numerical simulations of one-dimensional (1D) acoustic metamaterials that exhibit wide negative effective bulk modulus band down to zero<sup>12</sup>. A lumped model was developed to characterize the proposed

structure, and as much as 100% increase over the traditional single branch opening structure in bandwidth was achieved. The results were confirmed by numerical simulations.

- Proposed a design of a broadband acoustic hyperbolic metamaterial (HMM) using paper plates with true hyperbolic dispersion below a certain cutoff frequency<sup>13</sup>. Carried out numerical simulations and experiments to demonstrate partial focusing and subwavelength imaging at frequencies between 1.0 and 2.5 kHz. Enhanced transmission of evanescent waves and negative refraction were verified theoretically and numerically. The effect of material loss in anisotropic density near-zero metamaterial was also analyzed<sup>14</sup>.
- Investigated a type of anisotropic, complementary acoustic metamaterial (CMM) and its application in restoring acoustic fields distorted by aberrating layers<sup>15</sup>. Used numerical simulations to evaluate the technique, which led to dramatically reduced acoustic field distortion and enhanced sound transmission. The acoustic intensity at the focus is increased from 28% to 88% of the intensity in the control case (in the absence of the aberrating layer and the CMM) in the example where a focused beam was studied, therefore virtually removing the layer in a noninvasive manner.
- Designed and experimentally characterized acoustic metasurfaces yielding asymmetric transmission within a certain frequency band<sup>16</sup>. By combining a gradient-index metasurface and a near-zero-index metasurface, the transmission contrast between the two incident directions was found to be high at certain

frequencies. Moreover, the structure was compact and had a flat geometry, enabling easy integration with other structures.

- Used an iteration based algorithm to design an acoustic hologram for image projection and multifocusing<sup>17</sup>. Fabricated, assembled the hologram with 12 types of individual unit cells and verified the results both numerically and experimentally. It was shown that by carefully modulating the transmitted phase across each unit cell, different image patterns can be obtained. The proposed hologram exhibited great potential of manipulating acoustic waves.

## Chapter 2 Acoustic Metamaterial with Negative Modulus

The negative effective constitutive parameters of metamaterials serve as key requirements in many novel applications, such as superlensing and negative refraction<sup>18,19</sup>. In acoustic regime, as we have seen in the previous chapter, the two key parameters to control acoustic waves is density and bulk modulus. The primary goal in this chapter is to extend the bandwidth of negative modulus of traditional side-branch based acoustic metamaterial. We developed a lumped model to characterize the structure with multiple branch openings and confirmed the results using numerical simulations.

The first approach to achieve negative modulus is to use shunted Helmholtz resonators at ultrasonic frequencies<sup>20</sup>. The collective resonance of the Helmholtz resonators behaves as a negative volume connected to the main tube, and the effective modulus is shown to be negative near the resonance frequency. Due to the oscillating nature of the resonators, the bandwidth of negative modulus is usually narrow and cannot reach zero frequency. In addition, this type of negative modulus is usually accompanied with strong energy dissipation. Acoustic metamaterial with broadband negative modulus and low loss is therefore highly desired in the field of acoustics.

### 2.1 Side-branch Based Acoustic Metamaterial

In 2009, Lee *et al.* proposed a similar design with the previous ones using Helmholtz resonators, which consist of periodic branch openings on a main tube<sup>21</sup>. It was demonstrated that such open-ended side tubes were capable of producing negative modulus from zero frequency to a certain cutoff frequency. In their design, the negative bulk modulus was not introduced by resonance and consequently had low energy loss.

Such design is thus favorable in acoustic realm due to its wide bandwidth and simple structure. For example, it can be easily integrated with a membrane-type acoustic metamaterial to generate double-negative metamaterials<sup>22</sup>.

The typical geometry of such a structure is depicted in Fig. 2.1, with a square cross section of the main tube. By neglecting the damping term, the effective bulk modulus and phase velocity of the structure is expressed as<sup>21</sup>:

$$E_{eff} = \frac{E_0}{1 - \frac{\omega_0^2}{\omega^2}} \quad (2.1)$$

$$v_{ph} = \frac{v_0}{\sqrt{1 - \frac{\omega_0^2}{\omega^2}}} \quad (2.2)$$

where  $E_0$  and  $v_0$  are the modulus and speed of sound of the background medium (chosen as air in this study),  $\omega_0$  is the cutoff frequency,  $\omega$  is the angular frequency, respectively. Note that these equations do not consider the effect of the waveguide. It can be seen that both the effective modulus and phase velocity are negative below the cutoff frequency, thus forming a forbidden band below this frequency. The cutoff frequency,  $\omega_0$ , is dependent on the geometry of the side branch for a fixed dimension of the main tube. In practice, the dimension of the side tube is limited by that of the main tube, and imposes difficulty in increasing the cutoff frequency. For example, the diameter of the side tube cannot exceed the width of the main tube, and the height of the side tube should not take an arbitrarily large value if fabrication is a consideration.

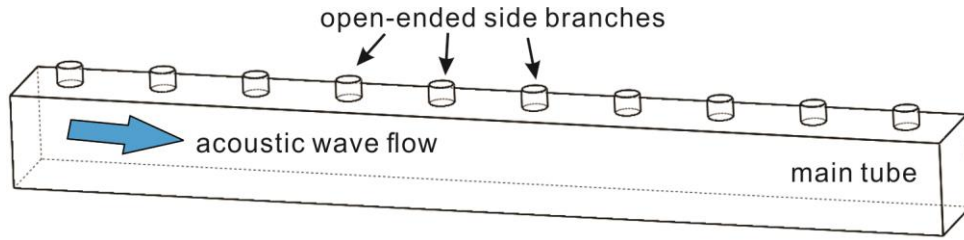


Figure 2.1 Geometry of a side-branch based acoustic metamaterial.

## 2.2 Multiple Branch Openings for Broader Bandwidth

In order to circumvent the difficulties mentioned above, here we utilize multiple branch openings as an alternative means to increase the cutoff frequency. As we shall discuss in the following sections, the 1D acoustic metamaterials with double and quadruple branch openings have negative bulk modulus bands considerably wider than the ones with single branch openings. It also provides another approach to tune the cutoff frequency and the effective modulus of branch-based acoustic metamaterials.

### 2.2.1 Lumped Model

The schematics of single branch, double branch and quadruple branch opening metamaterials are shown in Fig. 2.2. For simplification, the main tube is assumed to be rectangular, so that it can be easily integrated with side branches. The dimensions of the main tube and the side branches are labeled in Fig. 2.2(d). The proposed metamaterials consist of unit cells with circular branch openings on the facades of each unit cell. All branches are assumed to have the same dimensions (i.e., height and radius). However, it should be pointed out that the analytical model outlined in this chapter can be applied to more general cases where acoustic waveguides and side branches are used.

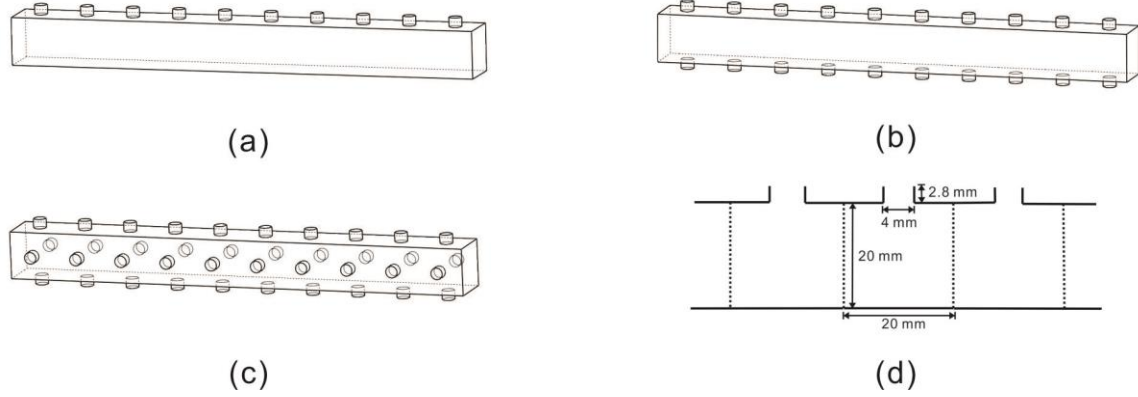


Figure 2.2 Schematics of single branch and multiple branch opening metamaterials. (a) Single branch. (b) Double branch. (c) Quadruple branch. Ten unit cells are included in each structure. (d) The side view and dimensions of three unit cells with single branch openings.

We here analyze the structures using a lumped model, the lumped model is assumed to have reasonably accurate results under low frequency approximation. In the equivalent acoustic transmission line circuit, a 1D waveguide can be described by an acoustic compliance/capacitor in shunt and a mass/inductor in series<sup>23</sup>. The inductor, however, only contributes to the effective density of the structure and therefore is omitted here for simplification. In fact, the waveguide is assumed to have negligible effect on the effective density of the structure<sup>21</sup>. The branch openings, on the other hand, can be described by acoustic inductors in shunt<sup>24</sup> as shown in Fig. 2.3. The acoustic capacitance of the waveguide and the acoustic inductance of a single opening read:

$$C_a = \frac{A}{E_0} d \quad (2.3)$$

$$m_a = \frac{Z_a}{i\omega} \quad (2.4)$$

where  $A$  is the cross-sectional area of the waveguide (square in this chapter),  $d$  is the length of the unit cell,  $Z_a$  is the acoustic impedance of the branch at the inner opening connecting to the waveguide, respectively.  $E_0 = \rho_0 c_0^2$  with  $\rho_0$  be the background medium density. To this end, we will first estimate the total effective capacitance  $C_{eff}$  caused by both  $C_a$  and  $m_a$ ; the effective bulk modulus  $E_{eff}$  of the branch-based structures will then be derived in a fashion that consider the structure as a homogenized medium:

$$C_{eff} = \frac{A}{E_{eff}} d \quad (2.5)$$

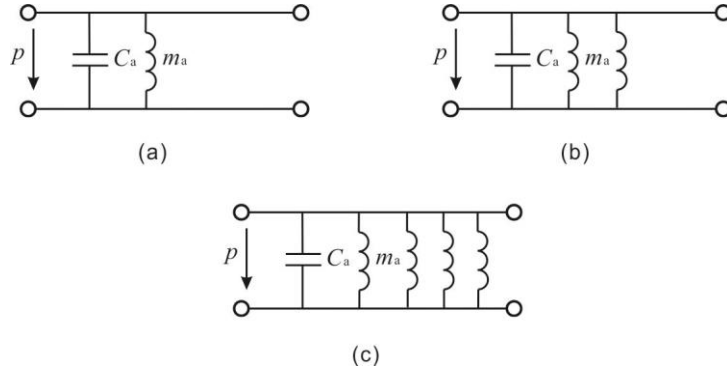


Figure 2.3 Lumped model of the proposed structures. (a) Single branch. (b) Double branch. (c) Quadruple branch

For a single branch, the acoustic impedances at the two ends of the branch can be related by the following equation<sup>24</sup>:

$$Z_a = \frac{Z_0 Z_{ah} S + i Z_0 \tan(kl_e)}{S i Z_{ah} S \tan(kl_e) + Z_0} \quad (2.6)$$

where  $Z_0 = \rho_0 c_0$  is the acoustic impedance of the background medium,  $Z_{ah}$  is the acoustic impedance at the outer opening of the branch,  $S$  is the cross-sectional area of the branch opening,  $k = \omega / c_0$  is the wave number, and  $l_e$  is the effective length of the branch. The effective length of the branch is the sum of the height of the branch ( $h$ ) and two end corrections, namely the end correction for inner and outer openings. The end corrections take the effect of the radius of the branch into account. Since the outer opening is unflanged, the end correction  $\Delta l_1$  is theoretically  $0.6a$ , where  $a$  is the radius of the openings<sup>24</sup>. There is no existing analytical end correction for the inner opening as it is connected to a confined space; the boundary condition is neither ideally flanged (of which the end correction is  $0.85a$ ) nor unflanged because of the existence of the side branches. It should be noted that accurate end corrections are critical in determining the cutoff frequency of the structure under study. We here use numerical simulations to determine the end correction for the inner opening, the details are given in section 2.2.2, and it is found that  $\Delta l_2 = 0.69a$ . Furthermore, to model branches with open ends, pressure release boundary condition ( $Z_{ah} = 0$ ) is used such that the end correction for the outer opening will not be contained and the branch height in the simulation is modified to be  $h + \Delta l_1$ . This is equivalent to modeling an open-ended branch with a height of  $h$  connecting to free space<sup>25</sup>. The acoustic impedance of the branch can then be simplified as:

$$Z_a = i \frac{\rho_0 c_0}{S} \tan(kl_e) \quad (2.7)$$

From a homogenized perspective, the effective total capacitance can be estimated from

$$\frac{1}{i\omega C_{eff}} = \frac{1}{i\omega C_a + Z_a^{-1}} \quad (2.8)$$

As the unit size is significantly smaller than the wavelength at the frequencies of interest, the structure can be regarded as a homogenized medium with an effective modulus  $E_{eff}$ .

Substituting Eqs. (2.3), (2.4) and (2.7) into Eqs. (2.5) and (2.8), we have

$$E_{eff} = \frac{\omega E_0}{\omega - \frac{SE_0}{\rho_0 c_0 Ad \tan(kl_e)}} \quad (2.9)$$

At low frequencies,  $\tan(kl_e)$  can be simplified to  $kl_e$ , and Eq. (2.9) reduces to

$$E_{eff} = \frac{\omega E_0}{\omega - \frac{SE_0}{\rho_0 c_0 Ad kl_e}} \quad (2.10)$$

The cutoff frequency  $\omega_0$  for the single branch structure can be determined by setting the denominator in Eq. (2.10) to zero, which yields

$$\omega_0 = \left( \frac{Sc_0^2}{Adl_e} \right)^{1/2} \quad (2.11)$$

Equations (2.10) and (2.11) imply that, the bandwidth of negative modulus is determined by the cutoff frequency of the branch opening, i.e., the bulk modulus is negative below the cutoff frequency.

The process for analyzing acoustic metamaterials with double and quadruple branch openings is similar to single branch opening. Since the acoustic inductors are in shunt as illustrated in Fig. 2.2(b) and (c), the acoustic impedance of the branches are  $Z_a^s = 2Z_a^d = 4Z_a^q$ , where subscripts  $s$ ,  $d$  and  $q$  represent single branch, double branch and quadruple branch openings, respectively. Equivalently, the effective lengths for different

structures at low frequencies are  $l_e^s = 2l_e^d = 4l_e^q$ , due to the approximation to Eq. (2.7), i.e.,

$Z_a = i \frac{\rho_0 c_0}{S} k l_e$ . Substituting the resulting effective lengths into Eq. (2.11), the cutoff

frequencies for different branch structures are

$$\omega_0^q = \sqrt{2} \omega_0^d = 2 \omega_0^s \quad (2.12)$$

Furthermore, for single branch opening metamaterials, assuming  $h$  is infinitely small and the outer opening can be considered flanged. The minimum value for  $l_e$  is thus  $0.69a + 0.85a$ , This will set an upper limit for the cutoff frequency  $\omega_0$  as:

$$\omega_{0\max} = \left( \frac{S c_0^2}{1.54 A d a} \right)^{1/2} \quad (2.13)$$

The minimum value for  $l_e$  can be now overcome using more branch openings, raising the upper limit for  $\omega_0$ . Equations (2.12) and (2.13) show that, within a frequency range of  $\omega_0^s \sim 2\omega_0^s$ , negative modulus can only be achieved by double branch or quadruple branch openings, provided that  $\frac{S}{Ad}$  remains constant. It could be argued that increasing  $\frac{S}{Ad}$  also raises the cutoff frequency. However, from a geometrical perspective,  $S$  is limited by the width of the waveguide (diameter cannot exceed the width), and  $d$  is also limited by the diameter of the opening ( $d$  cannot be less than the diameter). These pose bottlenecks for tuning the cutoff frequency. By introducing multiple branch openings, the cutoff frequency can be increased.

### 2.2.2 Numerical Simulations

Simulations based on finite element solver COMSOL Multiphysics 4.3b are now carried out to validate the theoretical findings. The pressure acoustics module is adopted and all the simulations are in frequency domain. The end correction  $\Delta l_2$  is first determined. A model is established which involves one unit cell from the single branch opening structure as shown in the inset of Fig. 2.4. The background medium properties and structure dimensions are listed in Table 2.1.

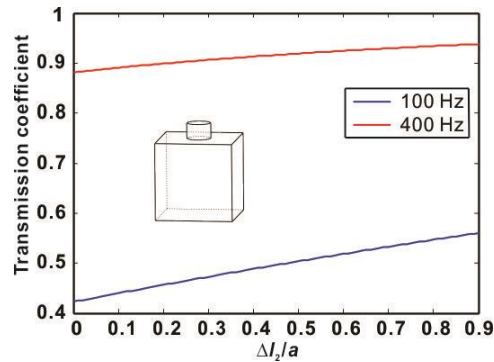


Figure 2.4 Transmission coefficients for a unit cell with single branch opening. Inset shows the geometry of the structure.

Table 2-1 Background medium properties and structure dimensions used in the simulation

$\rho_0$ (kg/m <sup>3</sup> )	$c_0$ (m/s)	$r$ (mm)	$h$ (mm)	$d$ (mm)	$A$ (mm <sup>2</sup> )
1.2	343	2	2.8	20	400

The transmission coefficient through this structure can be then extracted at different frequencies. Two arbitrary frequencies within the bandwidth of interest were chosen: 100

and 400 Hz. Their transmission coefficients were 0.53 and 0.93, respectively. On the other hand, the analytical solution for the transmission coefficient of this structure can be expressed as<sup>24</sup>:

$$T = 1 - \frac{Z_0 / 2A}{Z_0 / 2A + Z_a} \quad (2.14)$$

where  $Z_a$  is given by Eq. (2.7) and depends on  $\Delta l_2$ . Figure 2.4 shows the transmission coefficients with varied  $\Delta l_2$  according to Eq. (2.14). The theoretical values matched up well with the COMSOL simulation results when  $\Delta l_2 = 0.69a$ . This was used as the end correction for the inner opening of the branch throughout this chapter. It must be stressed that, the end correction could depend on the geometry of the structure (e.g., cross-sectional areas of the waveguide and the branch, and the separation between adjacent branches) and therefore should be determined accordingly for the specific structure under study.

Subsequently, the lumped model was compared with numerical simulations. The acoustic fields inside the proposed 1D acoustic metamaterials depicted in Fig. 2.2 was computed by COMSOL. A finite difference method was utilized to extract the effective modulus from the acquired acoustic fields<sup>26</sup>. The details of the method are presented in Appendix A. The normalized effective moduli  $E_{eff} / E_0$  of the 1D acoustic metamaterials composed of single, double and quadruple branch openings are depicted in Fig. 2.5. Excellent agreement can be observed between the theoretical and numerical approaches. The numerical results show that a single branch opening metamaterial has negative modulus below 930 Hz. The bandwidths of negative modulus (or cutoff frequencies) obtained from simulations were 1340 and 1860 Hz for double branch and quadruple branch

opening metamaterials, respectively. They are therefore 44% and 100% higher than the traditional single branch opening design, which are in good agreement with simulation results according to Eq. (2.12), from which the two values in theory should be 41% and 100%. Our simulation and lumped model indicate that metamaterials with double or quadruple branch openings could effectively broaden the negative modulus band, owing to the reduced effective length of the branches. The effective modulus of side branch based acoustic metamaterials can also be predicted by the lumped model in the low frequency range. It is noted that at the highest cutoff frequency of quadruple branch opening case, i.e., 1860 Hz, the unit cell size (20 mm) is about 1/10 of the wavelength, justifying the usage of medium homogenization theory.

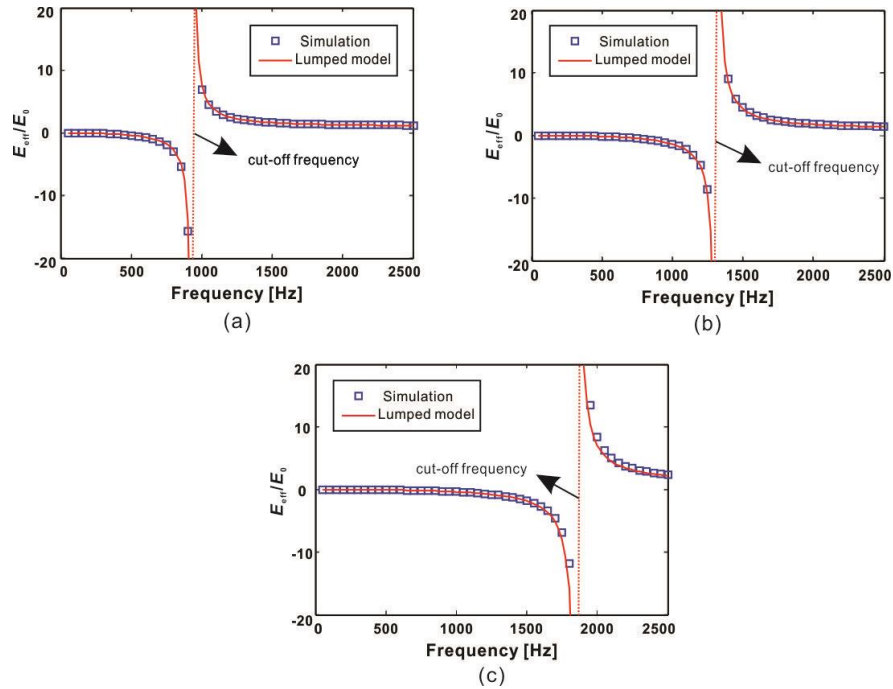


Figure 2.5 Normalized bulk moduli of different branch structures. (a) Single branch opening. (b) Double branch opening. (c) Quadruple branch opening. The metamaterials

have negative bulk moduli below cutoff frequencies where  $E_{eff} / E_0 = 0$ .

Finally, we investigate the transmission coefficients of the proposed metamaterials as homogenized media. The characteristic impedance of the metamaterial can be written as  $Z_m = \rho_0 c_{eff}$ , where  $c_{eff} = \sqrt{E_{eff} / \rho_0}$  is the effective speed of sound, since the effective density is assumed to be unaltered. Consider a metamaterial layer of  $n$  unit cells with identical medium (air) on both sides, the reflection and transmission coefficients with normal incidence are<sup>27</sup>:

$$R = \frac{Z_m^2 - Z_0^2}{Z_0^2 + Z_m^2 + 2iZ_0Z_m \cot(\phi)} \quad (2.15)$$

$$T = \frac{1 + R}{\cos(\phi) - \frac{iZ_m \sin(\phi)}{Z_0}} \quad (2.16)$$

where  $\phi = \frac{2\pi fnd}{c_{eff}}$  is the phase change across the layer, and  $Z_0$  is the impedance of air.

Figures 2.6 and 2.7 show the transmission coefficient against frequency predicted by Eq. (2.16), where  $Z_m$  was obtained by the lumped model. Numerical simulations using COMSOL were carried out for comparison. To show the influence of the number of unit cells and validity of the homogenization approach for metamaterials at arbitrary lengths, two sets of results are shown, where  $n$  is equal to 1 and 10. Small ripples are observed in Fig. 2.7 above the cutoff frequencies, which are probably caused by the coupling between unit cells. The transmission coefficient curve is also steeper as the number of unit cells increases. Ideally, an infinite number of unit cells will give a dramatic change of transmission coefficient at the cutoff frequency (i.e., from zero to unity). The value of cutoff frequency, on the other hand, is not influenced by the number of unit cells, as it is

intrinsically determined by the dimensions of the structures. The lumped model is able to accurately predict the transmission coefficient of the metamaterials under study. At  $n = 10$ , significant change of transmission coefficients can be seen: the stop-band of the acoustic metamaterial is significantly broadened with more branch openings.

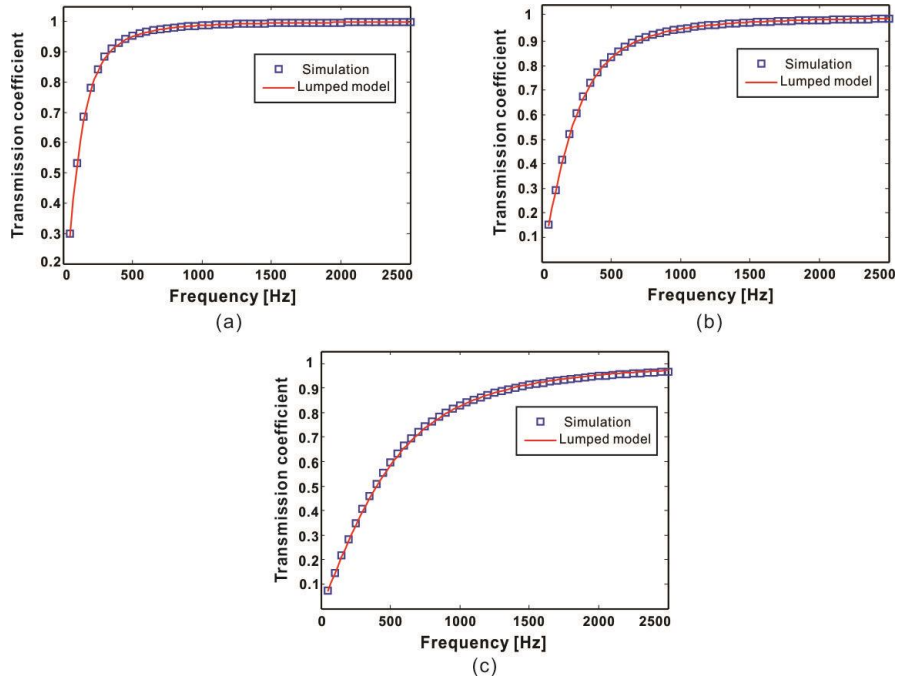


Figure 2.6 Transmission coefficients for different structures with unit cell number  $n = 1$ .

(a) Single branch opening. (b) Double branch opening. (c) Quadruple branch opening.

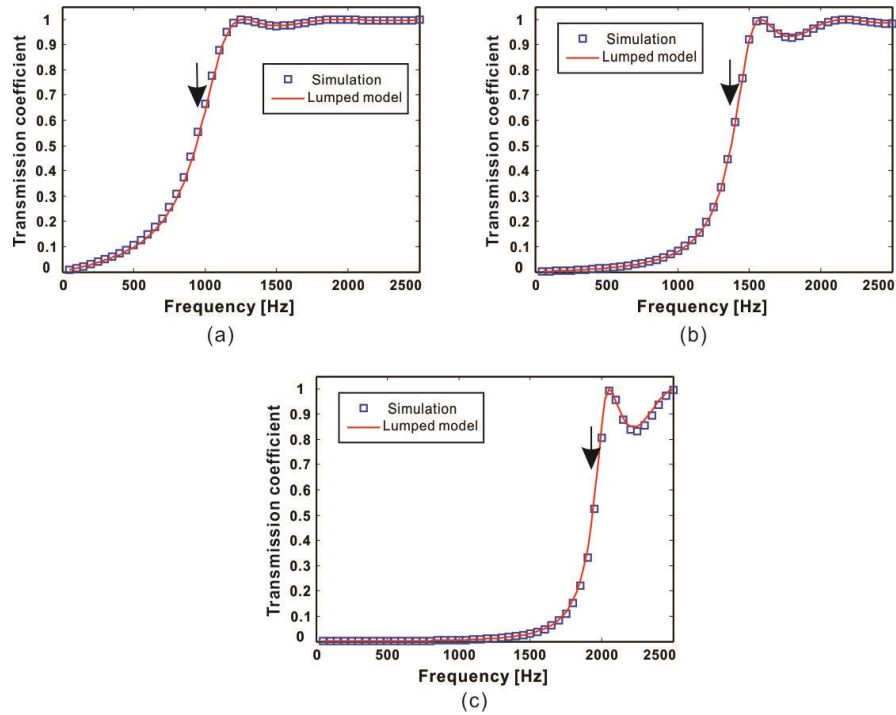


Figure 2.7 Transmission coefficients for different structures with unit cells number  $n = 10$ . The arrows indicate the cutoff frequencies predicted by Eq. (2.12). (a) Single branch opening. (b) Double branch opening. (c) Quadruple branch opening

From Figs. 2.6 and 2.7, it can be concluded that the transmission coefficient is smaller at lower frequencies, which contradicts with the famous mass law. This is because when the effective modulus is negative, the acoustic waves inside the structure are evanescent and decays quickly, as mentioned in chapter 1. This implies that the proposed structure may find usage in low frequency sound insulation, the geometry can also be tuned accordingly to have optimal performance at selected frequencies.

### 2.3 Summary

In this chapter, theoretical analysis and full wave simulations of multiple branch openings metamaterials are provided. A lumped model is established to describe this type of acoustic metamaterials. The end correction for branch opening is derived using a combination of analytical and numerical methods. Compared to traditional single branch opening structure, multiple branch openings can significantly broaden the bandwidth of negative modulus. The structure proposed here can be easily integrated with membrane-type metamaterials to achieve double negativity<sup>22</sup>. It is hoped that the broad bandwidth of the proposed structure can facilitate the design of acoustic metamaterials requiring single or double negative parameters.

### Chapter 3 Acoustic Metamaterial with Negative Density

As we have discussed in the previous chapters, density and bulk modulus are the two key parameters that one wish to control in order to manipulate acoustic waves. In this chapter, we continue to explore the negative parameters associated with acoustic metamaterials and focus our attention on the effective density. The acoustic metamaterials with negative effective density was initially created for the applications of sound insulation, the meta-atoms, which are the building blocks of the metamaterials, were constructed with metallic spheres coated by silicon rubbers<sup>5</sup>. Negative density was introduced with a Mie-type resonance of frequency much lower than the previous Bragg scattering frequency in phononic crystals. Because of the high dissipation and fabrication difficulties, practical implementations of this type of metamaterial are limited. From Newton's second law, which tells that the mass is proportional to the force and acceleration, one can expect that if the meta-atom accelerates out-of-phase with respect to the driving force, the effective density shall be negative. A more general and easier approach to achieve negative density was proposed in 2008 based on this assumption<sup>28</sup>. The structure was constructed with a small mass attached to the center of the membrane, which was fixed at the boundaries. The restoring force on the membrane served as a means to generate the out-of-phase oscillation of the membranes and the attached mass was used to tune the resonance frequency of the structure. The metamaterial was experimentally verified to break the mass density law of sound attenuation at the negative density region. Later on, it was found that the membrane itself is possible for the out-of-phase acceleration and the resonance frequency of the membrane can be tuned by its elastic properties other than the attached mass<sup>29</sup>. Plate-type metamaterials are similar to the membrane-type

metamaterials, the main difference is that no tension is applied on the plates. Other types of acoustic metamaterials with negative density include labyrinthine structures by coiling up space<sup>30</sup>. The exotic constitutive parameters are introduced by band foldings towards long wavelength regime without local resonance. In all, negative effective density has enabled numerous unique applications, like low frequency sound attenuation, acoustic superlensing, to name a few.

### 3.1 Membrane- and Plate-type Acoustic Metamaterials

The structure of a typical membrane- or plate-type acoustic metamaterial is illustrated in Fig. 3.1, with or without mass attached<sup>31</sup>. The membrane or plate is perfectly clamped inside the waveguide, and acoustic waves impinge normally on the membrane or plate. In this chapter, we are mainly focused on the membrane- and plate-type acoustic metamaterials without mass attached. Neglecting material loss, the effective density of membrane-type metamaterials can take the form<sup>29</sup>

$$\rho_{eff} = \rho' \left( 1 - \frac{\omega_c^2}{\omega^2} \right) \quad (3.1)$$

where  $\rho'$  is the average density of air loaded with the membrane or plate,  $\omega_c$  is the first resonance frequency of the membrane or plate. Note that this equation does not consider the effect of the waveguide. It can be seen from Eq. (3.1) that for no mass attached case, the effective density is negative below the first resonance frequency (cutoff frequency), and is close to zero near the first resonance frequency.

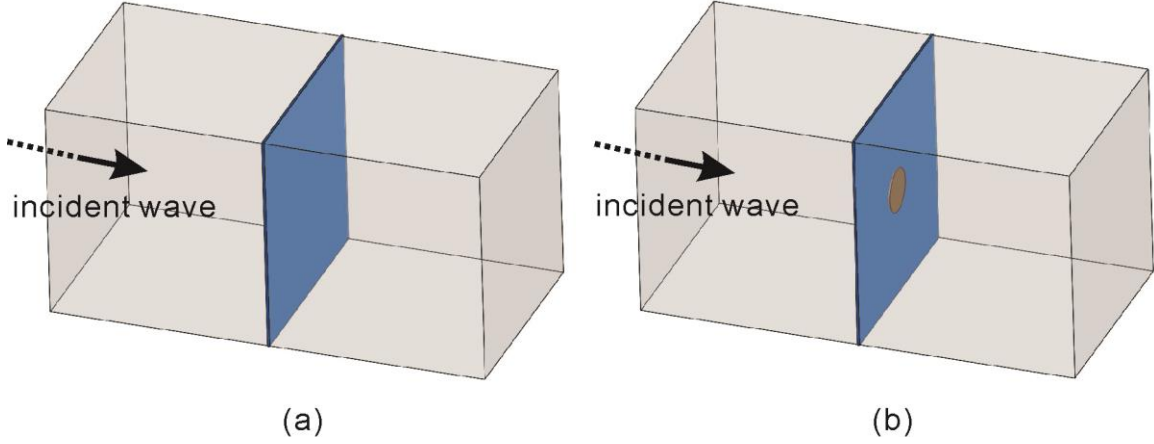


Figure 3.1 A membrane or plate clamped in a waveguide. (a) Without mass attached.  
 (b) With mass attached.

When there is no tension applied to the membranes, they fall into plate-type acoustic metamaterials, and here we use a semi-analytical model to characterize the metamaterials<sup>32</sup>. Note that the general scheme applies to membrane-type acoustic metamaterials as well. In order to incorporate the results with experiments that shall be mentioned later, here a specific type of paper plates is used. The plate has a density  $591 \text{ kg/m}^3$  and a thickness  $0.3 \text{ mm}$ . The first resonance frequency of a clamped square plate is given by<sup>33</sup>:

$$f_0 = \frac{5.58}{A} \sqrt{\frac{D'}{\rho h}} \quad (3.2)$$

where  $A$  is the cross-sectional area of the waveguide,  $D'$  is the flexural rigidity of the plate,  $\rho$  and  $h$  are the density and thickness of the plate, respectively. To determine the flexural rigidity of the paper plate, a single square plate with width  $a = 15.7 \text{ mm}$  is fabricated with boundaries clamped to an aluminum frame. The transmission loss (TL) of the sample is measured using a B&K impedance tube and is shown in Fig. 3.2. The first

TL dip observed at 4360 Hz indicates the first resonance of the plate, as the transmission coefficient reaches the maximum at the first resonance frequency. From Eq. (3.2), the flexural rigidity can be estimated by:

$$D' = 0.032 f_0^2 A^2 \rho h \quad (3.3)$$

The resulting flexural rigidity  $D'$  is then  $0.0066 \text{ Pa}\cdot\text{m}^4$ .

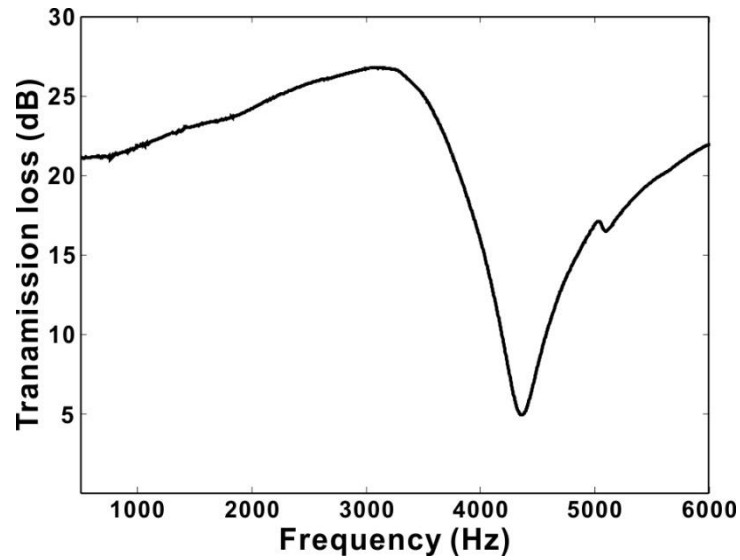


Figure 3.2 Transmission loss of the plate sample. The first resonance frequency is at 4360 Hz.

Since the values for Young's modulus and Poisson's ratio are needed in finite element package COMSOL for numerical simulations, these values are also estimated. The Poisson's of the paper plate is assumed to be 0.33<sup>34</sup>; from the definition of flexural rigidity, i.e.,  $D' = Eh^3/12(1-\nu^2)$ , the Young's modulus can be calculated as:

$$E = \frac{12D'(1-\nu^2)}{h^3} \quad (3.4)$$

where  $\nu$  is Poisson's ratio of the plate. The calculated Young's modulus of the plate is thus 2.61 GPa. It should be pointed out that, however, the numerical results of the plate-type metamaterial are not sensitive to errors in Young's modulus and Poisson's ratio. The most important plate property determining the performance of the metamaterial is the flexural rigidity, as it dictates the acoustic impedance of the thin plate and therefore the effective density<sup>23</sup>. It can be seen that Eq. (3.3), which is used to calculate the flexural rigidity of the plate, does not contain the Young's modulus and Poisson's ratio, but rather the first resonance frequency. Consequently, the resonance frequency  $f_0$ , which we carefully obtained from the impedance tube measurement, is more important than the estimated Young's modulus as well as the cited Poisson's ratio, and the calculated flexural rigidity is assumed to accurately predict the metamaterial behaviors.

Next, a lumped model can be utilized to predict the frequency-dependent effective density, which is written as

$$\rho_e = \frac{Z_{am}}{j\omega} \cdot \frac{A}{D} \quad (3.5)$$

where  $Z_{am}$  is the acoustic impedance of the plate,  $A = a^2$  is the cross-sectional area of the waveguide. Since there is no closed form solution of  $Z_{am}$  for a square plate, the acoustic impedance is calculated by the finite element method and is

$$Z_{am} = \frac{Z_m}{A^2} = \frac{\iint \Delta p A}{j\omega \xi A^2} \quad (3.6)$$

where  $Z_m$  is the mechanical impedance of the plate,  $\Delta p$  is the pressure difference across the plate, and  $\xi$  denotes the average transverse displacement of the plate. In finite element method,  $\Delta p$  is calculated by picking two planes near the front and back surface

of the plate, and  $\xi$  is obtained by averaging the transverse displacement over the entire plate. For a square plate with width  $a = 20$  mm, the first resonance frequency (or cutoff frequency) is calculated to be around 2.69 kHz according to the retrieved flexural rigidity. The predicted effective density from Eq. (3.5) is shown in Fig. 3.3, it is close to zero around the cutoff frequency and negative below the cutoff frequency.

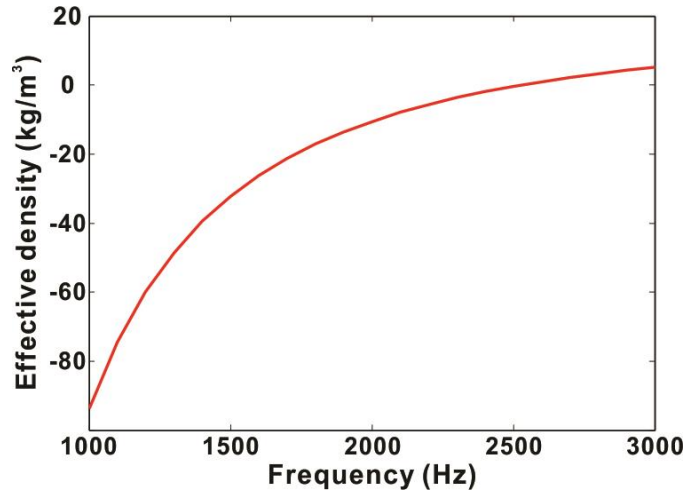


Figure 3.3 Effective density of the square plate with width  $a = 20$  mm.

### 3.2 Hyperbolic Acoustic Metamaterial

As we have discussed in the previous sections, acoustic metamaterials with negative density is useful in sound insulation, subwavelength imaging, etc. A specific type of acoustic metamaterial arises when the effective density along one direction becomes negative while it is positive along the others: the acoustic hyperbolic metamaterials (AHMMs). They are important in the acoustic family because of their extreme anisotropy and numerous possible applications, including negative refraction, backward waves, spatial filtering, and subwavelength imaging<sup>35-37</sup>. In 2D scenarios, the density is positive

in one direction and negative in the orthogonal direction. For materials with anisotropic densities, the general dispersion relation is given by

$$\frac{k_x^2}{\rho_x} + \frac{k_y^2}{\rho_y} = \frac{\omega^2}{B} \quad (3.7)$$

where  $B$  is the bulk modulus of the entire medium. For media with positive, anisotropic densities, the equifrequency contour (EFC) is an ellipse, whereas it is a hyperbola for AHMMs. Although the importance of AHMMs as a tool for achieving full control of acoustic waves is substantial, the realization of a broadband and truly hyperbolic acoustic metamaterial remains unclear. A broadband hyperlens has been demonstrated using brass fins<sup>8</sup>, the capability of subwavelength imaging, however, stems from extreme contrast of density and this hyperlens in fact does not bear a hyperbolic dispersion. It has been demonstrated theoretically and experimentally that periodically perforated plates can exhibit hyperbolic-like dispersion for airborne sound<sup>38,39</sup>. Negative refraction and energy funneling associated with this structure were demonstrated experimentally within a narrow band around 40 kHz. This design yields a flat band profile in EFC and therefore could not be used for acoustic partial focusing, which is an important application of AHMMs.

### 3.2.1 Hyperbolic Dispersion Relation

In this chapter, we show realization of a broadband AHMM utilizing plate-type acoustic metamaterials. The plates have the same material properties that have been discussed in section 3.1. The proposed structure exhibits truly hyperbolic dispersion, as demonstrated by its ability of partial focusing and subwavelength imaging over a broadband frequency. The designed structure of the AHMM is illustrated in Fig. 3.4. The rigid frames are made

of aluminum. There are 13 frames and each contains 14 plate unit cells. Each two frames have a separation distance of  $d = 2$  cm and the thickness of the frame is  $t = 0.16$  cm. The frames in the  $y$ -direction therefore have a periodicity of  $D = d + t = 2.16$  cm. The width of the square plate is  $a = 2$  cm. The boundaries of the plates are fixed securely on the frames. Two acrylic panels cover the top and bottom of the sample to ensure two-dimensional wave propagation. The aluminum frames are also secured inside the slits on the acrylic panels so that their vibration and interaction with acoustic waves are negligible. The overall size of the sample is 30.2 cm by 27 cm.

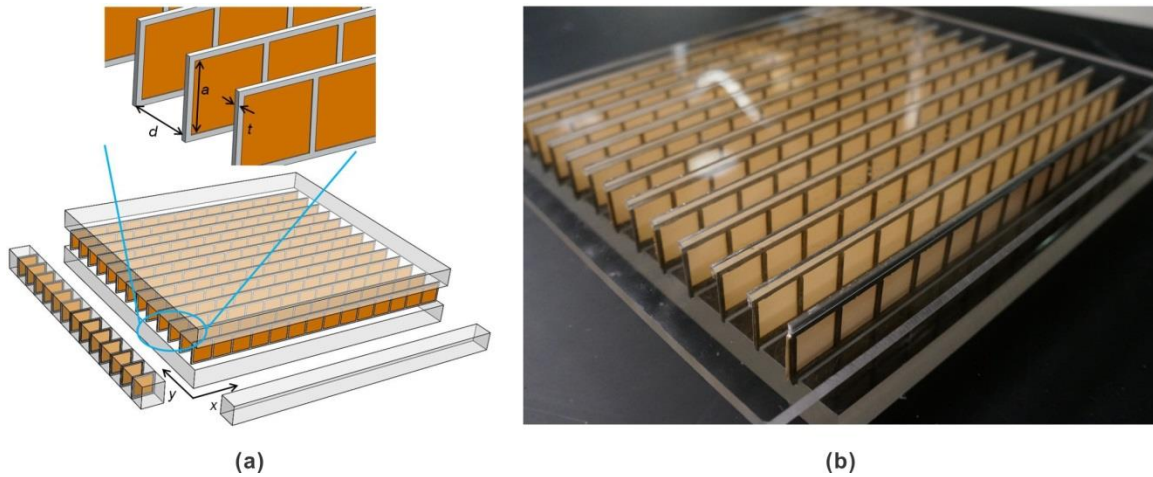


Figure 3.4 Snapshots of the AHMM. (a) Physical structure of the AHMM. To study the effective acoustic properties, the 2D AHMM can be decoupled into two waveguides in each direction: one contains periodically arranged plates ( $y$ -direction) and the other one does not ( $x$ -direction). (b) Photo of the fabricated sample.

To theoretically characterize the proposed AHMM, we use 1D analysis since wave propagation in  $x$ - and  $y$ -directions can be decoupled in this type of structures<sup>15,40</sup>. Because there are no plates arranged in the  $x$ -direction, the effective density can be

considered as that of air and is frequency-independent ( $\rho_x = 1.2 \text{ kg/m}^3$ ). In the  $y$ -direction, the method for obtaining its effective density is outlined in section 3.1 and is plotted in Fig. 3.3.

The corresponding EFC of the structure at relevant frequencies is depicted in Fig. 3.5 according to Eq. (3.7). Since  $\rho_x$  is always positive, the dispersion curve theoretically is a hyperbola over a broadband frequency. Two sets of results for the EFC are shown and are in good agreement. One is calculated using the effective density from the lumped model and the other one is from numerical simulations of the real structure without assuming homogenization. For the numerical results, the band structure of a unit cell is first studied, and the EFC is retrieved from the band structure, as will be shown in the following text. The dispersion curves are clearly hyperbolic and the EFCs become flat at low frequencies.

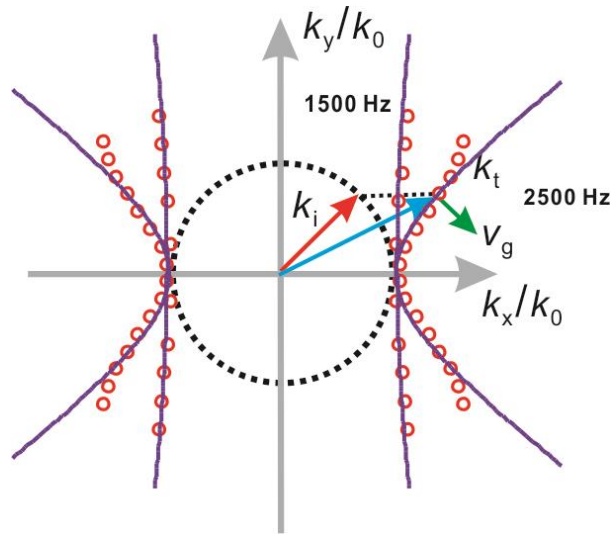


Figure 3.5 Calculated EFC at two selected frequencies which are both below the cutoff frequency. Solid line: lumped model. Circle mark: retrieved from numerical simulations.

We then examine the behavior of the AHMM using real structures numerically. An AHMM unit cell with proper periodic conditions is simulated and the band structure is depicted in Fig. 3.6. The details of calculating the band structure is given in Appendix B. In the  $x_2$ - $\Gamma$  direction ( $\Gamma$  is the center of the first Brillouin zone) where the plates are perpendicular to, there is band gap below around 2.7 kHz, which is roughly the first resonance frequency of the plates. In the  $\Gamma$ - $x_1$  direction, the dispersion curve is a straight line, indicating that the unit cell is not dispersive in the  $\Gamma$ - $x_1$  direction, since no plates exist in this direction. These results clearly show that the AHMM unit cell has different characteristics along orthogonal directions, which contribute to the hyperbolic dispersion. By solving the eigenfrequencies of the unit cell inside the first Brillouin zone, a 3D band structure can be obtained, the corresponding dispersion relation at relevant frequencies can then be retrieved by cutting a plane at these frequencies, as shown by the circle marks in Fig. 3.5.

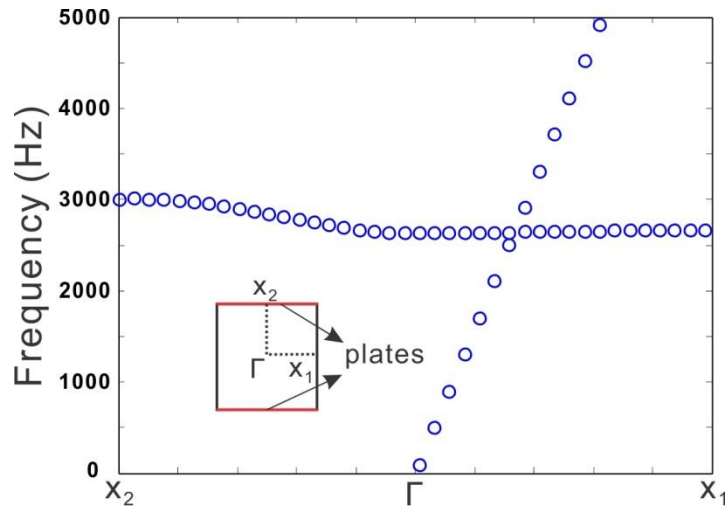


Figure 3.6 Band structure of the AHMM unit cell. The inset illustrates the unit cell and the plates.

### 3.2.2 Negative Refraction

By combining the dispersion relation of free space and the hyperbolic medium, the refraction angle of an incident wave vector  $k_i$  with vertical component  $k_y$  can be calculated as:

$$\theta_r = \pm \tan^{-1} \frac{\rho_x}{\rho_y} \left( k_y / \left( \rho_x \left( \frac{\omega^2}{B} - \frac{k_y^2}{\rho_y} \right) \right)^{\frac{1}{2}} \right) \quad (3.8)$$

The sign should be determined so that the refraction angle has the opposite sign with  $k_y$  when  $\rho_y$  is negative. The refraction angle  $\theta_r$  therefore lies in the same side with the incident angle, indicating negative refraction. This can be understood from Fig. 3.5, where the incident wave (red arrow) reaches the interface of free space and AHMM, the corresponding wave vector inside the AHMM (blue arrow) has the same vertical component ( $k_y$ ) with the incident wave due to momentum matching. The group velocity  $v_g$  then takes the same side with the incident wave vector, since it must lie normal to the EFC.

Since negative refraction plays a crucial role in AHMMs, we first investigate this phenomenon numerically using commercial package COMSOL Multiphysics 5.1. Experiments demonstrating negative refraction are not carried out here because of the finite size of the sample, since the shifted distance will be small and difficult to measure for the given sample.

The effect of negative refraction can be demonstrated by a long AHMM slab placed in front of a Gaussian beam. For quantitative analysis, the shifted distance of the beam is

estimated and compared between the real structure model and theoretical effective medium model.

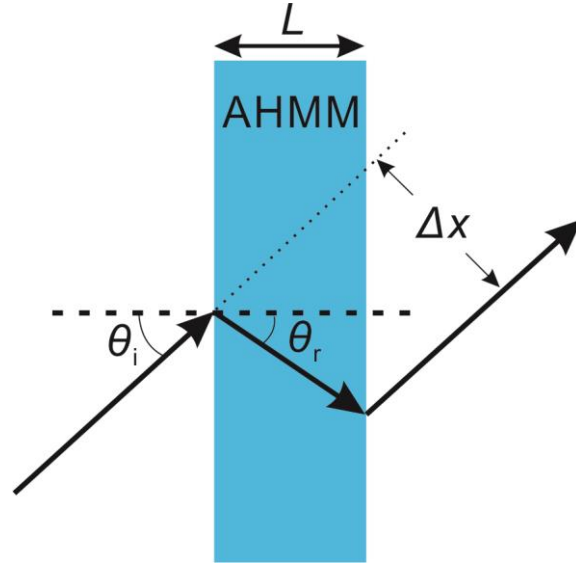


Figure 3.7 The simulation setup for negative refraction. This behavior can be quantitatively evaluated by examining the shifted distance  $\Delta x$  of the beam.

For an incident beam with an incident angle of  $\theta_i$ , the shifted distance can be calculated as:

$$\Delta x = \frac{L \cos(\theta_i - \theta_r)}{\cos \theta_r} \quad (3.9)$$

where the refraction angle  $\theta_r$  can be estimated by Eq. (3.8). Equation (3.9) provides the analytically predicted shifted distance for the effective medium model. For comparison, the real structure of AHMM is simulated in COMSOL and the shifted distance is estimated as well.

The pressure field showing negative refraction using real structure is depicted in Fig. 3.8(a) at a frequency of 2450 Hz. The thickness of the slab is  $L = 30.2$  cm (same with the fabricated sample). Figure 3.8(b) shows the theoretical and simulated shifted distance for an AHMM with a beam incident angle of  $\theta_i = 45^\circ$ . The distance gradually increases as the frequency goes higher, as  $\rho_y$  approaches zero and the corresponding refraction angle becomes greater. The results agree well, both demonstrating a broadband negative refraction phenomenon below the cutoff frequency of the plates.

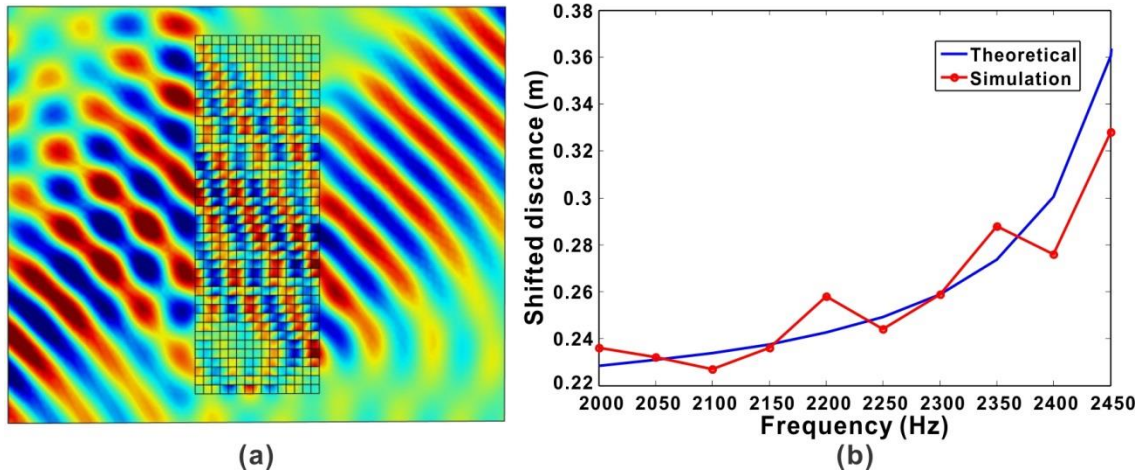


Figure 3.8 (a) Numerical demonstration of negative refraction using at 2450 Hz. (b) Theoretical and simulated shifted distances.

### 3.2.3 Partial Focusing and Subwavelength Imaging

Because negative refraction occurs at the interface between free space and AHMM medium, for a point source located in front of the sample, the refracted wave will be redirected and focused inside or on the back of the sample, depending on the geometry and constitutive parameters. A rigorous analysis based on ray tracing reveals that, for the

hyperbolic metamaterial, not all waves will refocus at the same point, in other words, this is not an ideal focusing but should be termed as “partial focusing”<sup>41</sup>. This is an intrinsic difference between hyperbolic metamaterial and an isotropic negative index metamaterial, where an ideal focal point can be generated. As seen from Fig. 3.3, at frequencies sufficiently below the cutoff frequency,  $\rho_y$  becomes deep negative (that is, the magnitude becomes larger while the sign remains negative). According to Eq. (3.8), the resulting refraction angle would approach zero, indicating that the focusing effect cannot be observed for an AHMM with a finite size. Since the fabricated AHMM is about 1-2 wavelengths at frequencies of interest, partial focusing effect can be best observed when the absolute value of  $\rho_y$  is comparable to the background medium, which occurs at frequencies relatively close but below the cutoff frequency.

By rearranging terms in the dispersion equation, one can see that  $k_x^2 = \rho_x \left( \frac{\omega^2}{B} - \frac{k_y^2}{\rho_y} \right)$ ,

which indicates that in the absence of losses, there does not exist a value for  $k_y$  so that  $k_x^2 < 0$  since  $\rho_y$  is negative and  $\rho_x$  is positive. Consequently, all waves inside the AHMM are in propagating mode and no evanescent solutions are allowed. In other words, at an arbitrary incident angle, the evanescent wave reaching the surface of the AHMM can excite the propagating mode. Furthermore, the EFC becomes flat at frequencies sufficiently below the cutoff frequency, as the absolute value of the effective density in the y-direction is large. It can be predicted from Fig. 3.5 that at low frequencies, the refracted acoustic waves would be collimated along the x-direction and funneled through the AHMM. Altogether, subwavelength information can be transferred to the opposite side of the AHMM and subwavelength imaging is possible.

Both numerical simulations and experiments are conducted to validate the AHMM for partial focusing and subwavelength imaging. The setup for experiment of partial focusing is depicted in Fig. 3.9 where a loudspeaker mimicking a point source is placed 170 mm away from the front face of the sample. The channels in the sample are facing normally to the loudspeaker and the plates are facing the other direction. The measurement is conducted inside a 2D waveguide. Sound absorptive foams are placed on the edges of the 2D waveguide and two sides of the AHMM sample to minimize the reflection and sound field interference behind the AHMM, respectively. The loudspeaker transmits pulsed signals at various center frequencies with a bandwidth of 1 kHz and the acoustic pressure fields are measured behind the sample. The field mapping measurements are performed using a scanning microphone having a diameter of 10 mm. The size of the microphone is thus one order of magnitude smaller than the relevant wavelength, and is therefore considered not to have interference with the acoustic field on the scan area. The scan area is 520 mm×800 mm and the scanning step size is 20 mm. At each position the acoustic signal is averaged over five measurements. All the signals are then aligned with a same reference signal, so that both amplitude and phase information can be restored. After scanning, the frequency-domain acoustic fields are obtained via the Fourier transform.

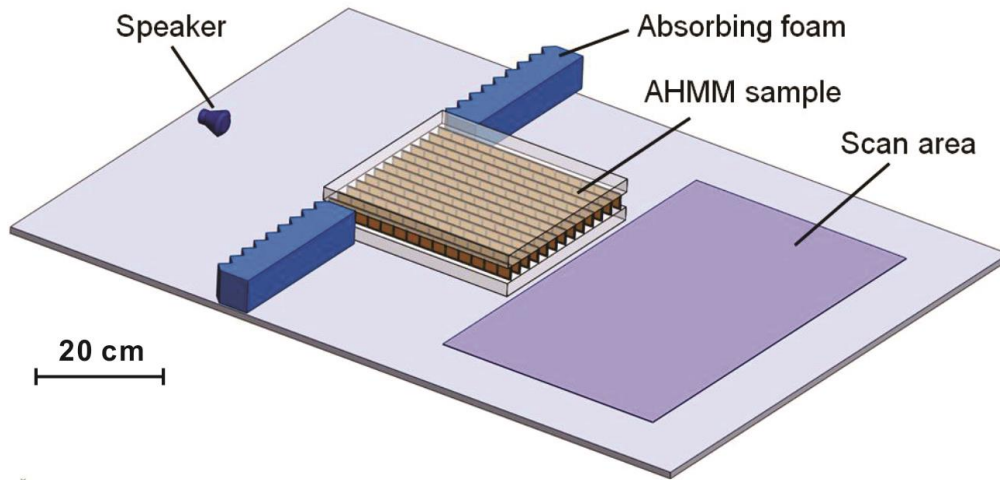


Figure 3.9 Experiment setup for partial focusing.

Figure 3.10 shows the simulated and measured acoustic pressure fields at 2440 Hz for both cases where the AHMM is present and absent. The acoustic energy is focused on the back of the AHMM and diverges behind the AHMM, as shown by both simulations and experiments. Top two figures show the simulation results for the entire domain. Left one is with AHMM and right one is without AHMM. Bottom figures compare the simulation and measurement in the scanning area. The solid white box, dashed black box and solid black box denote absorbing foam, AHMM and scan area, respectively. The measurement agrees well with the simulation in terms of the pressure pattern.

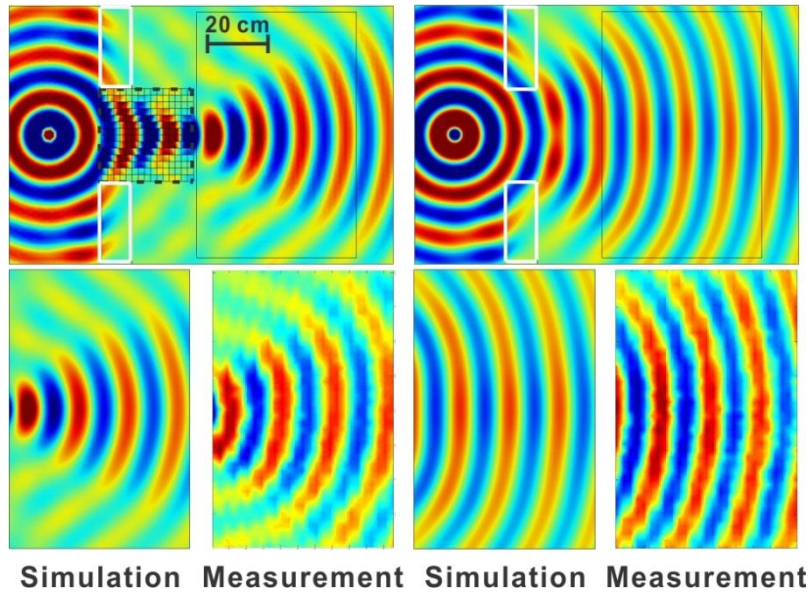


Figure 3.10 Simulated and measured acoustic fields showing partial focusing at 2440 Hz.

The pressure magnitude distributions on the exiting surface of the AHMM are also examined and depicted in Fig. 3.11. Two types of simulations are performed. One uses the real structure of the AHMM and the other one uses effective medium with properties given by Fig. 3.3. The solid blue curve, dashed blue curve, solid red curve and solid black curve represent measurement with AHMM, measurement without AHMM, simulation using real structure and simulation using effective medium, respectively. A focused profile can be clearly observed. Several factors could contribute to the small discrepancy between the measurement and simulation results: inherent microphone measurement errors (finite size effect, noise, directivity, etc.); some sound could still go through the absorbing foams and interfere with the sound field in the scanning area; the simulation assumes an ideal situation in which the frames are infinitely small and perfectly rigid. Although only partial focusing is achieved, the AHMM may still be favorable over an isotropic negative index metamaterial in terms of energy focusing as it is less sensitive to

material loss<sup>42</sup>. When the frequency is above the cutoff,  $\rho_y$  becomes positive and the EFC of the structure changes from a hyperbolic on to an elliptical one. The refractive index also changes from negative values to positive values. The resulting acoustic pressure field will no longer show a focused profile. The acoustic fields at 2.9 kHz are shown in Fig. 3.12 with and without the AHMM. Indeed, the energy focusing cannot be observed at this frequency, as the acoustic waves gradually diverge inside and behind the AHMM.

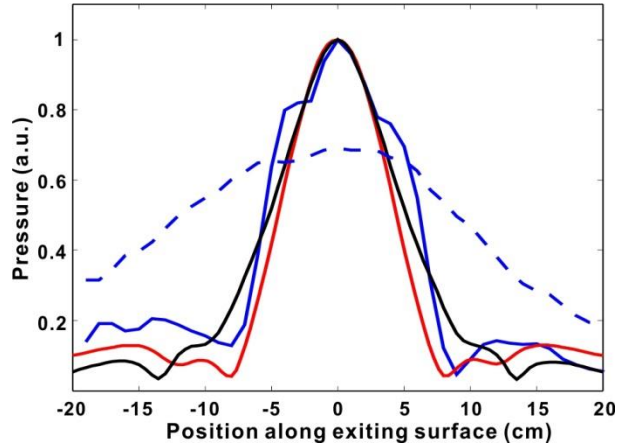


Figure 3.11 Normalized pressure magnitude distributions on the exiting surface of the AHMM.

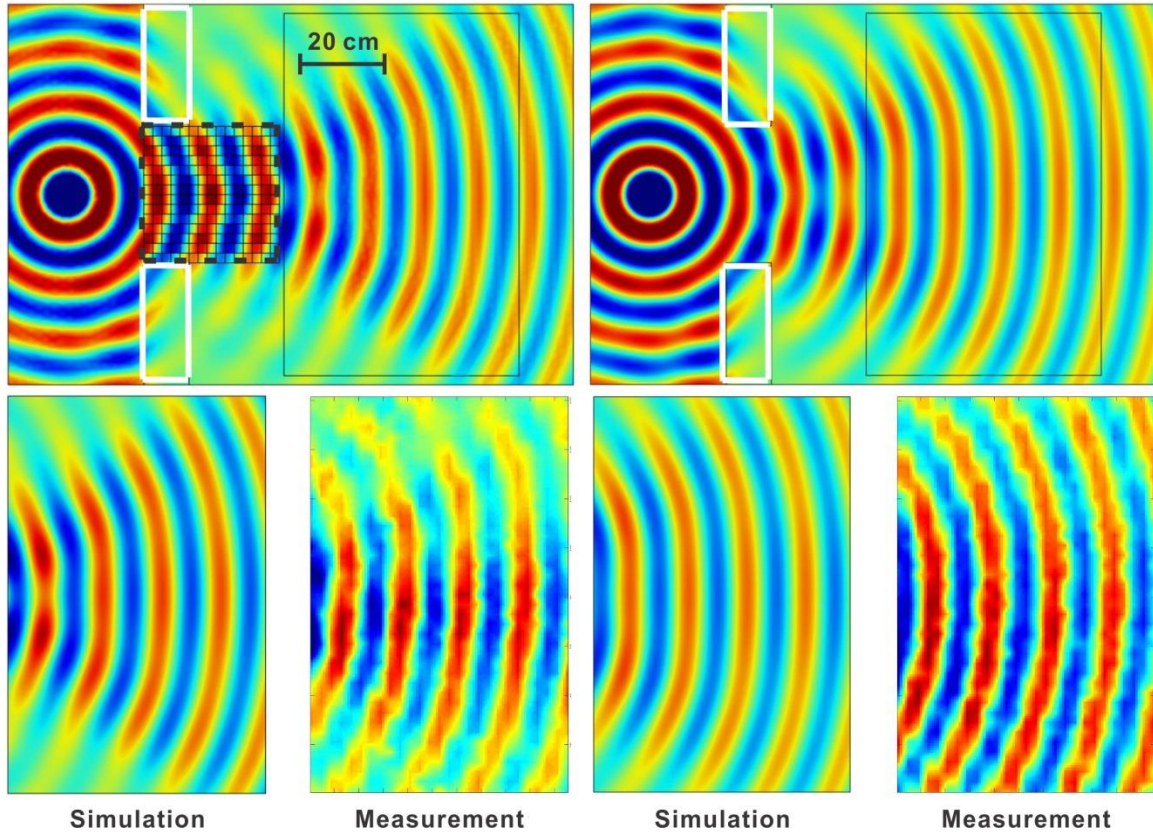


Figure 3.12 Simulated and measured acoustic fields at 2.9 kHz.

The AHMM is also capable of subwavelength imaging as abovementioned. To demonstrate this, a perforated panel with two square holes is placed in front of the AHMM, creating two in-phase sources separated by approximately 66 mm. The acoustic field is measured on the exiting surface of the AHMM at frequencies between 1 kHz and 1.6 kHz. The separating distance therefore corresponds to  $\lambda/5.2$ -  $\lambda/3.2$  ( $\lambda$  is the wavelength). The thickness of the AHMM corresponds to  $0.9\lambda$ - $1.4\lambda$ . Experimental results are shown in Fig. 3.13. At 1.1 kHz, two peaks are clearly resolved when the AHMM is present (Fig. 3.13(a)), the resolved resolution is about  $1/4.7$  of the wavelength. The normalized acoustic intensity distribution along the exiting surface of the AHMM clearly shows two peaks, while the control case (without AHMM) shows a single peak. When

the AHMM is absent, the waves radiated by the two sources merge and the resulting acoustic pressure field shows only one pronounced peak. Figure 3.13(b) demonstrates the broadband performance of the AHMM for subwavelength imaging. Two peaks can be observed for all frequencies within the frequency range tested.

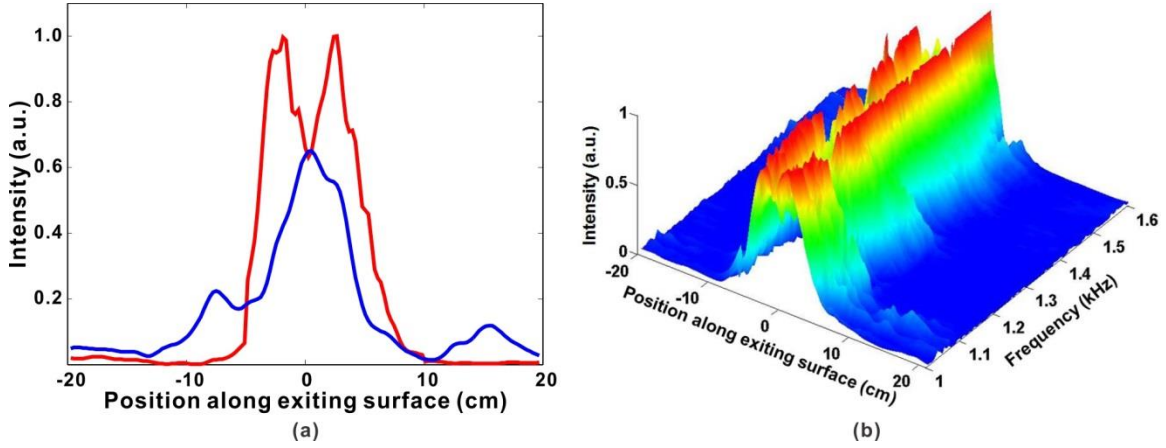


Figure 3.13 Measured acoustic fields demonstrating subwavelength imaging. (a) Imaging performance of the AHMM at 1.1 kHz. (b) The broadband performance of subwavelength imaging of the AHMM.

To understand physically the effect of subwavelength imaging, the transmission coefficients for acoustic waves propagating through the AHMM is examined. For both propagating and evanescent waves transmitting through a layer of anisotropic medium from free space, the transmission coefficient is given by<sup>43</sup>:

$$T = \frac{4Z_x Z_{0x} e^{jk_x L}}{(Z_x + Z_{0x})^2 - (Z_x - Z_{0x})^2 e^{2jk_x L}} \quad (3.10)$$

where  $Z_x = \omega\rho_x / k_x$  and  $Z_{0x} = \omega\rho_0 / k_{0x}$  are the wave impedances,  $L$  is the thickness of the layer,  $k_{0x} = \sqrt{k_0^2 - k_{0y}^2}$  and  $k_x$  are wave vectors in free space and the anisotropic medium, respectively. Note that  $k_y = k_{0y}$ , and the wave vector  $k_x$  can be obtained by:

$$k_x = \sqrt{\rho_x \left( \frac{\omega^2}{B} - \frac{k_y^2}{\rho_y} \right)} \quad (3.11)$$

where  $B$  is the bulk modulus of the medium (same for the background medium and AHMM in our case),  $\rho_x$  and  $\rho_y$  are the effective densities along x- and y-directions, respectively.

Figure 3.14 shows the transmission coefficients of the AHMM sample and free space at 1.1 kHz using Eq. (3.10). The effective densities of the AHMM are taken from Fig. 3.3 and are  $\rho_x = 1.2 \text{ kg/m}^3$ ,  $\rho_x = -75 \text{ kg/m}^3$ . For evanescent waves, i.e.,  $k_{0y} > k_0$ , it can be seen that when AHMM is present, the transmission coefficient is much higher than the control case (free space). For propagating waves, the transmission coefficients for both cases are almost unity, except when  $k_{0y}$  approaches  $k_0$ , the transmission coefficient through the AHMM drops. This means that the evanescent wave components, containing subwavelength information, are converted into the propagating components and the energy is transferred to the image plane through the AHMM, while in the control case the evanescent wave components decay very quickly and cannot reach the image plane.

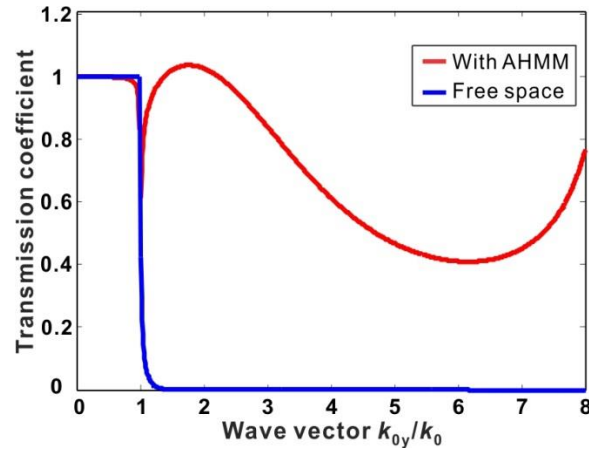


Figure 3.14 Enhanced transmission of evanescent waves across the AHMM sample at 1.1 kHz.

### 3.3 Material Loss in Anisotropic Density Near-zero Metamaterials

We now continue to examine the unique behavior of anisotropic density near-zero metamaterials. Following the concept of epsilon-near-zero (ENZ) metamaterials in electromagnetic waves, density-near-zero (DNZ) metamaterials have been proposed in the acoustic regime, showing exciting potential for controlling acoustic waves<sup>44,45</sup>. For example, subwavelength imaging and extraordinary transmission using DNZ metamaterials have been proposed<sup>43,46</sup>. In ENZ metamaterials, material loss has been demonstrated to introduce transparency, omni-directional collimation, and counterintuitively, improved transmission<sup>47,48</sup>. However, little work has been done to investigate the effect of material loss in acoustic anisotropic density-near-zero (ADNZ) metamaterials. Inspired by the study on ENZ metamaterials, this section will examine the effect of material loss in ADNZ metamaterials where only one component of the mass density tensor is close to zero.

### 3.3.1 Loss-induced Enhanced Transmission

Consider a homogeneous ADNZ medium whose effective density is positive in the x-direction and near-zero in the y-direction, i.e.,  $\rho_x > 0$  and  $\rho_y \rightarrow 0$ . The general dispersion relation for a two-dimensional scenario is Eq. (3.7). To include material loss in the ADNZ medium,  $\rho_y$  is now considered as a complex number having the form  $\rho_y = \text{Re}(\rho_y) + j\text{Im}(\rho_y)$ . Without losing generality, the background medium is assumed to be air with density  $\rho_0$ , and  $\rho_x = \rho_0 = 1.2 \text{ kg/m}^3$ . The EFCs of three different cases are plotted in Fig. 1 based on Eq. (3.7), with the same  $\text{Re}(\rho_y) = 0.02$  and different losses  $\text{Im}(\rho_y) = -0.2$ ,  $\text{Im}(\rho_y) = -2$ , and  $\text{Im}(\rho_y) = -20$ . These three values correspond to low loss, moderate loss, and high loss, respectively. The EFC of the ADNZ medium is represented by a solid curve and the EFC of free space is represented by a dashed curve for comparison. The incident wave vector  $k_i$  has a  $30^\circ$  incident angle.

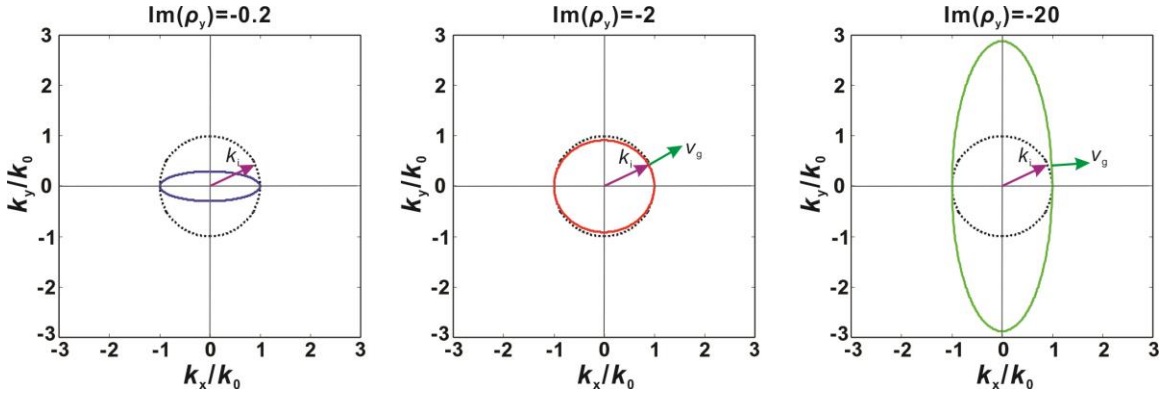


Figure 3.15 EFC of an ADNZ medium with low, moderate and high losses. Dashed line represents the free space.

It can be seen from Fig. 3.15 that the general EFC of the lossy media is an ellipsoid. When the material loss increases, the major axis of the ellipsoid changes from the horizontal axis to the vertical axis. For an incoming plane wave with incident wave vector  $k_i$ , incident and transmitted waves should have the identical y-component wave vector due to the conservation of momentum. For a  $30^\circ$  incident beam, it is indicated by Fig. 3.15 that, for the low loss case, the corresponding  $k_x$  inside ADNZ medium has no solutions since no  $k_y$  component can be found on the EFC matching the free space  $k_{0,y}$  component. However, for the moderate and high loss cases,  $k_x$  exists, indicating wave propagation is allowed in the medium. As the group velocity  $v_g$  must lie normal to the EFC, for the high loss case, the transmitted wave vector is pointing in the x-direction since the EFC is almost flat. Therefore, the transmitted energy is collimated towards the normal direction if a large material loss is introduced.

We further investigate the transmission characteristics of the ADNZ slab with various losses. The transmission coefficient for both propagating and evanescent waves transmitting through an anisotropic layer is given in Eq. (3.10). Figure 3.16 shows the transmission coefficients at 2545 Hz for  $L=30$  cm with effective densities abovementioned used. It can be seen that for normal incidence ( $k_{0,y} = 0$ ), the transmission coefficients are high in all three cases. This is because the impedance in the x-direction  $Z_x$  matches with the free space impedance  $Z_0$ , as  $k_{0,y}$  is zero. For oblique incidences, especially for large incident angles (large  $k_{0,y}$  values), the transmission coefficients for both propagating and evanescent waves increase significantly when more loss is induced. For the low loss case, the transmission coefficient quickly drops to very small values as

$k_{0y}$  increases, implying no propagating mode is allowed in the medium. Note that as illustrated in Fig. 3.15, sound energy mainly propagates in the x-direction for a large material loss. We hereby evaluate the value of  $Z_x$  in terms of  $\text{Im}(\rho_y)$ .

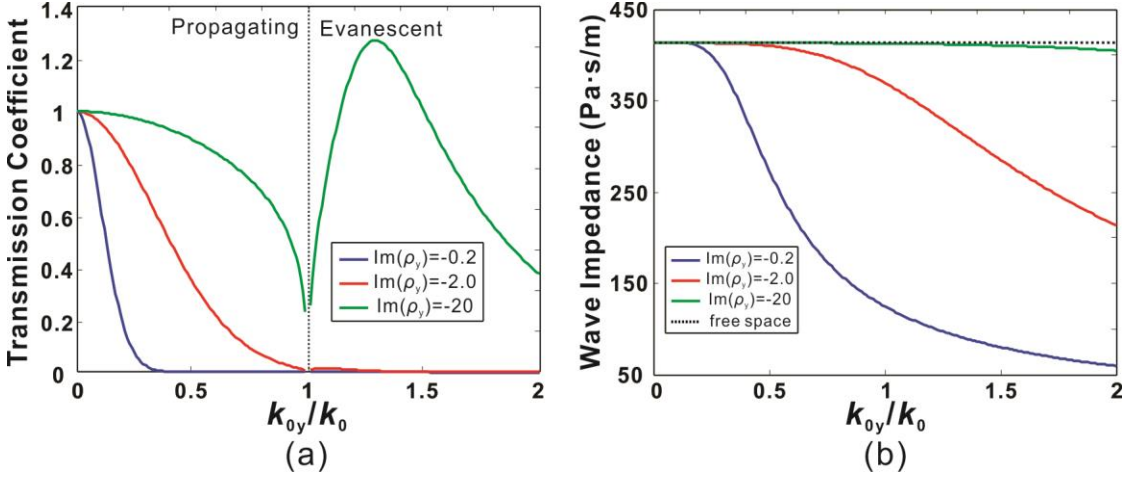


Figure 3.16 (a) Transmission coefficients of the ADNZ medium with various losses. (b)

The x-direction wave impedance of the ADNZ medium with various losses.

The wave vector  $k_x$  inside the ADNZ medium is given by Eq. (3.11), the wave impedance  $Z_x$  is thus:

$$Z_x = \omega \sqrt{\rho_x / \left( \frac{\omega^2}{B} - \frac{k_y^2}{\rho_y} \right)} \quad (3.12)$$

The dependence of  $Z_x$  on  $\text{Im}(\rho_y)$  is shown in Fig. 3.16(b). As a reference, the free space impedance  $Z_0 = \rho_0 c_0$  is also included in the figure. It can be clearly observed that for large material losses, the impedance matching condition is fulfilled within a broad range of  $k_{0y}$  starting from 0. These results are not surprising, as we can observe higher

transmission in Fig. 3.16(a) for a certain  $k_{0,y}$  value with large losses. We also note that the enhanced transmission when  $k_{0,y} > 1$  implies that the evanescent components can be coupled through an ADNZ slab and is favorable for subwavelength imaging applications<sup>49</sup>.

### 3.3.2 Numerical Simulations

We now verify the proposed phenomenon with numerical simulations. The ADNZ medium is constructed utilizing plate-type acoustic metamaterials outlined in the previous sections. The 2D ADNZ metamaterial is the same with Fig. 3.4(a) where periodically arranged, clamped square plates facing the y-direction are placed inside a 2D waveguide. The plates also have the same material properties in section 3.1. Different material losses are now considered to give rise to complex effective density in the y-direction. To this end, one-dimensional (1D) models are first utilized to study the effective density of the ADNZ metamaterial. Finite element package COMSOL MULTIPHYSICS is adopted for numerical simulations.

The effective density along the x-direction is considered as that of air and therefore  $\rho_x = 1.2 \text{ kg/m}^3$ . The procedure for evaluating the complex effective density of the ADNZ metamaterial in the y-direction is still the lumped model outlined in section 3.1. Note that the Young's moduli of the plates are set to be complex numbers, i.e.,  $E = \text{Re}[E] + j \text{Im}[E]$ , to include material loss in the simulations. The same real parts of the Young's moduli are used, i.e.,  $\text{Re}[E] = 2.61 \text{ GPa}$ . Three values are chosen for the imaginary parts:  $\text{Im}[E] = 0.0261 \text{ GPa}$ ,  $\text{Im}[E] = 0.261 \text{ GPa}$  and  $\text{Im}[E] = 2.61 \text{ GPa}$ . The

corresponding loss factors ( $\tan \delta$ ) are 0.01, 0.1, and 1. They correspond to low, moderate and high loss case, respectively.

Figure 3.17 depicts the calculated effective density of the three cases. Since the real part is loss-independent, it is only represented by a single curve. The imaginary part, on the other hand, varies with the material loss. It can be found from Fig. 4 that with higher material loss, the absolute value of the imaginary part of  $\rho_y$  increases. The real part of  $\rho_y$  is near zero ( $\text{Re}(\rho_y) = 0.02$ ) around 2545 Hz and the corresponding  $\text{Im}(\rho_y)$  is -0.2, -1.9, and -18.8, respectively.

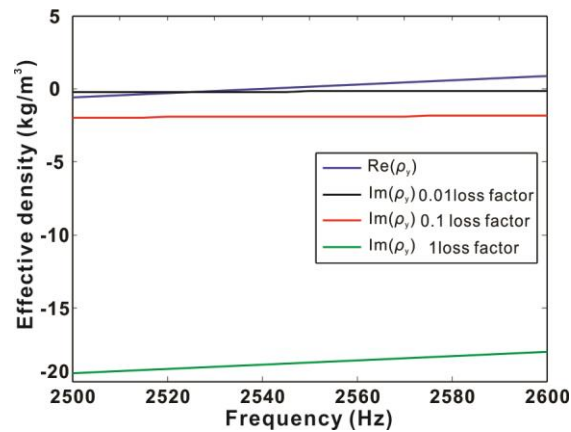


Figure 3.17 Effective density along the y-direction with different losses.

Full wave simulations based on real structures are carried out to study the enhanced transmission for loss-induced ADNZ metamaterials. A Gaussian beam with frequency 2545 Hz is transmitted with an incident angle  $30^\circ$  to the ADNZ metamaterial slab. The corresponding acoustic pressure and intensity fields are plotted in Fig. 3.18. The top shows the acoustic pressure field for real structures, for better comparison, simulations using effective medium is also performed and is shown in the middle, the dashed line

denotes the interface between free space and ADNZ medium. The bottom shows the acoustic intensity fields for real structures, which correspond to the top figures. It is clear that for the low loss case, the incident wave cannot excite propagating modes inside the ADNZ medium and the acoustic energy vanishes quickly inside the slab. When the loss increases, higher transmission is observed, and the acoustic energy is collimated in the x-direction, which is well predicted by the theory presented above. This seems to be counterintuitive, as more material losses increase the transmission. However, a rigorous analysis of the EFC shows that in the high loss case, the acoustic waves are forced to travel along the x-direction (Fig. 3.15(c)), where there are no plates and therefore no energy loss in that direction (Fig. 3.18(c)). This is consistent with the fact that the homogenized acoustic medium does not yield loss in the x-direction.

It should be noted here that by increasing the magnitude of the effective density along the y-direction ( $\rho_y$ ) will also enhance the transmission coefficient for oblique incidence. For example, by increasing the real part of  $\rho_y$  will also increase the transmission coefficients for both propagating and evanescent waves, which can be confirmed by Eq. (3.10). It shall be pointed out, however, the material loss provides an alternative means to tune the transmission of anisotropic metamaterials. Moreover, for a given material, the real part of the effective density is not always easy to be tailored, and may not yield relatively large amplitude as it will do for the imaginary part. In this way, material loss is favorable in tuning the transmission characteristics of anisotropic acoustic metamaterials.

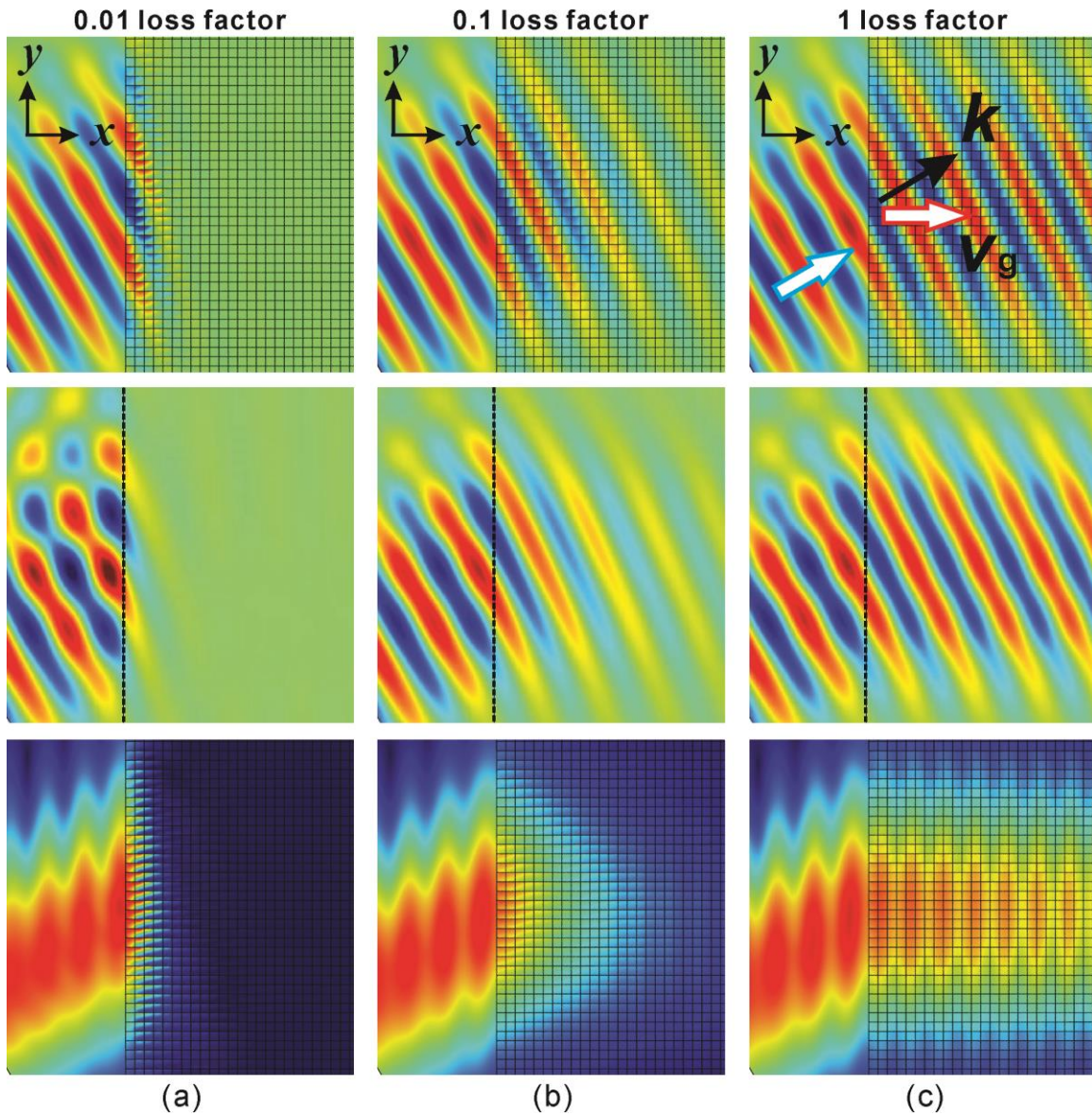


Figure 3.18 The acoustic pressure and intensity fields. Top: acoustic pressure fields from real structure. Middle: acoustic pressure fields from effective medium. Bottom: acoustic intensity fields from real structure. (a) Low loss. (b) Moderate loss. (c) High loss.

To demonstrate acoustic imaging with resolution below the diffraction limit, two square acoustic sources with width 2 cm are placed in front of the ADNZ slab with thickness 30 cm, corresponding to  $2.23 \lambda$  ( $\lambda$  is the wavelength) at 2545 Hz. The separation of the

sources is 6 cm, corresponding to  $1/2.25\lambda$ . The resulting normalized acoustic pressure amplitude distribution on the other side of the ADNZ slab is depicted in Fig. 3.18 with different loss factors. Two peaks can be clearly resolved for the high loss case, owing to the enhanced transmission of evanescent waves. The pressure amplitude profile shows only one peak for other cases, as the evanescent wave energy cannot be coupled through the ADNZ slab, as indicated by Fig. 3.16.

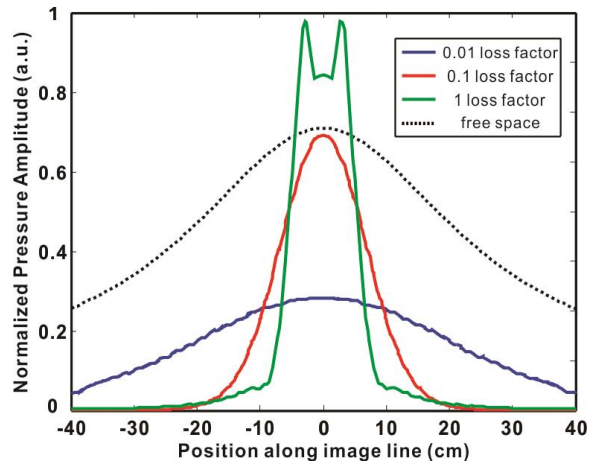


Figure 3.19 Pressure amplitude distribution on the image plane for different loss factors.

### 3.4 Summary

In this chapter, we have designed, fabricated, and tested a broadband AHMM based on plate-type acoustic metamaterials. The effective density of the plates is first evaluated using a semi-analytic method. The truly hyperbolic dispersion is then verified by partial focusing and subwavelength imaging through experiments. The proposed AHMM in this study can be scaled down to operate at much higher frequencies. However, it should be borne in mind that the required high-resolution fabrication can pose a challenge. For example, the unit cell length could be in the 100 micron range for an operating frequency

around 1 MHz in water. The proposed AHMM may find usage in angular filtering<sup>50</sup>, medical imaging and non-destructive testing. The proposed design can be readily extended to achieve 3D AHMMs. The effect of material loss is also discussed when the effective density is approaching zero. It is expected that the results of this chapter will provide a new design methodology for the realization of acoustic metamaterials requiring anisotropic densities.

## Chapter 4 Complementary Acoustic Metamaterial

A good yet powerful way to design acoustic metamaterials is to borrow ideas from other classes of metamaterials, especially electromagnetic metamaterials, as there exist a lot of analogy between acoustic waves and electromagnetic waves<sup>51</sup>. It is not surprising that many concepts were first demonstrated in electromagnetic regime, and were later realized using acoustic waves<sup>52</sup>. One of the most interesting examples is the complementary metamaterial (CMM), which is designed to have complementary equivalent parameters with real materials<sup>53</sup>. In this way, the presence of the real material is canceled out by the CMM and the electromagnetic waves propagating through these materials will be preserved and behave like in vacuum. Following this idea, several design schemes had been proposed for electromagnetic cloaking or illusion, and opening up virtual holes in a wall without distortion<sup>54,55</sup>. The most significant advantage of this approach is that it allows interaction of the cloaked object with the outer space. Similar concepts of acoustic cloaking with single negative parameters were also proposed for cloaking in free space<sup>56</sup>. More feasible designs were carried out for complementary acoustic cloaking using effective medium approach<sup>57,58</sup> where the simulations were based on homogenized effective media, and no explicit designs were given.

In this chapter, we aim to fill the long-standing gap between the theory of CMM and its design in the context of acoustics and to further apply it to ultrasound transmission through aberrating layers.

#### 4.1 Background and Motivation

In many medical ultrasound and nondestructive evaluation applications, ultrasonic waves need to be transmitted through an aberrating layer<sup>59-61</sup>, where either transmission is desired to be maximized or the reflection needs to be minimized. One of the most representative examples is transcranial ultrasound beam focusing, which could be useful in both brain imaging and treatment<sup>60,61</sup>. However, transcranial beam focusing is extremely challenging because there is a large impedance mismatch between the skull and the tissue. A common approach to achieve transcranial beam focusing is based on the time-reversal or phase-conjugate technique and ultrasound phased arrays<sup>62,63</sup>. Although the focal position can be restored, one significant shortcoming of this strategy is that it does not compensate for the large acoustic energy loss due to the impedance mismatch between the skull and human tissue. Recent development of acoustic metamaterials could open up the possibility for noninvasive ultrasound transmission through aberrating layers. By tailoring the effective properties, an acoustic metamaterial could be used to cancel out or cloak the aberrating layer, allowing the acoustic wave to pass through the layer without energy loss. The concept is illustrated in Fig. 4.1, where the acoustic energy is blocked by the aberrating layer due to the large impedance mismatch, while it can transmit with high efficiency if placing the desired CMM adjacent to the aberrating layer.

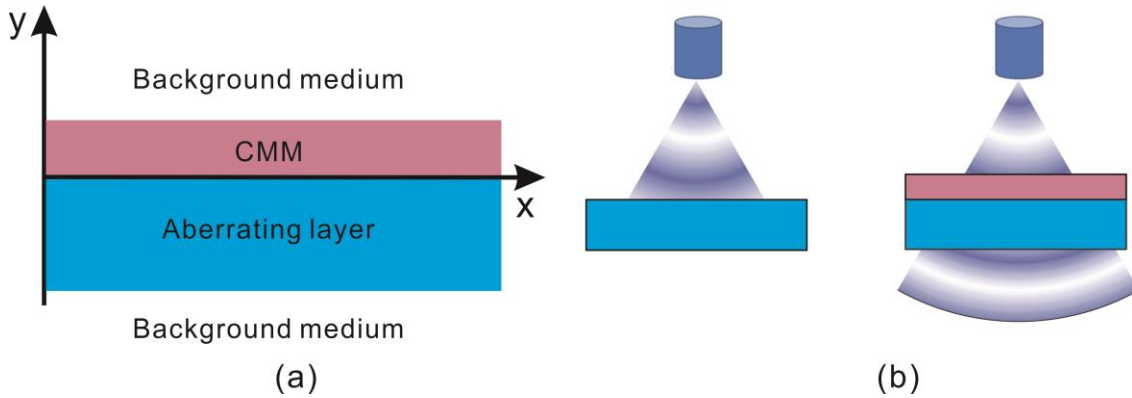


Figure 4.1 (a) Schematic of the CMM, the aberrating layer, and the background medium.

(b) Concept of the CMM for enhancing the sound transmission.

Conventional cloaking strategies<sup>10,11</sup>, on the other hand, compress or rotate the space and hide the object inside an enclosure in which the object has no interaction with the outside world; therefore, it is not suited to the problem of interest in this study. As we have discussed in the previous section, CMM incorporate well with this shortcoming and is thus chosen for dealing with the problem here. In particular, side-branch based metamaterials and plate-type acoustic metamaterials, described in chapters 2 and 3, are adopted for the design of the CMM.

## 4.2 Anisotropic Complementary Metamaterial

A generalized CMM requires negative and anisotropic properties simultaneously and preferably should not be resonance based because of the large damping effect associated with resonance. We present here a design of a quiai-2D acoustic CMM utilizing clamped plates and side branches. By assigning plates in different directions with different thicknesses, the effective density is shown to be both anisotropic and negative at the operating frequency. We then show the proposed CMM can effectively cancel out

aberrating layers in order to allow the sound to pass through with strongly enhanced transmission and reduced acoustic field distortion.

#### 4.2.1 Transformation Acoustics

Transformation acoustics, which is a powerful tool for designing acoustic metamaterials, has enabled numerous possibilities in manipulating acoustic waves versatily<sup>64</sup>. Similar to other many other concepts in the field acoustic metamaterials, this was first introduced in electromagnetic regime<sup>65,66</sup>. The transformation of coordinates in real spaces makes acoustic waves travel as if they are in virtual spaces. Acoustic metamaterials, on the other hand, provide a feasible way for achieving the desired field properties.

We first give a brief derivation of the required CMM properties in order to cancel out a certain aberrating layer. The CMM is placed on top of the aberrating layer, as illustrated in Fig. 4.1(a). The aberrating layer is assumed to be sufficiently long so that the edges do not significantly affect the acoustic field. The CMM compresses and cancels the information of the selected aberrating layer. Let  $\rho^{(c)}(x^{(c)}, y^{(c)}, z^{(c)})$ ,  $\beta^{(c)}(x^{(c)}, y^{(c)}, z^{(c)})$  and  $\rho^{(a)}(x^{(a)}, y^{(a)}, z^{(a)})$ ,  $\beta^{(a)}(x^{(a)}, y^{(a)}, z^{(a)})$  be the effective density and compressibility tensors of the CMM and the aberrating layer, respectively.  $x^{(c)}$ ,  $y^{(c)}$ ,  $z^{(c)}$  and  $x^{(a)}$ ,  $y^{(a)}$ ,  $z^{(a)}$  are generalized curved coordinates. The effective parameters of the CMM is designed so that it will cancel out with the effect of the aberrating layer, based on the acoustic coordinate transformation, we have<sup>67</sup>:

$$\left[ \rho^{(c)} \right]^{-1} = \mathbf{A} \left[ \rho^{(a)} \right]^{-1} \mathbf{A}^T / \det \mathbf{A} \quad (4.1)$$

$$\beta^{(c)} = \beta^{(a)} / \det \mathbf{A} \quad (4.2)$$

where  $\mathbf{A}$  is the Jacobian transformation tensor of compressing transformation given by:

$$\mathbf{A} = \begin{bmatrix} \frac{\partial x^{(c)}}{\partial x^{(a)}} & \frac{\partial x^{(c)}}{\partial y^{(a)}} & \frac{\partial x^{(c)}}{\partial z^{(a)}} \\ \frac{\partial y^{(c)}}{\partial x^{(a)}} & \frac{\partial y^{(c)}}{\partial y^{(a)}} & \frac{\partial y^{(c)}}{\partial z^{(a)}} \\ \frac{\partial z^{(c)}}{\partial x^{(a)}} & \frac{\partial z^{(c)}}{\partial y^{(a)}} & \frac{\partial z^{(c)}}{\partial z^{(a)}} \end{bmatrix} \quad (4.3)$$

This study focuses on 2D problems, and only wave propagation in the  $x$ - $y$  plane is of interest. The  $z$  component in the Jacobian matrix is therefore dropped. Since the length of the CMM layer and the aberrating layer are assumed to be equal, we have

$$\frac{\partial x^{(c)}}{\partial x^{(a)}} = 1 \quad (4.4)$$

Because of the coordinate transformation  $x^{(c)} = x^{(a)}$ . Without loss of generality, the thickness of the CMM is assumed to be half of the aberrating layer. The following equation needs to be satisfied because of the coordinate transformation  $y^{(c)} = -y^{(a)}$ , such that

$$\frac{\partial y^{(c)}}{\partial y^{(a)}} = -0.5 \quad (4.5)$$

This ratio is negative since the acoustic information is folded in the CMM and would cancel out with that of the aberrating layer. Other components  $\frac{\partial x^{(c)}}{\partial y^{(a)}}$  and  $\frac{\partial y^{(c)}}{\partial x^{(a)}}$  in the tensor are equal to zero, as the transformation in each direction (i.e.,  $x$ - and  $y$ -directions) are independent. For more complicated geometries, off-diagonal components may appear. They would, however, be eliminated by coordinate rotations<sup>68</sup>.

Finally, tensor  $\mathbf{A}$  reads

$$\mathbf{A} = \begin{bmatrix} 1 & 0 \\ 0 & -0.5 \end{bmatrix} \quad (4.6)$$

Consequently, the density and compressibility tensors of the CMM are

$$\rho^{(c)} = \begin{bmatrix} -0.5 & 0 \\ 0 & -2 \end{bmatrix} \times \rho^{(a)} \quad (4.7)$$

$$\beta^{(c)} = -2 \times \beta^{(a)} \quad (4.8)$$

Such a generalized CMM requires strongly anisotropic density as well as negativity for both density and compressibility. We note that the density can be isotropic if the thickness of the CMM is chosen to be the same as the aberrating layer. In this case, however, the refractive index is -1, and the  $k$  vector along the interface goes to infinity<sup>49</sup>. In other words, such a CMM will be very unit-cell-size sensitive and can be difficult to demonstrate. Furthermore, a generalized CMM is preferred in practice as its thickness can be arbitrarily chosen; i.e., it does not depend on the thickness of the aberrating layer, thus providing great flexibility.

We then further explore the potential of CMM for canceling out multiple aberrating layers and acoustic cloaking. These results will be verified numerically using effective medium approach in section 4.2.3.

We know that in practice, more than one aberrating layer could exist. To deal with this problem, multiple CMM layers can be adopted to effectively cancel out multiple aberrating layers. To demonstrate this, we here perform analysis of using two CMM layers for cancelling out two aberrating layers. The approach presented here can be generalized to problems with more than two layers.

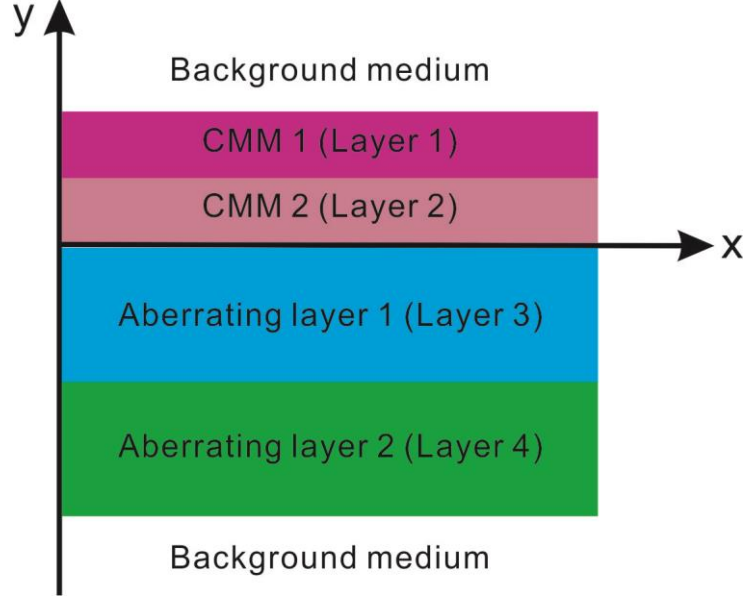


Figure 4.2 Schematic of the CMM and aberrating layers and the background medium.

Figure 4.2 shows the schematic of two aberrating layers (layers 3 and 4 have the same thickness but different acoustic properties) and two CMM layers (layers 1 and 2) which can effectively cancel out layers 3 and 4. Without loss of generality, the thicknesses of the CMM layers are assumed to be half of the aberrating layers. Here layers 1 and 2 are used to cancel out layers 4 and 3, respectively.

Let  $\rho^{(i)}(x^{(i)}, y^{(i)}, z^{(i)})$  and  $\beta^{(i)}(x^{(i)}, y^{(i)}, z^{(i)})$  be the effective density and compressibility of the  $i$ th layer,  $x^{(i)}, y^{(i)}, z^{(i)}$  are generalized curved coordinates. Performing the same coordinate transformation based on the given geometry, we have:

$$\mathbf{A} = \mathbf{B} = \begin{bmatrix} 1 & 0 \\ 0 & -0.5 \end{bmatrix} \quad (4.9)$$

where  $\mathbf{A}$  and  $\mathbf{B}$  are the Jacobian transformation tensors of transforming layer 3 and layer 4 into layer 2 and layer 1, respectively. Using Eqs. (4.1) and (4.2), the density and compressibility tensors of layers 1 and 2 read:

$$\rho^{(1)} = \begin{bmatrix} -0.5 & 0 \\ 0 & -2 \end{bmatrix} \times \rho^{(4)} \quad (4.10)$$

$$\beta^{(1)} = -2 \times \beta^{(4)} \quad (4.11)$$

$$\rho^{(2)} = \begin{bmatrix} -0.5 & 0 \\ 0 & -2 \end{bmatrix} \times \rho^{(3)} \quad (4.12)$$

$$\beta^{(2)} = -2 \times \beta^{(3)} \quad (4.13)$$

For acoustic cloaking applications, another restoring layer should be added in order to fill up the void created by CMM and aberrating layer. Figure 4.3 shows the schematic of acoustic cloaking using CMMs, where the blue dotted line denotes the boundaries of layer 4. The cloaking device consists of two layers (layer 1 and layer 2), where layer 1 maps and restores the information of layer 4, of which the scattering and transmission field will be revealed behind the aberrating layer (layer 3, which is assumed to be sufficiently long so that the edges do not significantly affect the wave field). Layer 2 is the CMM layer which compresses and cancels the information of layer 3.

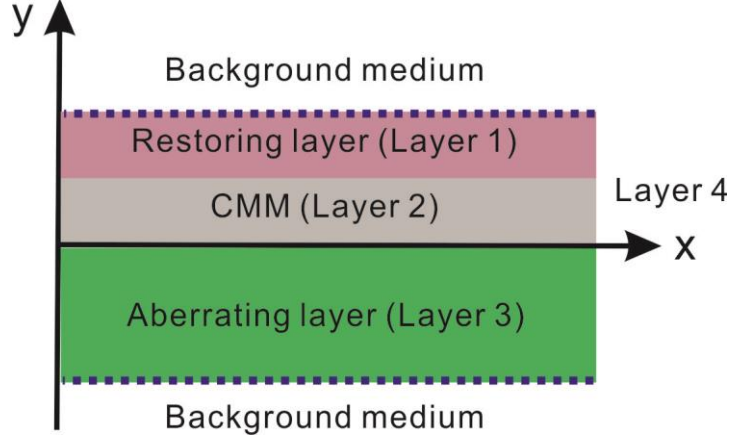


Figure 4.3 Schematic of acoustic cloaking using CMMs.

Note that layer 4 has the acoustic properties of the background medium so that the total virtual acoustic field will be homogeneous. The thicknesses of layer 1 and layer 2 are assumed to be half of layer 3 for simplification. Performing the same coordinate transformation based on the given geometry, we have

$$\mathbf{A} = \begin{bmatrix} 1 & 0 \\ 0 & -0.5 \end{bmatrix} \quad (4.14)$$

where  $\mathbf{A}$  is the Jacobian transformation tensor of folding layer 3 into layer 2.

The Jacobian transformation tensor  $\mathbf{B}$  of restoring information of layer 1 into layer 4 is given by:

$$\mathbf{B} = \begin{bmatrix} \frac{\partial x^{(1)}}{\partial x^{(4)}} & \frac{\partial x^{(1)}}{\partial y^{(4)}} \\ \frac{\partial y^{(1)}}{\partial x^{(4)}} & \frac{\partial y^{(1)}}{\partial y^{(4)}} \end{bmatrix} \quad (4.15)$$

Since layer 1 restores the acoustic information of layer 4, and it is illustrated in Fig. 4.3 that the thickness of layer 1 is 1/4 of layer 4, the following equation needs to be satisfied in the y-direction:

$$\frac{\partial y^{(1)}}{\partial y^{(4)}} = 0.25 \quad (4.16)$$

Other components of tensor  $\mathbf{B}$  are the same with tensor  $\mathbf{A}$  as only transformation in the y-direction is different.

Finally, tensor  $\mathbf{B}$  reads:

$$\mathbf{B} = \begin{bmatrix} 1 & 0 \\ 0 & 0.25 \end{bmatrix} \quad (4.17)$$

Therefore, the density and compressibility tensors of layers 1 and 2 are:

$$\rho^{(1)} = \begin{bmatrix} 0.25 & 0 \\ 0 & 4 \end{bmatrix} \times \rho^{(4)} \quad (4.18)$$

$$\beta^{(1)} = 4 \times \beta^{(4)} \quad (4.19)$$

$$\rho^{(2)} = \begin{bmatrix} -0.5 & 0 \\ 0 & -2 \end{bmatrix} \times \rho^{(3)} \quad (4.20)$$

$$\beta^{(2)} = -2 \times \beta^{(3)} \quad (4.21)$$

Using Eqs. (4.18)(4.19)(4.20)(4.21), the acoustic information of layer 3 will be canceled out by layer 2, and layer 1 will release and restore the acoustic information of the background medium so that layer 4 is virtually filled with the background medium. Layers 1 and 2 thus behave as an acoustic cloaking device. It is noted that, layer can be achieved using exactly the design we shall introduce in the next section. The density in layer 1 is anisotropic but positive, which can be realized using an existed structure<sup>11</sup>.

#### 4.2.2 Structure Design

We then continue to design the structure that exhibits the required properties given in Eqs. (4.7) and (4.8). As will be shown below, the proposed CMMs can be achieved by

periodic cubic blocks with clamped elastic plates and side branches, and they are nonresonant acoustic metamaterials.

A portion of the CMM ( $5 \times 5$  units) is shown in Fig. 4.4(a). The plate size is  $2 \text{ mm} \times 2 \text{ mm}$ , and the plate material is aluminum. The Young's modulus, Poisson's ratio and density are  $70 \text{ GPa}$ ,  $0.33$  and  $2700 \text{ kg/m}^3$ , respectively; the tension on the plate is assumed to be zero. The side branches are open ended and are introduced to tune the compressibility. The operating frequency of the CMM is  $50 \text{ kHz}$ , at which the wavelength in water (background medium) is 15 times larger than the size of the unit cell.

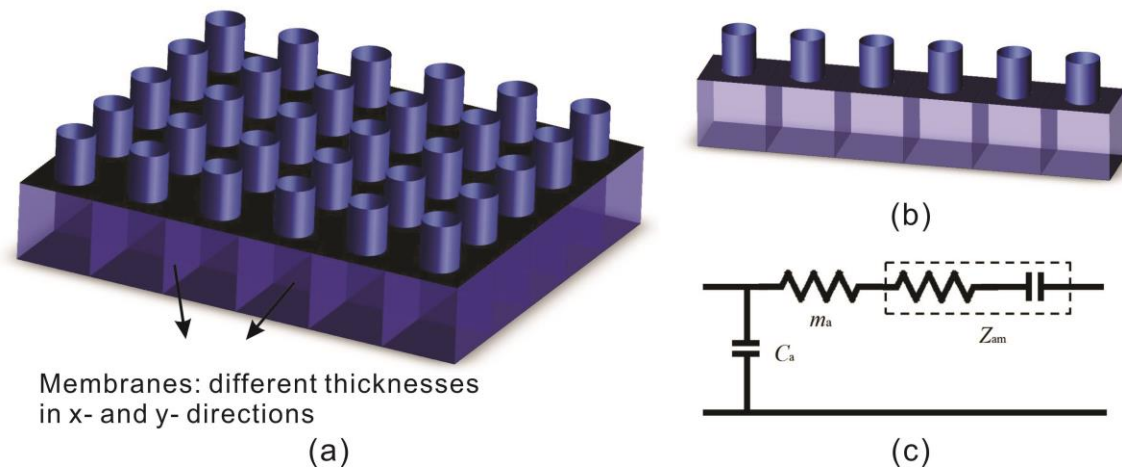


Figure 4.4 (a) Schematic of a portion of the quasi-2D CMM. (b) Schematic of a 1D side branch and plate-type metamaterial. (c) Equivalent acoustic circuit of a single unit cell of the 1D structure in (b).

By adjusting the thicknesses of the plates facing each direction ( $x$ - and  $y$ -), the effective density can be tuned therein in order to achieve anisotropy. Assuming the interaction and coupling between plates in the  $x$ - and  $y$ -directions is negligible, the effective density and compressibility in either the  $x$ - or  $y$ -direction can be estimated separately by 1D studies<sup>40</sup>.

To this end, 1D models are first carried out in order to determine the appropriate thicknesses of the plates and the dimensions of the side branches by both theoretical analysis and numerical simulations. Two separate sets of simulations are conducted for the  $x$ - and  $y$ -directions, respectively. The finite-element analysis software COMSOL 4.3b is used for all simulations. The effective density and compressibility of the proposed CMM can be extracted from numerical simulation results by a finite-difference approximation method<sup>26</sup>. On the other hand, the effective compressibility with open-ended side branches can be estimated using the method outlined in chapter 2 and is written as:

$$\beta_e = \beta_0 \left( 1 - \frac{S}{Ad\rho_0\beta_0 l_e \omega^2} \right) \quad (4.22)$$

where  $\beta_e$  is the effective compressibility,  $\beta_0$  is the background medium compressibility,  $S$  is cross section area of the branch,  $A$  is cross section area of the waveguide (cubic block),  $d$  is length of unit cell, and  $l_e$  is the effective length of the branch.

It has been demonstrated in chapter 3 that for the 1D plate-type metamaterials shown in Fig. 4.4(b), the effective density depends on the properties of the plates. The side branches are assumed to have a negligible effect on the effective density<sup>22</sup>. The effective density with clamped plates can be derived by using the lumped model similar to that in chapter 3. The difference is that the effect of the waveguide is now taken into consideration. Figure 4.4(c) shows the equivalent acoustic circuit of the 1D plate-type metamaterial, where  $m_a$  is the effective acoustic mass of the tube,  $C_a$  is the acoustic capacitance of the waveguide,  $Z_{am}$  is the acoustic impedance of the plate and can be approximated by an inductor and capacitor in series in the low-frequency region<sup>23</sup>.

$m_a$  and  $C_a$  are given by:

$$m_a = \frac{\rho_0}{A(d-h)} \quad (4.23)$$

$$C_a = A\beta_0(d-h) \quad (4.24)$$

where  $\rho_0$  is the background medium density,  $h$  is the plate thickness.

The acoustic impedance of the plate,  $Z_{am}$ , can be defined as

$$Z_{am} = \frac{\iint \Delta p A}{j\omega \xi A^2} \quad (4.25)$$

Note that this equation is the same with Eq. (3.6), and is evaluated numerically using COMSOL.

The combination of Eqs. (4.23) and (4.25) yields the expression for the total acoustic impedance of the tube:

$$Z_{as} = j\omega m_a + Z_{am} \quad (4.26)$$

The effective density of a unit cell is then given by

$$\rho_e = \frac{Z_{as} \cdot A}{j\omega d} \quad (4.27)$$

The thicknesses of the plates are 0.083 mm and 0.11 mm in the  $x$ - and  $y$ -directions, respectively.

The dimensions of the side branches are  $r=0.5$  mm,  $h=1.25$  mm, respectively, where  $r$  and  $h$  are the radius and the height of the side branch, respectively. The effective acoustic parameters retrieved from finite difference method (details given in Appendix A) are compared with the theoretical prediction and are shown in Fig. (4.5), where excellent agreement can be observed. At 50 kHz, the desired density and compressibility are

achieved. It is clear that these structures produce negative properties without relying on the resonance since the negative properties appear in a broadband frequency range.

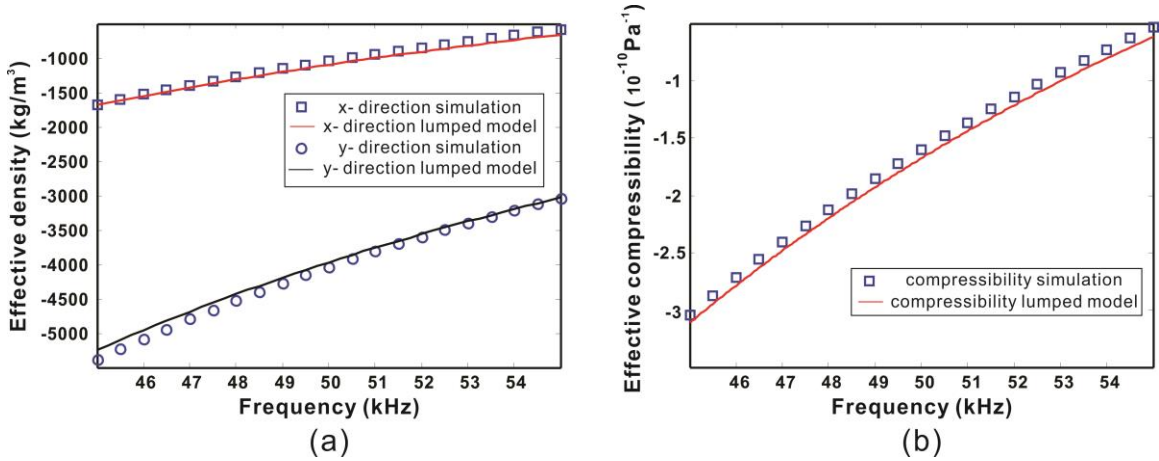


Figure 4.5 Effective densities and compressibility extracted from full-wave simulations and predicted by the lumped model. (a) Effective densities in  $x$ - and  $y$ -directions. (b) Effective compressibility.

### 4.2.3 Numerical Simulations

Two sets of full-wave simulations are then carried out to validate the proposed CMM. The acoustic-shell interaction model is used for numerical simulations. Specifically, we use the interior shell feature to model the plates. The entire CMM slab consists of  $120 \times 10$  unit cells: there 120 units in the  $x$ -direction and 10 units in the  $y$ -direction. Perfectly matched layers (PML) are used to minimize reflections from the boundary. The thickness of the aberrating layer is 40 mm. The density and sound speed of the background medium (water) and the aberrating layer are  $1000 \text{ kg/m}^3$ ,  $1500 \text{ m/s}$  and  $2000 \text{ kg/m}^3$ ,  $2500 \text{ m/s}$ , respectively. The properties of the aberrating layer are chosen so that it mimics human skulls. The acoustic impedance of the aberrating layer is therefore over 3.3 times larger

than the background medium, providing a sufficient amount of mismatch. Figure 4.5 shows that at 50 kHz, the density and compressibility of CMM satisfy Eqs. (4.7) and (4.8) for the given values: the density is  $-1000 \text{ kg/m}^3$  and  $-4000 \text{ kg/m}^3$  in the x- and y-directions, respectively; the compressibility is  $-1.6 \times 10^{-10}$ .

In the two examples, a curved (focused) array and a linear array are respectively introduced to generate different acoustic fields. In the first case, the curved array is placed in front of the aberrating layer (the CMM is on the same side as the array), whereas in the second case, the CMM is on the opposite side of the layer. The curved array is treated as an active acoustic source. Since the CMM would effectively cancel out the aberrating layer, the focal point will be 60 mm (total thickness of the CMM and the aberrating layer) behind the original one. The curved array is therefore moved 60 mm away from the aberrating layer when the CMM is considered, so the focal point remains at the desired location. The position of the linear array is not moved, as it is treated as a passive source.

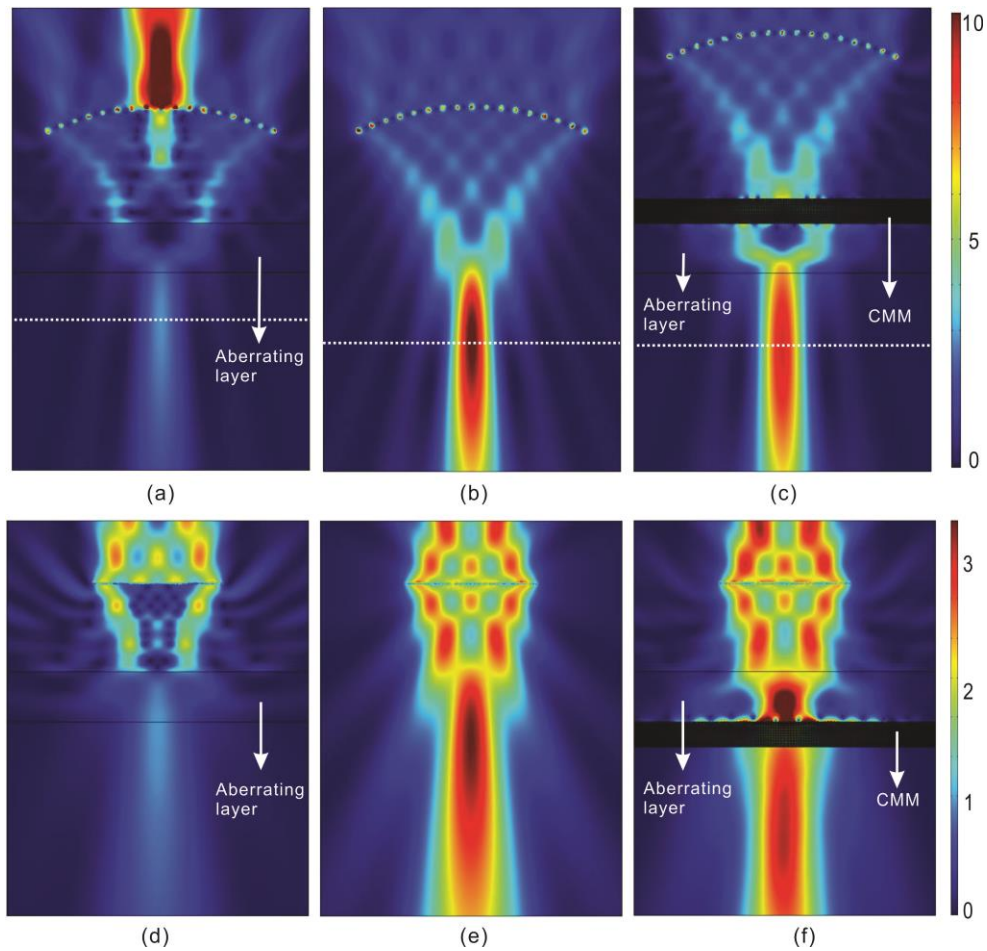


Figure 4.6 Acoustic intensity field for a curved array (focused beam). Three cases are presented: (a) the skull only, (b) homogeneous medium, and (c) with CMM and the skull. Acoustic intensity field for a linear array (unfocused beam). Three cases are presented: (d) skull only, (e) homogeneous medium, and (f) with CMM and the skull.

Figure 4.6 shows the acoustic intensity fields in three cases for each set of simulation: with the skull but without CMM, homogeneous water (control case), and with CMM and the skull, respectively. The CMM is placed in front of the aberrating layer, and white dotted lines indicate the position of the focal plane. When the CMM is used, the transmitted acoustic energy is significantly enhanced compared to the one without the

CMM, indicating that the reflected acoustic energy is considerably reduced and the aberrating layer is acoustically canceled out. It can be observed in Fig. 4.6(c) that the transmitted acoustic intensity field highly resembles that of the control case shown in Fig. 4.6(b), whereas in Fig. 4.6(f), the acoustic intensity field above the aberrating layer matches well with that of Fig. 4.6(e).

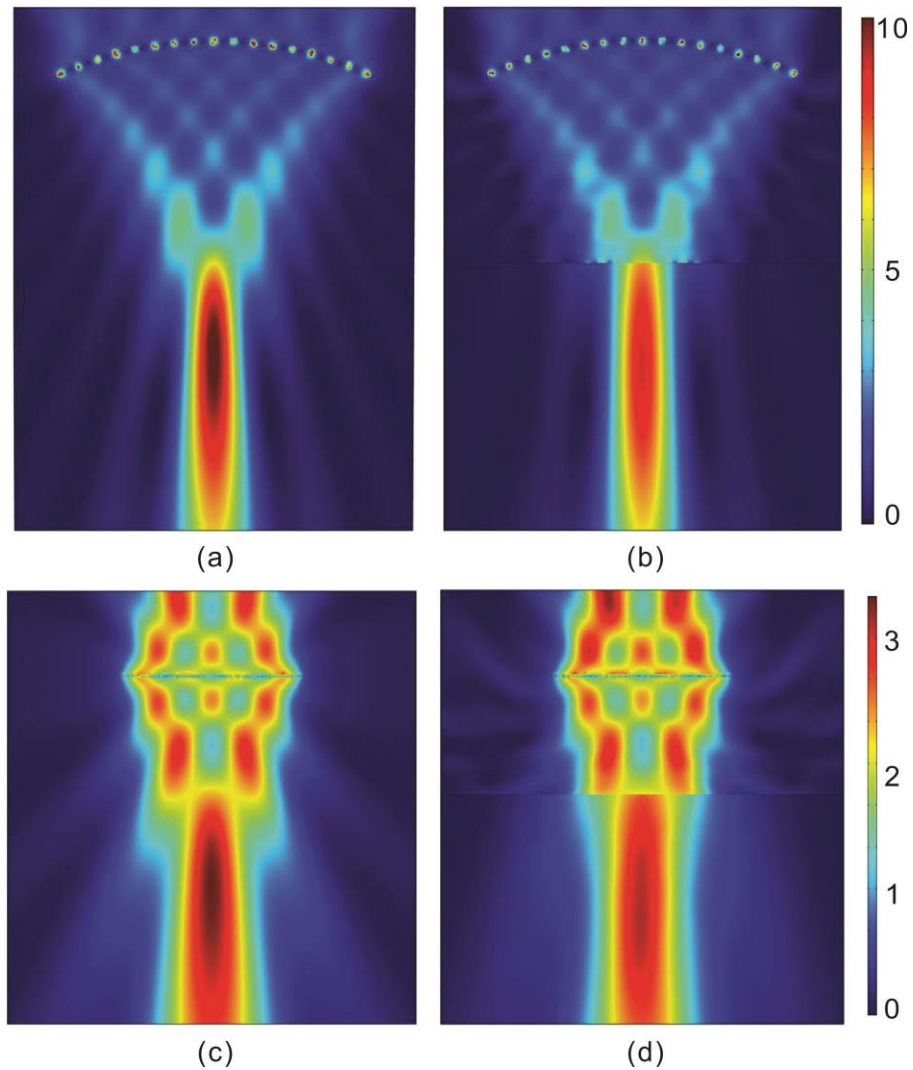


Figure 4.7 (a) Focused beam, homogeneous medium. (b) Focused beam. (c) Unfocused beam, homogeneous medium. (d) Unfocused beam.

Furthermore, as shown in Fig. 4.7, when the CMM and the skull are removed (edited out from Figs. 4.6(c) and 4.6(f)), the entire acoustic intensity fields look very similar to that of the control cases. In the curved array case, the CMM and the skull are removed from Fig. 4.6(c), and the area above the CMM is moved downwards to be directly in touch with the area below the aberrating layer. The intensity amplitude at the focal point is 88% of that of the control case. When CMM is not introduced, it is 28%. This is an over 300% improvement in term of the sound transmission. By varying the thickness of the aberrating layer, it is possible to have an even lower sound transmission (lower than 28%); therefore, a more significant improvement is possible using CMMs. The CMM also results in an accurate focus position, which is only 3 mm (1/10 of the wavelength) off the desired location, as in the control case. Without CMM, the focus is 14 mm (about 1/2 of the wavelength) off. This example demonstrates one potential application of CMMs to focus ultrasound behind aberrating layers, which could extremely useful for improving ultrasound imaging or therapy.

In the linear array case (unfocused acoustic field), the CMM and the skull are removed from Fig. 4.6(f), and the area above the aberrating layer is moved downwards to be directly in touch with the area below the CMM. The total acoustic intensity with the CMM behind the skull is 97% of that of the control case, whereas this parameter is 31% without the CMM. This example demonstrates another potential application of CMMs to detect passive acoustic source emissions or reflections from an object to be imaged or detected behind aberrating layers. Also very interestingly, this example indicates that the CMM can be placed behind a reflective layer and yet still achieve antireflection; thus, it has the advantage of being virtually concealed.

Typical antireflection layers rely on sound absorption or damping and must be placed in front of the reflective layer; therefore, they could be aesthetically unpleasant, particularly used for architectural acoustic applications. In both cases, the effective properties (density and compressibility) are extracted from the simulation results and are very close to the ones predicted by the earlier 1D model. Note that ideally a CMM would exactly restore the sound field without considering the energy loss inside the metamaterial. However, it would require an infinitely small unit cell so that homogenization is perfect. The material losses are not taken into account in the simulations. However, aluminum (plate material) is known to have a small loss factor, and the attenuation in water is also negligible. In addition, the side branch and plate-type metamaterial used here are nonresonant metamaterials; therefore, the material loss is not expected to be a significant factor. This is crucial for the application of interest in this chapter, as our CMMs do not suffer from the energy loss due to the resonance which would inevitably occur in practice. If the material losses are significant, the CMM can be designed so that its thickness is ultrathin in order to reduce the energy loss. Again, this is possible because the thickness of the CMM can be arbitrary in our design.

Numerical simulations are also conducted of CMMs for canceling out multiple aberrating layers and acoustic cloaking assuming homogenized effective media. For the layout shown in Fig.4.2 where two aberrating layers are canceled out, the density and compressibility of layer 3 and layer 4 are arbitrarily chosen to be 1.6, 0.8 and 2, 0.3, respectively. The CMM layers are placed in front of the aberrating layers. Figure 4.8 shows that for a curved array (focused beam) case, two CMM layers of effective parameters governed by Eqs. (4.10)(4.11)(4.12)(4.13), will effectively cancel out the

aberrating layers. The intensity fields in Fig. 4.8(b) and (c) indicate the validity of the multiple aberrating layers approach.

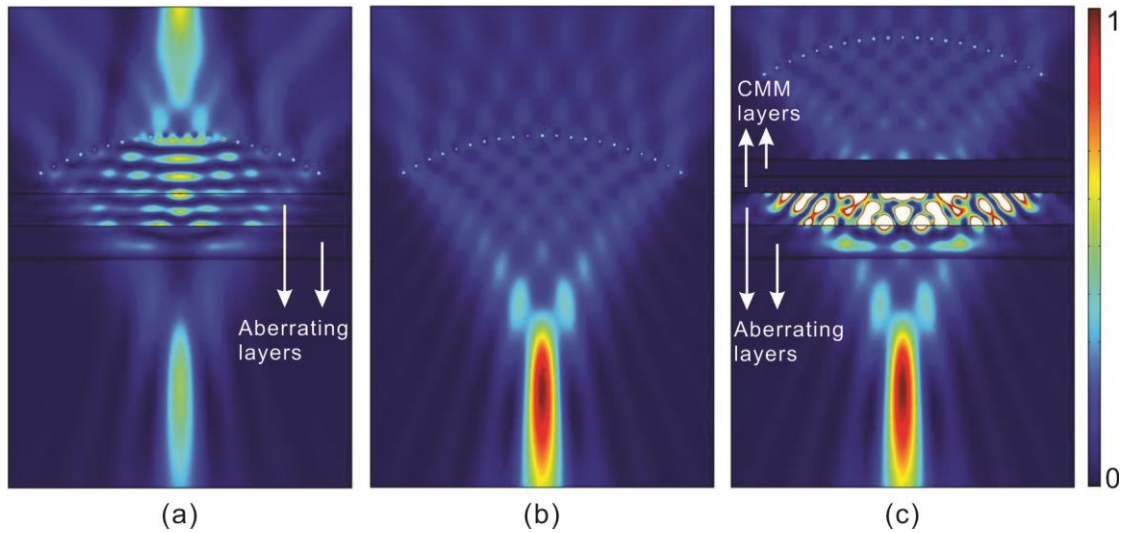


Figure 4.8 Acoustic intensity field of a curved array (focused beam). Three cases are presented: (a) Aberrating layers only. (b) Homogeneous medium. (c) With CMM and aberrating layers.

Numerical simulation results of the cloaking device are presented using effective media, where an acoustic cloaking device is placed on top of the slab so that it can effectively cloak the slab. The density and compressibility of the slab are randomly chosen to be 1.5, 0.1, respectively. The background medium has a density and compressibility of 1 and 1 (the units are arbitrary). The cloaking device consisting of the restoring layer and CMM layer is placed adjacent to the surface of the slab. Consequently, the slab is cloaked. Since the acoustic module in COMSOL does not include anisotropic properties, here we take the analogy between acoustic waves and TM polarized electromagnetic waves and use radio frequency module for simplification. The analogy is summarized as follows:

acoustic pressure to electric field, density in x- and y-directions to permeability in y- and x-directions, and compressibility to permittivity in z-direction.

Figure 4.9 depicts the acoustic pressure fields of a point source. The wave fields in Fig. 4.9(b) (control case) are almost identical in terms of amplitude and phase with those in Fig. 4.9(c), demonstrating the capability of the proposed cloaking device. The amplitude in Fig. 4.9(a) is much lower than these two as most of the energy is reflected due to the impedance mismatch between the slab and the background medium.

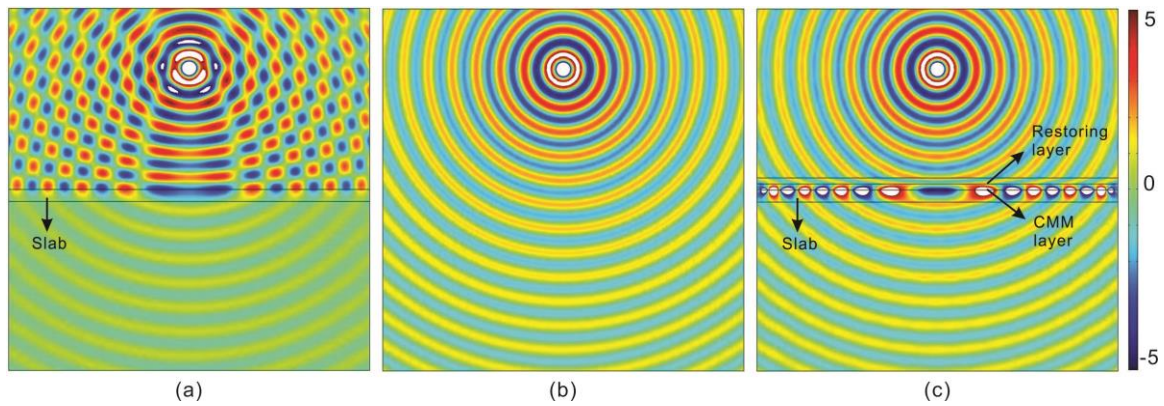


Figure 4.9 Acoustic pressure fields for a point source which is blocked by a slab. (a) Slab only. (b) Homogeneous medium. (c) With cloaking device adjacent to the slab.

To extend the current design to 3D, the branch openings can be replaced by slits, which also yield a negative compressibility or bulk modulus<sup>23</sup>. The major challenge in realizing the proposed CMM is that the thicknesses of the plates should be reasonably accurate, as they determine the effective density of the metamaterial. The boundaries of the plates should also be clamped as perfectly as possible. Finally, we note that, for a different piece of the skull, the acoustic properties (density and speed of sound) as well as the thickness could be different (variation around 10%-20%). This requires different effective density

and compressibility for the CMM according to the coordinate transformation shown in this chapter; otherwise, the CMM would not work effectively. Therefore, the same structure can be used, but the dimensions need to be modified (different plate sizes, branch opening heights, etc.) This is, in some way, a theoretical limitation of CMMs; i.e., the properties of the CMM depend on the property and dimensions of the object to be canceled out. Nevertheless, the proposed design can be readily modified to achieve active CMMs; i.e., a single CMM can be tuned for canceling out different aberrating layers. For example, the aluminum plates can be replaced by piezoelectric plates to actively tune the density<sup>69</sup>.

#### 4.3 Summary

In this chapter, we proposed the design of a CMM based on coordinate transformation of acoustic waves, which is able to cancel out an object in free space. Numerical examples are presented, in which CMMs are used to restore the acoustic fields distorted by aberrating layers. As demonstrated in this chapter, the CMM is capable of virtually removing an aberrating layer in a noninvasive manner; therefore, it could greatly facilitate nondestructive evaluation, transcranial ultrasound imaging and treatment. The proposed CMMs can be readily used to cancel out multiple layers or achieve acoustic cloaking if needed. CMMs are also expected to be useful for the design of acoustic cloaking and all-angle antireflection materials<sup>70</sup>. The design methodologies of the CMM can be used in other applications where effective density and/or compressibility need to be tuned for optimal performance. It is expected that the structure and concept proposed here pave the way for various acoustic applications.

## Chapter 5 Acoustic Metasurfaces with Asymmetric Transmission

Asymmetric transmission is a kind of interesting phenomenon, in which an incident wave is prevented from one direction, and is allowed from another. This unique feature adds a great amount of flexibility to wave manipulation. In physics, one-way manipulation was first studied based on electromagnetic waves<sup>71</sup> and heat flux<sup>72</sup>. Following these concepts, several design strategies have been proposed to realize asymmetric transmission, in both linear<sup>73</sup> and nonlinear systems<sup>74</sup>. Nonreciprocal systems utilize nonlinearity or active control of acoustic waves to break the reciprocity. Although the transmission contrast can be relatively high, these systems generally suffer from low efficiency and high energy consumption. The design complexity may also make them impractical for real world applications. On the other hand, reciprocal and symmetric systems could be potentially easier to design, as they are mostly passive and do not change the frequency content of the sound as it does in nonlinear systems. The drawbacks of these systems are that they are commonly associated with bulky structures and complicated boundary geometries.

As have been introduced in chapter 1, the emergence acoustic metasurfaces opens up new possibilities in manipulating acoustic waves by controlling the refraction/reflection behaviors. The flat geometry and thin thickness also allows it for better integration into different dimensions. Recently, an acoustic open tunnel with metasurfaces attached on the wall was proposed to allow sound transmission only in one direction<sup>75</sup>. Although asymmetric transmission is realized based on the phase engineering through the channel wall, the scheme requires the presence of a tunnel and its cross-sectional dimension to be comparable to the working wavelength, which poses limitations to its applications. One-

way acoustic metasurface with flat geometry and ability of integration is thus highly desirable in the acoustic community.

In this chapter, we combine the concept of asymmetric transmission and acoustic metasurfaces, a flat and thin metasurface is investigated which yields asymmetric transmission within a certain frequency band.

### 5.1 Gradient-index Metasurface and Near-zero Index Metasurface

To design the acoustic metasurfaces with asymmetric transmission, two different types of metasurfaces are adopted. The first type is the gradient-index metasurface (GIM), and the second type is the near-zero index metasurface (ZIM). To this end, the unique properties of these two types of metasurfaces will be first introduced, then the working principle of the device will be studied.

In 2011, it was found that for waves transmitting from one medium to another where there is a phase discontinuity along the interface, the refracted/reflected beam will be dictated by the generalized Snell's law<sup>76</sup>. For example, consider a plane wave impinging normally on the GIM, the transmitted wave will travel at an angle given by:

$$(\sin \theta_t - \sin \theta_i)k_0 = d\Phi / dx \quad (5.1)$$

where  $\theta_t$  and  $\theta_i$  are transmitted and incident angles,  $k_0$  is the wave number,  $d\Phi / dx$  is the phase gradient along the surface. For normal incidence, the refracted angle  $\theta_t$  will have a certain non-zero value as  $\theta_i$  is equal to zero.

Figure 5.1 shows the pressure field of an incoming wave propagating normally to a ZIM at 3 kHz. The unit cells have a width 26 mm and depth 60 mm. Along the direction parallel to the interface, six units form a period that cover a phase change of  $2\pi$ . In other

words, the difference of phase change across adjacent unit cells is  $\pi/3$ . The phase gradient along the surface of the GIM is  $d\Phi/dx=40.3$  rad/m. It can be clearly seen that the outgoing beam is bended and has a certain refracted angle, which can be calculated according to Eq. (5.1).

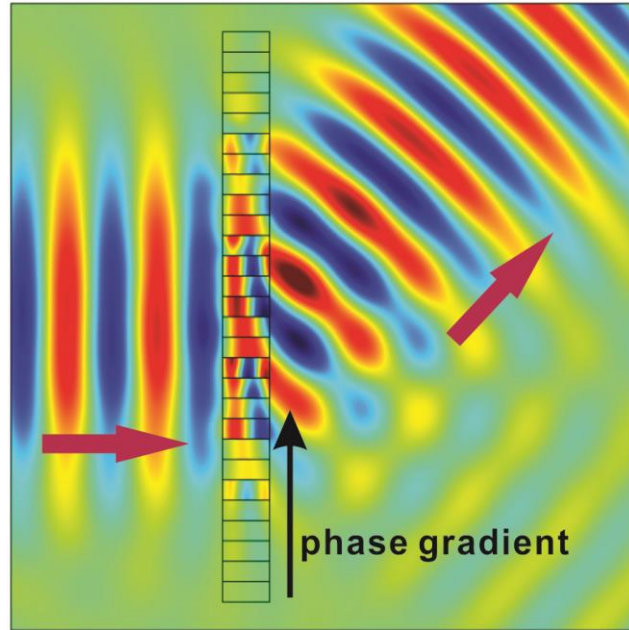


Figure 5.1 Acoustic pressure field of an incoming wave transmitting through a GIM.

The ZIM is an acoustic metasurface whose effective refractive index is near zero. For normal transmission, the transmitted wave undergoes little phase change, as the effective wavelength of the ZIM is approaching infinity. For incoming waves of oblique incidence, total reflection will take place. This is because the effective phase velocity of the ZIM is much greater than that of air, i.e.,  $v_{ZIM} \gg v_0$ , the critical angle is close to zero as  $\theta_c = \sin^{-1}(v_0/v_{ZIM})$ . This can be understood by the momentum mismatch at the interface when the incident angle is above the critical angle.

By combining these two types of metasurfaces, asymmetric transmission can be achieved, as illustrated in Fig. 5.2. When acoustic waves propagate normally to the GIM, they will be first bended, and total reflection will occur at the interface between ZIM and GIM. Consequently, the transmission coefficient in this direction is very low. On the other hand, for acoustic waves coming from the opposite direction, the incident wave reaches the ZIM at the normal direction and will pass through the ZIM with high transmission due to the tunneling effect<sup>30</sup>, as indicated by Fig. 5.2(c). Then the acoustic waves will pass through the GIM freely with a bended wavefront, as illustrated in Fig. 5.1.

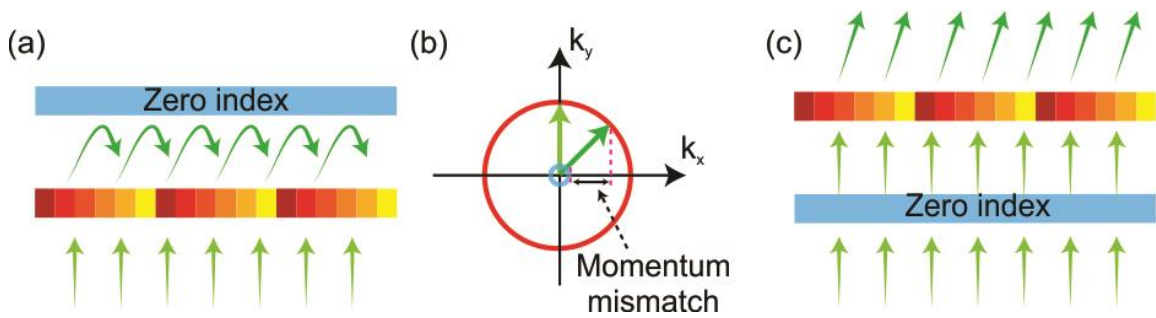


Figure 5.2 Schematic of the working principle of the device. (a) Low transmission case where the incident wave faces the GIM. (b) k-space diagram showing that the rotation of momentum vector causes its mismatch in transverse components, leading to the low transmission. (c) High transmission case where the incident wave faces the ZIM.

The unit cells in the ZIM can be designed specifically to yield a relatively high transmission coefficient. As a result, the overall transmission contrast is expected to be high in this case. Also, the transmitted wavefront will be redirected because of the phase gradient along the GIM surface. It is noted that for such a linear and reciprocal system,

the transmitted wave direction must have a certain change compared with the incident wave, dictated by the reciprocity in the system<sup>77</sup>.

## 5.2 Simulation and Measurement Results

To design the ZIM and the GIM, labyrinthine metamaterials are used<sup>30</sup>. It should be pointed out that the general strategy for realizing asymmetric transmission in this chapter is not restricted to the labyrinthine metamaterials, other candidates with the same required parameters can also be adopted, such as membrane-based structures<sup>78</sup>. For the ZIM, a type of labyrinthine structure is used which consists of subwavelength curled channels. Acoustic waves are assumed to travel freely inside the channels with small loss. The geometry of the unit cells is the same as that in an earlier study<sup>79</sup> and is depicted in Fig. 5.3(a). The labyrinthine unit has a width  $d_1 = 26$  mm, the thickness of the channels and the hard walls are 1.5 mm and 1 mm, respectively. The walls are 3D printed with acrylonitrile butadiene styrene (ABS) plastic with density  $1230 \text{ kg/m}^3$  and speed of sound  $2230 \text{ m/s}$ , and are assumed to be acoustically hard since their impedance is much greater than that of air.

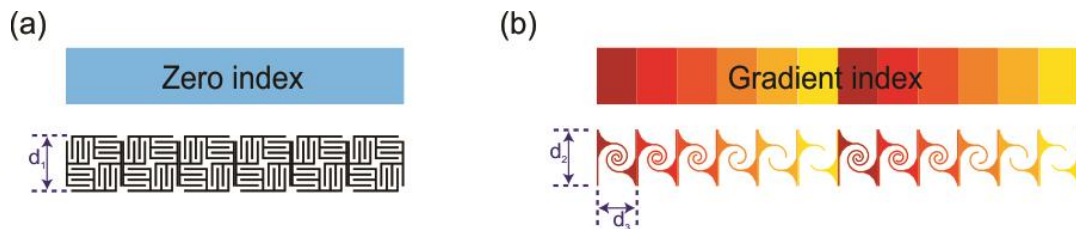


Figure 5.3 Geometry of the metasurfaces (a) ZIM. (b) GIM.

The spiral structures of the GIM are adopted from another previous study, which showed extraordinary capabilities in manipulating transmitted wavefronts<sup>80</sup>. Figure 5.3(b) shows the GIM, which consists of six types of individual unit cells. For the unit cells designed here, the transmitted phase difference across adjacent unit cells is about  $\pi/6$ , and two layers of the unit cells can cover a complete  $2\pi$  of phase change for one period (6 unit cells). The relative phase change across the unit cells can be preserved over a broad bandwidth around 3 kHz with a high transmission coefficient<sup>80</sup>. The proposed GIM is thus expected to have a wavefront-bending effect around 3 kHz. The unit cells have identical thickness  $d_2 = 34$  mm and width  $d_3 = 26$  mm, thus making the GIM planar and easy for integration with other structures.

To verify the performance of the proposed structures, simulations using finite element package COMSOL Multiphysics is carried out first. The effective refractive index of the ZIM is retrieved numerically using an inverse method<sup>27</sup> and the results are plotted in Fig. 5.4. The details of the method are presented in Appendix C. The background medium is air, with density and speed of sound  $1.2 \text{ kg/m}^3$  and  $343 \text{ m/s}$ , respectively. It can be seen that at the operating frequency (around 3.1 kHz), the refractive index of the proposed structure is close to zero. The ZIM is thus acoustically transparent for incoming waves with normal incidence and opaque for oblique incident angles. To ensure sufficient energy contrast, two layers of the ZIM are used for the proposed device. The performance of the GIM can be found in Fig. 5.1 with an effective medium approximation.

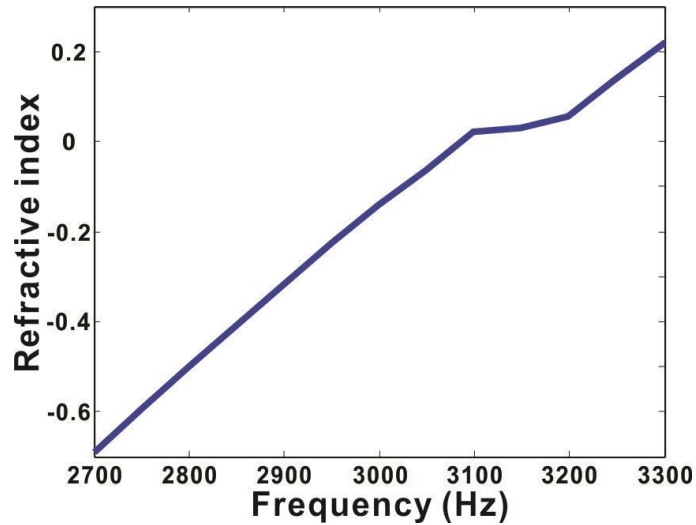


Figure 5.4 Retrieved refractive index of a ZIM unit cell.

Simulations for the whole device and measurements of the prototype are also performed. Perfect matched layers (PML) are used in the simulations to minimize reflections from the boundaries. The experimental setup is shown in Fig. 5.5, where a loudspeaker array sends Gaussian beams with a center frequency at 3 kHz towards the metasurfaces. The Gaussian beams have a bandwidth of 1 kHz and is therefore able to give sufficient frequency information within a broad frequency band. The metasurfaces are secured in a two-dimensional (2D) waveguide, with absorbing foams placed on both sides to prevent acoustic waves bypassing them. The field behind the metasurfaces is scanned with a moving microphone with a step size 2 cm. The signals are averaged with five measurements. The acoustic pressure field at different frequencies is then obtained by the inverse Fourier transform. Two sets of simulations and measurements are performed by swapping the direction of the incoming wave.

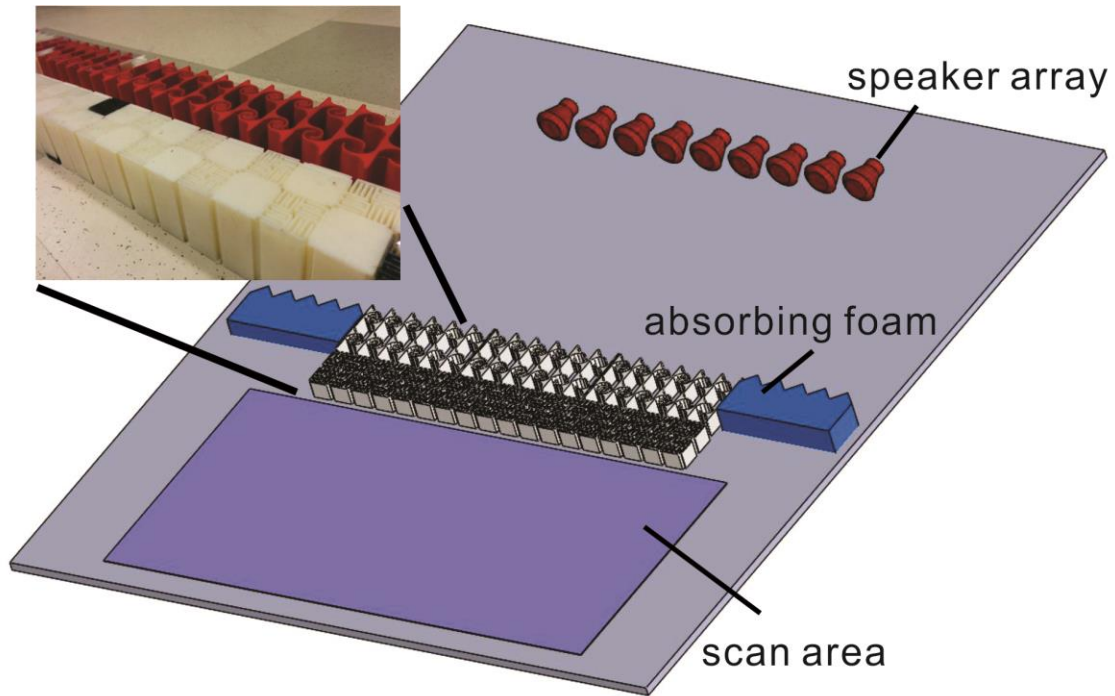
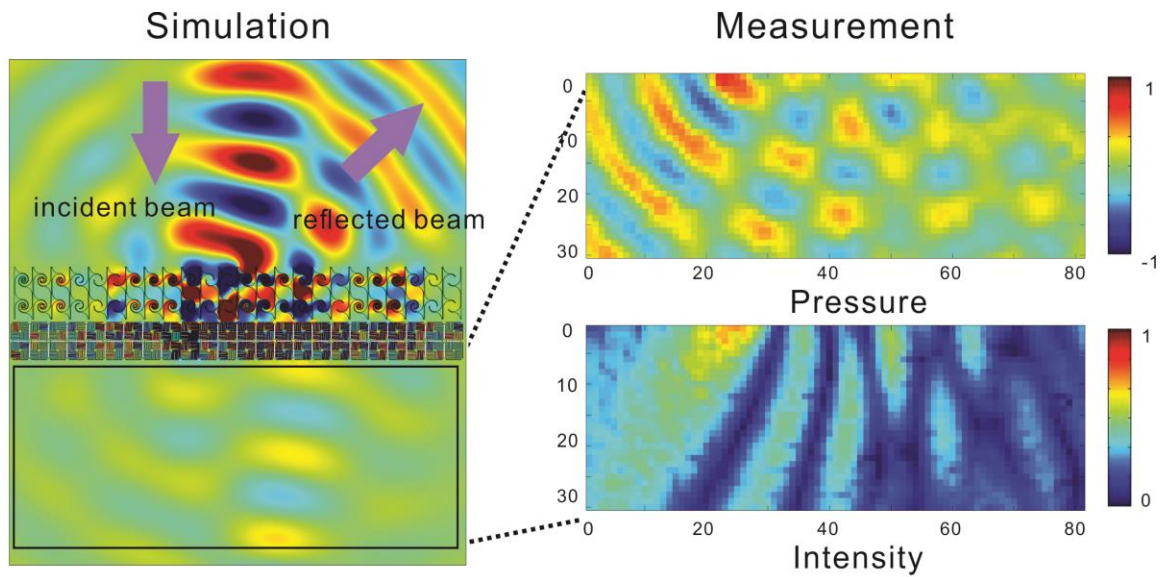
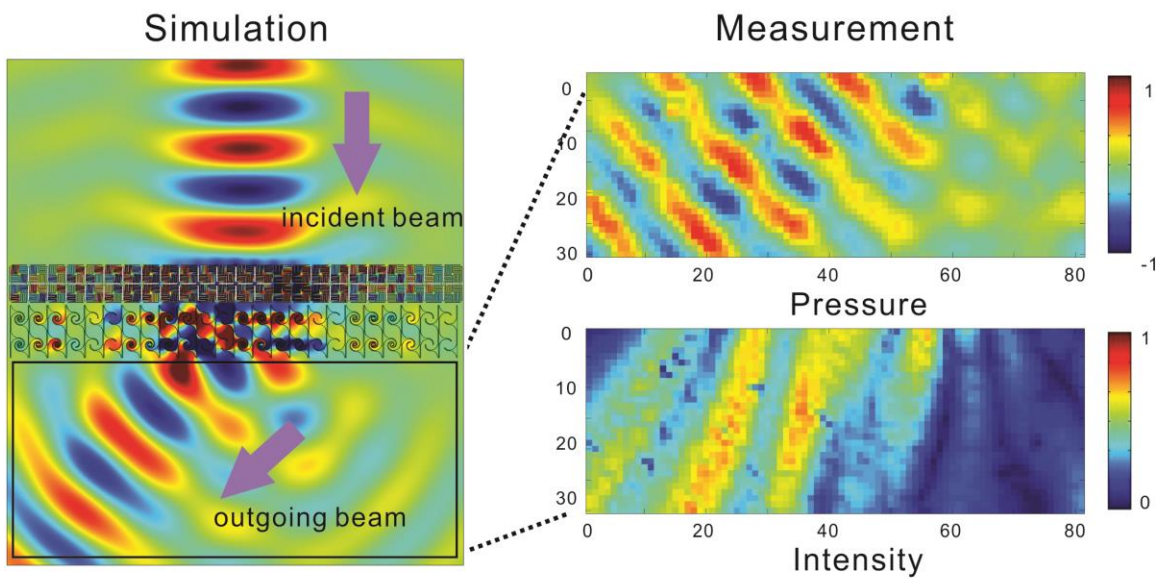


Figure 5.5 Simulation and experimental setup. Inset shows the photo of the fabricated sample.

The fabricated device is shown in the inset of Fig. 4, where the red structure on the top is GIM and the white structure on the bottom is ZIM. The overall size of the device is  $63\text{ cm} \times 12\text{ cm}$  and the thickness is about one wavelength at the operating frequency. The corresponding transmitted angle in the high transmission case is calculated as  $45.2^\circ$  according to Eq.(5.1), assuming the incident angle is  $0^\circ$ . The acoustic fields in the scan area for simulation and measurement are illustrated in Fig. 5.6 at  $3.1\text{ kHz}$ . The acoustic intensity field is calculated by taking the absolute square of the pressure field. Reasonably good agreement can be observed. The results indicate that the proposed device can yield an asymmetric transmission phenomenon for incident waves from different directions. The measured transmitted wavefront for the high transmission case is around  $46^\circ$ , which matches well with theory.



(a)



(b)

Figure 5.6 Simulated and measured acoustic fields at 3.1 kHz for incident waves in different directions. Axis unit: cm. (a) Incident beam is facing the GIM, corresponds to low transmission case. (b) Incident beam is facing the ZIM, corresponds to high transmission case.

Next, we investigate the overall transmitted energy for both cases. The total acoustic energy along a transverse line behind the sample is integrated. The line is 10 cm away from the sample to avoid capture of surface waves. The overall normalized transmission is shown in Fig. 5.7 within the frequency band 2.6 kHz to 3.6 kHz. The peak energy contrast is about four times in measurement, which is smaller than simulation (over ten times), and the optimal working frequency also has a certain shift from 3.1 kHz to 3.28 kHz. Several possible factors could contribute to these deviations between simulation and measurement. Firstly, the simulation assumes no internal loss within the metasurfaces, however, viscous loss within small channels is inevitable in practice<sup>81</sup>, which may decrease the energy contrast in measurements. The leakage inside the metasurfaces and the imperfect boundary conditions can also affect the experimental results. The operating frequency may have shifted due to imperfection and nonuniformity of the fabricated samples.

To minimize the effect of loss in the proposed scheme, the labyrinthine structures may be replaced by low-loss membrane-type acoustic metamaterials<sup>78</sup>, or metascreen passive phased arrays<sup>82</sup>. It is also expected that more ZIM layers can be employed to yield larger energy contrast.

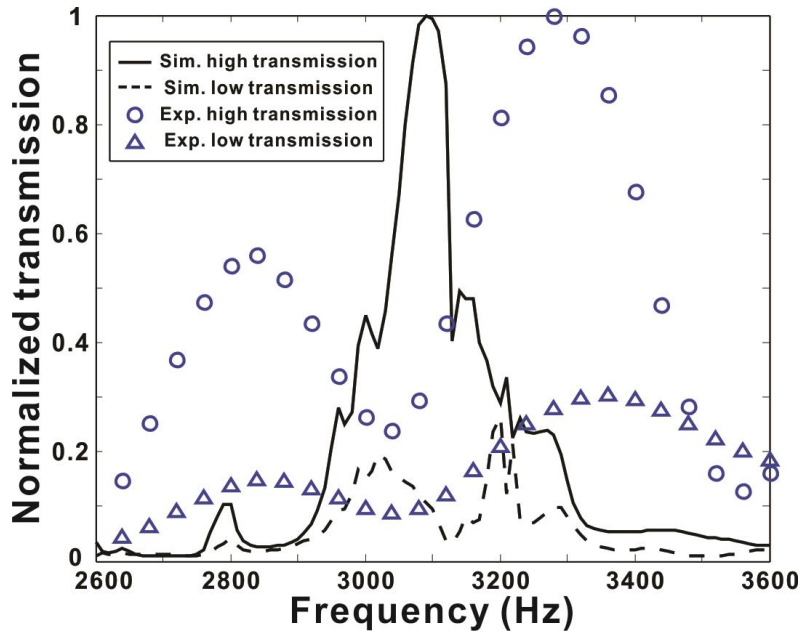


Figure 5.7 Normalized transmission for different directions of incoming waves.

Furthermore, we investigate the performance of the proposed device as a function of incident angle. As discussed earlier in this chapter, the device is assumed to have optimal performance for normal incidence. Here, numerical simulations are carried out at 3.1 kHz, the normalized transmission is shown in Fig. 5.8 at different incident angles. As expected, the transmission is at its highest value at  $0^\circ$  for the high transmission case and decreases quickly at larger incident angles. For the low transmission case, the transmission is always low. The device appears to have acceptable performance when the incident angle is less than around  $10^\circ$ .

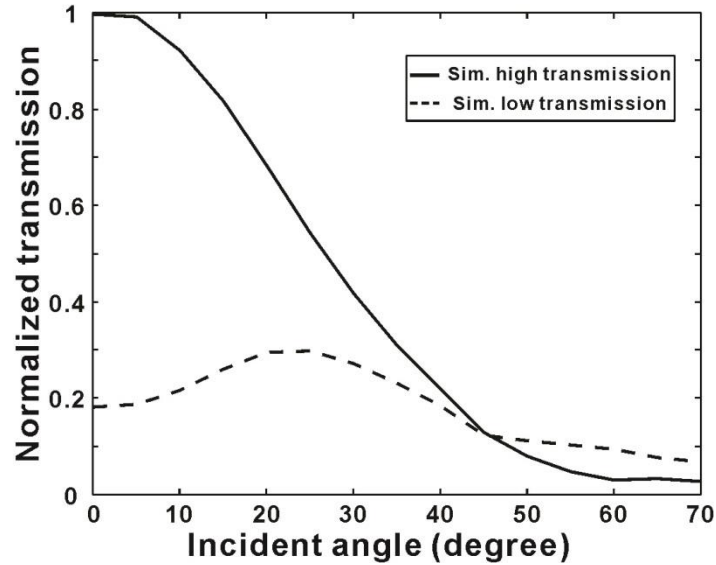


Figure 5.8 Normalized intensity transmission as a function of the incident angle.

### 5.3 Summary

In this chapter, we have designed, fabricated, and experimentally characterized a thin acoustic metasurface which exhibits asymmetric transmission at around 3.1 kHz. The effect is realized by total reflection for oblique incidence and tunneling for normal incidence induced by the ZIM. The device has a flat geometry and can be also readily modified to achieve asymmetric transmission for 3D wave propagation. It is worthy pointing out that due to the dispersive nature of the ZIM structure, the near-zero refractive index occurs only within a relatively narrow frequency band, as seen in Fig. 5.4. The operating bandwidth of the proposed device is thus mainly limited by the performance of the ZIM. For the GIM, its performance can be preserved within a certain frequency band, which is wider than the ZIM. Moreover, the device works best for normal incidences, as for oblique incidences, when the incident wave is facing the ZIM, the transmission will be relatively low. On the other hand, for incident waves from the

opposite direction, total reflection may not occur at the interface of the metasurfaces. This is because the transmitted angle across may be small for some certain incident angles. Within some certain range of incident angles, the transmitted wave may be surface wave which travels along the surface of the GIM, or having evanescent components and decay quickly<sup>80</sup>, and neither of these cases will excite high transmission through the ZIM. The proposed device thus has a limited region for incident angles to ensure both the high transmission and low transmission requirements.

Despite the drawbacks discussed above, the proposed device can still be helpful in noise control and architectural acoustics by rejecting the unwanted acoustic waves. The design may find applications in acoustic sensing and therapeutic ultrasound as well. The design strategy which involves a wave vector dependent manner also suggests new ways of controlling acoustic waves.

## Chapter 6 Acoustic Hologram Based on Metasurfaces

The ability to manipulate acoustic waves via metasurfaces has been demonstrated by controlling the refractive/reflective behaviors of the incident waves. In the previous chapter, the potential of asymmetric transmission is studied both numerically and experimentally, some other possibilities, like self-accelerating beams<sup>83</sup>, has also been proposed using metasurfaces. In this chapter, we push the capability of acoustic metasurfaces one step further, and demonstrate its unprecedented possibility of manipulating acoustic waves, that is, holographic reconstruction.

Holography is a technique of reconstructing the entire wave field information. In optics, holography has found a lot of useful applications, such as virtual reality devices, data storage and optical communications<sup>84</sup>. In acoustic realm, the theory has also been demonstrated for over 30 years<sup>85</sup>, but its applications are less developed compared with optical ones. One major reason is that to generate a meaningful acoustic image, it often requires a lot of active acoustic transducers and electric networks. This is also partly true for optic holography, and the large power consumption and difficulty in element design have posed limitations to the development of holography.

Recently, using metasurfaces as holograms has opened up a new approach for designing holograms<sup>86</sup>. The relatively easy fabrication processes and the passive nature of metamaterials offer great versatility on shrinking the sophisticated systems. The capability of full control of waves also provides solid foundation in developing metamaterial-based holograms. Till now, several optic holograms have been proposed using metamaterials<sup>87,88</sup>, acoustic holograms, on the other hand, are analogues to these

concepts in terms of wave manipulating techniques. In this chapter, we demonstrate an acoustic metasurface hologram that can be used for holographic reconstruction.

## 6.1 Weighted Gerchberg-Saxton Algorithm

It has been shown in chapter 5 that acoustic metasurfaces can be utilized to control the transmission/reflection characters of acoustic waves. To avoid cumbersome circuitry and active acoustic elements, metasurfaces with high transmission coefficients are used to generate acoustic images. Since we are trying to maintain a high efficiency in terms of energy, the metasurface elements are designed to yield a relatively high transmission coefficient at the operating frequency (4 kHz). To simplify the design, the amplitude of each element is considered to be uniform since we are more concerned with the manipulation of transmitted phases. We hereby introduce the Weighted Gerchberg-Saxton (GSW) algorithm<sup>89</sup>, which was first used in optics and is free of amplitude manipulation, for the calculation of phase patterns for the acoustic metasurface hologram. The algorithm is modified and combined with the MATLAB simulation tool, Field II, to perform optimization of the hologram parameters.

Consider a hologram that consists of acoustic sources with  $N$  elements, and the acoustic image plane is decomposed into  $M$  targets, each contains a small area. The sound pressure at the  $m$ th target is the sum of all the acoustic waves from each source element:

$$p_m = i \frac{\rho c k S}{2\pi} \sum_{n=1}^N d_{mn}^{-1} |u_n| \exp(i\varphi_n) \exp(-ikd_{mn}) \quad (6.1)$$

where  $\rho$  and  $c$  are background medium density and speed of sound,  $k$  is the wave number,  $S$  is the surface area of each element,  $d_{mn}$  is the distance between the  $n$ th

element and  $m$ th target,  $u_n$  and  $\varphi_n$  are the amplitude and phase of the radiating velocity on the source surface, respectively. The distance  $d_{mn}$  is given by:

$$d_{mn} = \sqrt{(x_m - x_n)^2 + (y_m - y_n)^2 + z^2} \quad (6.2)$$

where  $(x_m, y_m)$  and  $(x_n, y_n)$  are the local coordinates of the target and source, respectively,  $z$  is the distance from the source plane to the image plane.

We hereby write Eq. (6.1) in matrix notation, and apply Green's function for the calculation of the source element parameters. The pressure vectors  $\mathbf{p}$  on each target element and  $\mathbf{u}$  on each source element can be associated by the transferring matrix  $\mathbf{H}$ :

$$\mathbf{p} = \mathbf{H}\mathbf{u} \quad (6.3)$$

Here  $\mathbf{p}$  and  $\mathbf{u}$  are  $M \times 1$  and  $N \times 1$  pressure vectors including the amplitude and phase information. The  $(m, n)$ th component of matrix  $\mathbf{H}$  is given by:

$$\mathbf{H}(m, n) = iKd_{mn}^{-1} \exp(-ikd_{mn}) \quad (6.4)$$

and  $K = \rho ckS / 2\pi$  is considered to be constant since the source surface areas are identical.

We now introduce the GSW algorithm to optimize the phase for each source element, since its amplitude is assumed to be equal. The amplitude for each target element, i.e.,  $|p_m|$  is weighted by a factor  $w_m$  so that the amplitude deviations from the mean value will be reduced. By adding the weighting factor, the updated pressure vector and transferring matrix can also be written in the similar form with Eq. (6.3). The total absolute pressure value on the image plane is then expressed as:

$$\sum_m |\tilde{p}_m| = d_{mn}^{-1} \sum_m w_m \left| \sum_n \exp[i(\varphi_n - kd_{mn})] \right| \quad (6.5)$$

The iterative process is performed by calculating the weighting factor  $w_m$  for each iteration such that at 0th step  $w_m^0 = 1$ , and at  $t$  th step, we have:

$$w_m^t = w_m^{t-1} \frac{\langle |\tilde{p}^{t-1}| \rangle}{|\tilde{p}^{t-1}|} \quad (6.6)$$

By setting a convergence criteria, i.e.,  $\delta^t = \frac{\min\{|\tilde{p}_1|, |\tilde{p}_2|, \dots, |\tilde{p}_m|\}}{\max\{|\tilde{p}_1|, |\tilde{p}_2|, \dots, |\tilde{p}_m|\}} < \delta^{\text{stop}}$ , the pressure

distribution on the target can be regarded as uniform and the image quality is considered to be satisfactory. The optimized phase profile on the source plane can be found by:

$$\varphi_n = \arg \left\{ \sum_m w_m \exp(ikd_{mn}) \frac{\tilde{p}_m}{|\tilde{p}_m|} \right\} \quad (6.7)$$

In this manner, the deviation on the target is minimized, while the phase distribution on the source plane can be calculated.

## 6.2 Acoustic Hologram with Phase Modulation

We now use the GSW algorithm described above to design the acoustic metasurface hologram, Table 6.1 lists some of the design parameters for the proposed hologram.

Table 6-1 Design parameters of the acoustic hologram

$f$ (Hz)	$N$	$M$	$\rho$ (kg/m <sup>3</sup> )	$c$ (m/s)	$S$ (cm <sup>2</sup> )	$z$ (m)
4000	256 (16×16)	256 (16×16)	1.2	343	4 (2×2)	0.3

The metasurface is composed of 16×16 unit cells and is working by means of transmission. The amplitude is assumed to be equal, and the phase on each element can

be tailored within a  $2\pi$  range. The target is also broken down into  $16\times 16$  elements. The amplitude where has the image is assumed to be unity, and the amplitude where no image lies is considered to be zero. Certain convergence criteria are set to generate the phase profile of different images.

### 6.2.1 Characterization of the Unit Cells

Although the acoustic metasurface is theoretically able to modulate transmitted phase with arbitrary values, here we designed thirteen types of individual elements for the hologram. The phase difference of the transmitted phase for each adjacent element is  $\pi/12$ , and two layers of the elements can therefore cover the complete  $2\pi$  range of phase shift required by the hologram. Figure 6.1 shows the transmitted phase for each type of unit cell, note that in each case there are two identical unit cells for better illustration of phase change. The orientation of one of the two unit cells should also be inverted to seal a curled channel for acoustic waves. The geometry is similar with the previous ones, but is designed specifically here to have optimal performance at 4 kHz (the operating frequency). The unit cells are printed with ABS plastic, with volume  $2\text{ cm}\times 2\text{ cm}\times 2\text{ cm}$  ( $8\text{cm}^3$ ), density  $1130\text{ kg/m}^3$  and sound speed  $2230\text{ m/s}$ . The geometry of the fabricated unit cell is cubic so that it allows easy integration into arbitrary scales.

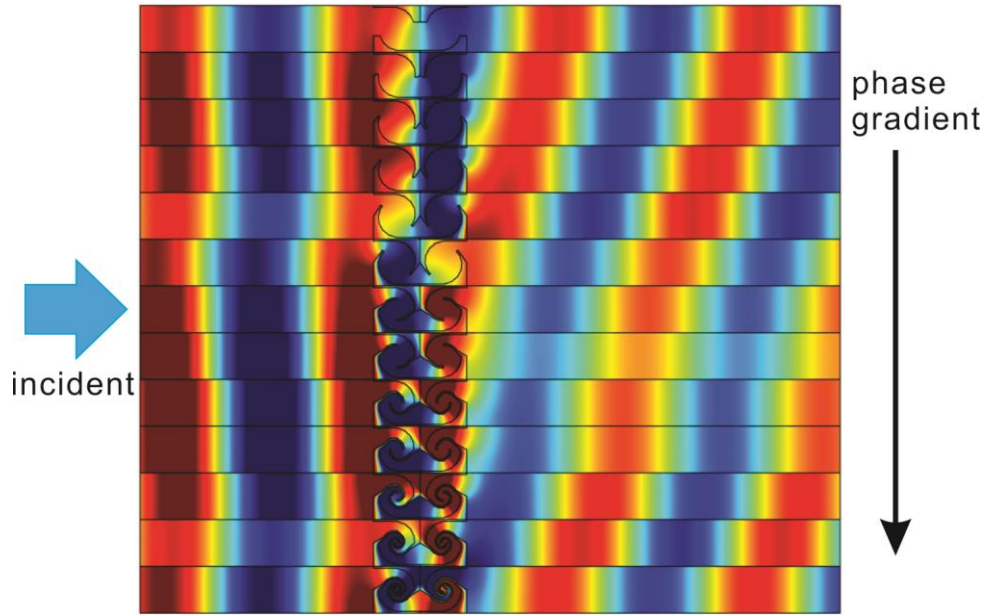


Figure 6.1 Transmitted phase for different types of unit cells.

From Fig. 6.1, it can be observed that there is a clear phase gradient along different types of unit cells, also for unit cell index 1 and 13 (lower index corresponds to less coiled structures), the transmitted phase has the same value. This is because the relative phase change for a single unit cell is  $\pi$ , and two of the unit cells will therefore have a phase difference of one cycle, making the transmitted phase identical. The complete  $2\pi$  phase difference is discretized into 24 combinations of unit cells, range from unit cell index 1+1 to unit cell index 12+13, with a step of  $\pi/12$ .

The transmitted amplitude for each type of unit cell is plotted in Fig. 6.2, each corresponds to two identical unit cells combined, as illustrated in Fig. 6.1, and is above 50% all cases. Viscous loss is not considered in the simulation. Although the transmission is not ideally uniform, and each combination maintains a different transmission coefficient, the overall transmission is high. We shall note here that for this specific configuration of the hologram, we are more concerned with the phase

information of the units, the amplitude is assumed to have a negligible effect on the performance, which will be confirmed later experimentally in this chapter.

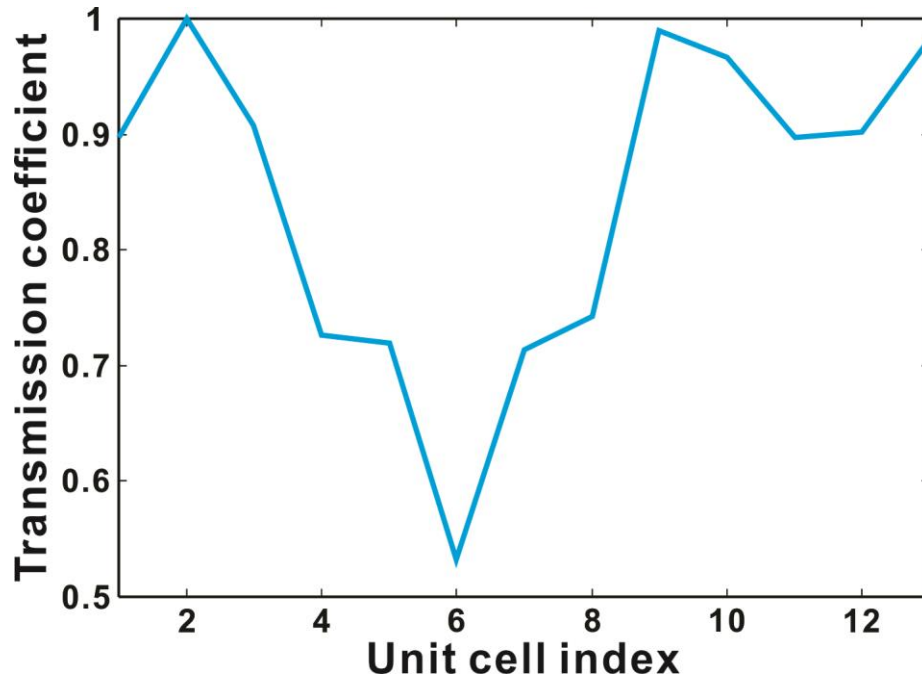


Figure 6.2 Transmission coefficient of different types of unit cells

### 6.2.2 Numerical Simulations

To validate the performance of the hologram, three different numerical methods are employed. The first one is the spatial impulse response-based field simulation tool Field II in MATLAB; the second one is the angular spectrum approach (ASA) for modeling the propagation of the wave field created by the hologram<sup>90</sup>; the third one is the commercial finite element software COMSOL Multiphysics. The Field II toolbox is directly associated with the GSW algorithm to generate the image, while ASA and finite element approach utilize the calculated phase from the algorithm, and perform wave propagation analysis for the pressure field on the image plane.

The image we select here is the capital letter “A”, the convergence in the GSW algorithm is set to be 0.6 to get the optimal phase delay on the source plane. The phase delay profile on the hologram is obtained by compensating the optimized phase delay on the source plane with the phase delay caused by the different distances from the point source. It should be pointed out that the compensation can be omitted if plane wave radiation condition is satisfied. However, since we are concerned with energy consumption and efficiency, a single point source is used here and the compensation process is necessary. The idea image, optimal phase on the source plane and the corresponding absolute acoustic pressure field is depicted in Fig. 6.3. As mentioned earlier, the hologram consists of  $16 \times 16$  units, so the hologram is  $32 \text{ cm} \times 32 \text{ cm}$ , sixteen units are arranged along the x- and y-directions on the source plane (assume image is projected along the z-axis), the relative phase delay in Fig. 6.3(c) shows the ideal phase right behind the hologram for the optimal image (Fig. 6.3(b)). The image size is  $64 \text{ cm} \times 64 \text{ cm}$ .

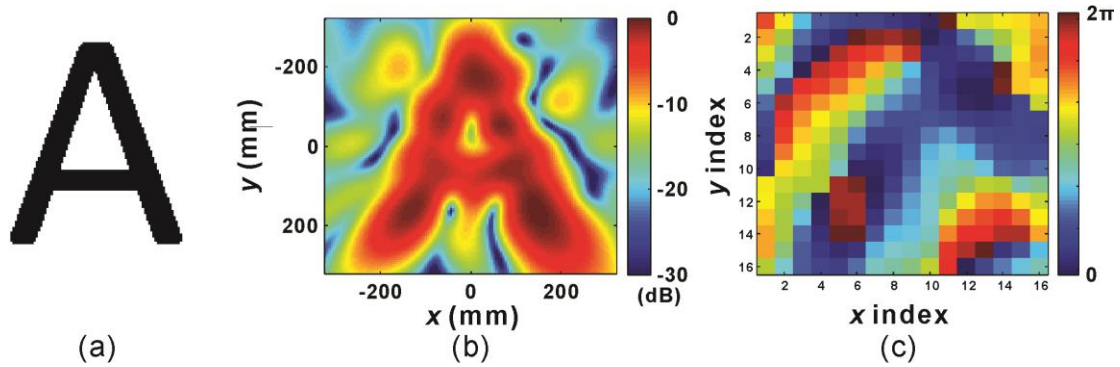


Figure 6.3 (a) Ideal image to be projected. (b) Calculated image using GSW algorithm. (c)

Ideal phase on the source plane.

Numerical results based on ASA and finite element analysis are now carried out for verification. For ASA, each element on the hologram is assumed to be a point source, which uniform amplitude, and different phases given by Fig. 6.3(c). The total acoustic field is much larger than the image size to mimic the free space situation. For finite element analysis in COMSOL, the simulation setup is illustrated in Fig. 6.4, where  $16 \times 16$  elements are placed in the source plane. PMLs are used on the boundaries to minimize reflections, the propagation depth is set to be 0.5 m, which is slightly larger than the focal depth to better illustrate the generation of the acoustic pressure field.

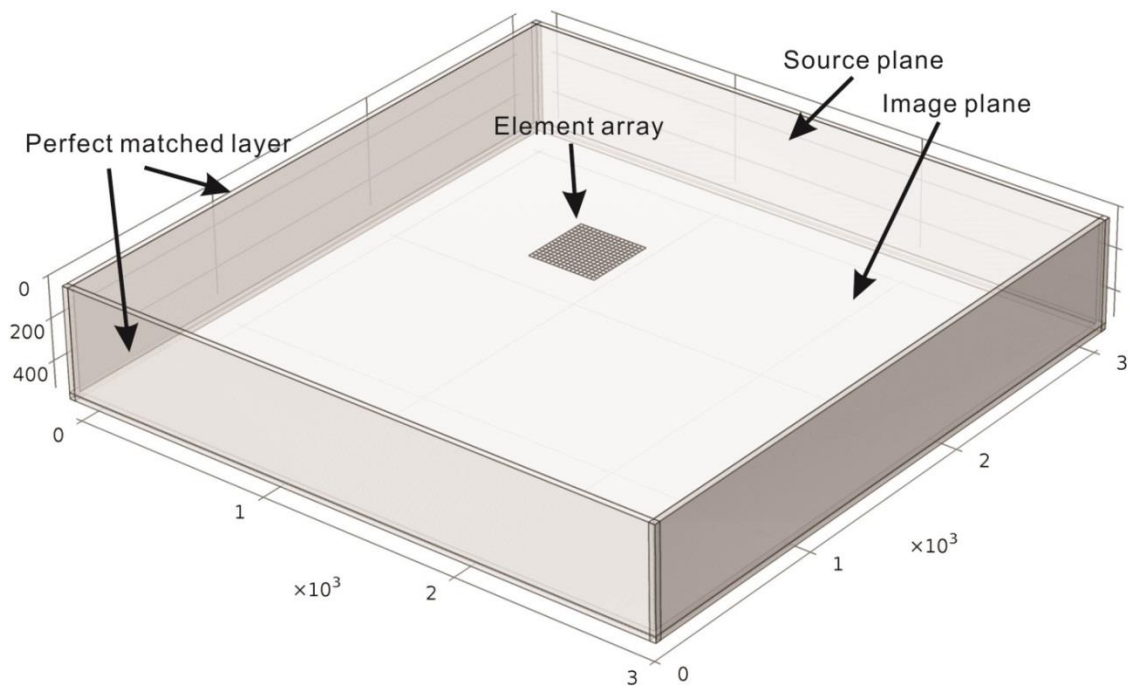


Figure 6.4 Simulation setup in COMSOL. Unit: mm.

The acoustic intensity fields from ASA and COMSOL are depicted in Fig. 6.5 and Fig. 6.6, respectively. Excellent agreements are observed, and both simulations clearly show

that with the phase modulation of each element, the radiated waves interact with each other and form an image of “A” at the designed focal depth.

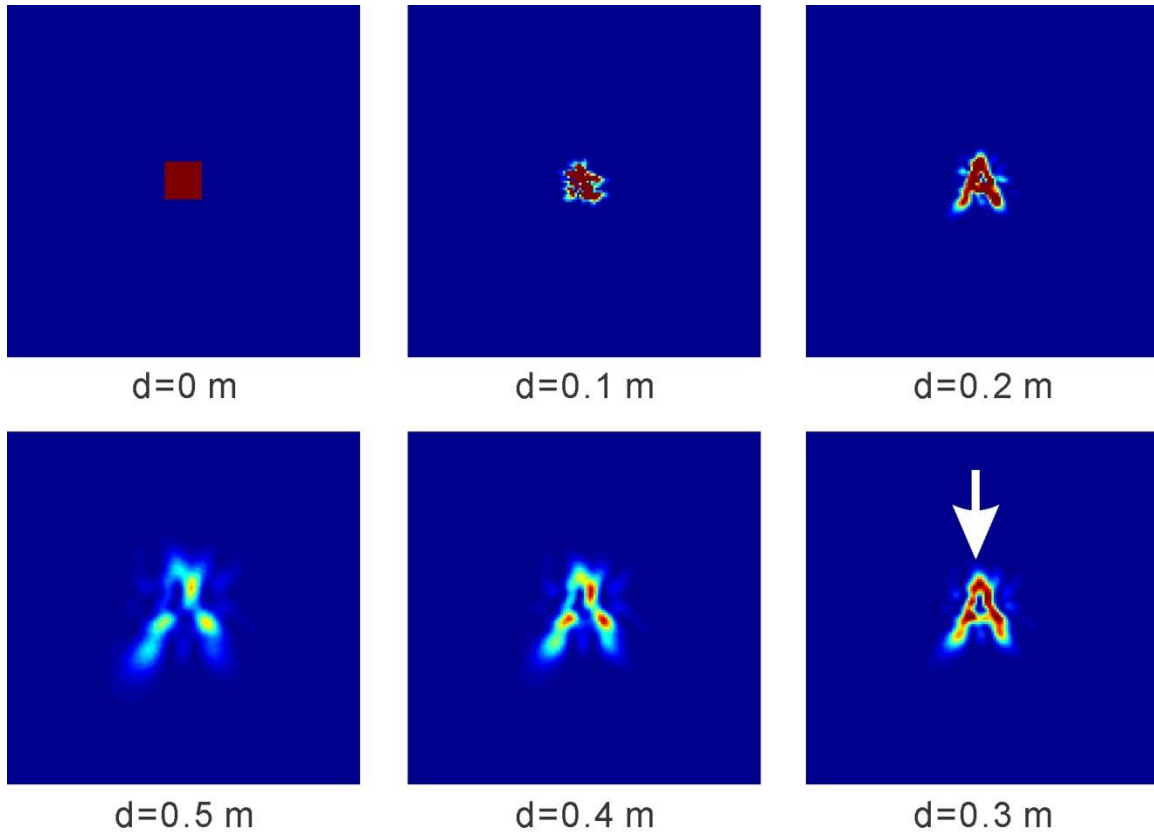


Figure 6.5 Generation of acoustic intensity fields at different focal depth from ASA.

White arrow denotes the ideal distance from the image plane.

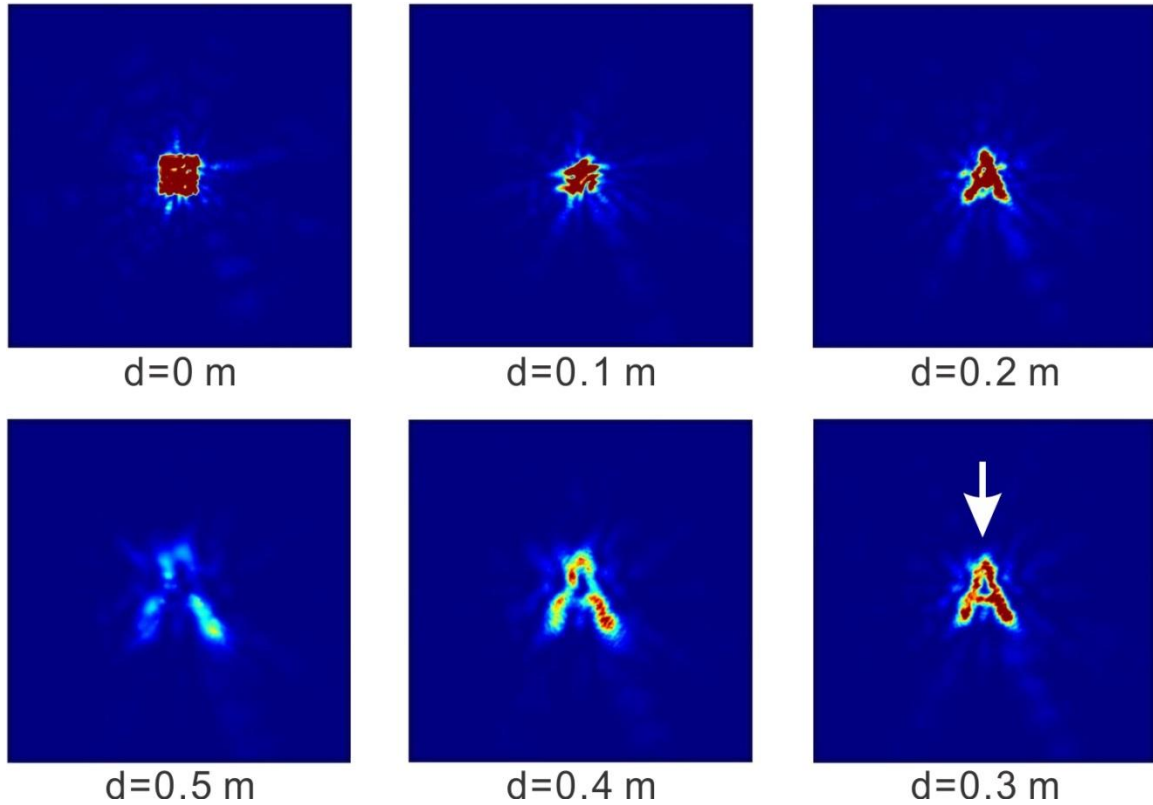


Figure 6.6 Generation of acoustic intensity fields at different focal depth from COMSOL.

White arrow denotes the ideal distance from the image plane.

### 6.2.3 Experimental Results

Experiments with the fabricated units are now carried out to further verify the proposed hologram. The unit cells are glued tightly to assure no leakage on the boundaries. A photo of the assembled hologram is shown in Fig. 6.7. The unit cells are 3D printed with randomly selected colors, so the color of the hologram does not reflect the types of the unit cells, nor the value of the phase change across each pixels.

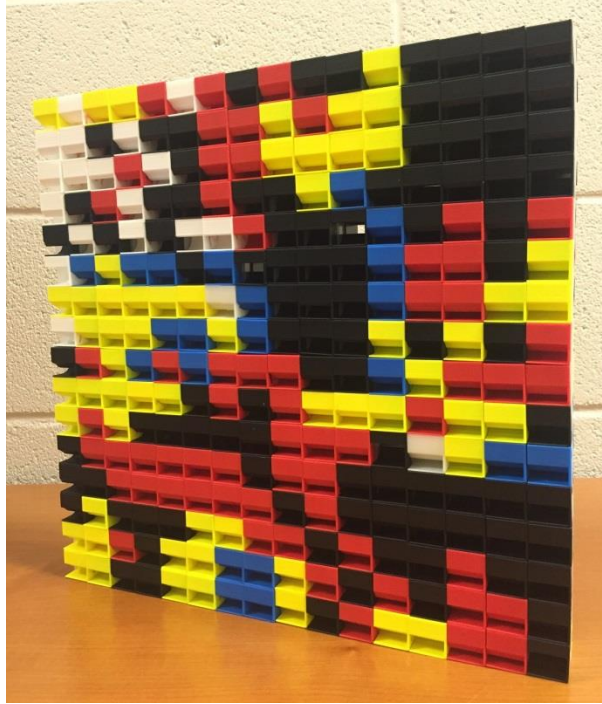


Figure 6.7 Photo of the assembled hologram.

The experiment setup is depicted in Fig. 6.8(a) and a photo of the measurement layout is shown in Fig. 6.8(b). The measurement is done in an anechoic chamber. A loudspeaker mimicking a point source is placed 0.5 m in front of the hologram, which is 0.3 m away from the image plane. The hologram is mounted securely inside a large hard paper panel. Since the acoustic impedance of the paper panel is much greater than air, it is assumed to be acoustically rigid and prevents acoustic field distortion caused by sound bypassing the hologram. The loudspeaker sends Gaussian pulses at a frequency of 4 kHz to the hologram, and the acoustic field is mapped by a moving microphone of step size 2 cm. The acoustic field at each point is measured out from five measurements to minimize noise. All the signals are referenced by a same signal to obtain both amplitude and phase information.

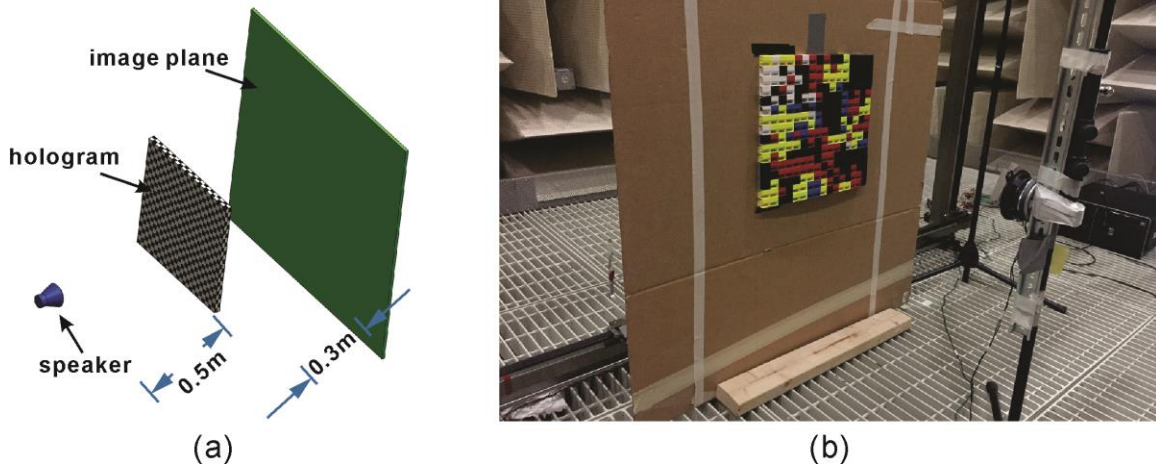


Figure 6.8 Experiment setup of the hologram measurement.

We first examine the measured phase right behind the hologram since the working mechanism of the hologram is based on phase modulation. The ideal and measured phase is depicted in Fig. 6.9. It can be seen that the general pattern is almost identical for the measured and designed phase, except some small discrepancies at some points. We note that although much effort has been done to eliminate the effect of noise, there is still some leakage on the hologram boundaries, and reflections from the scanning stage. Also, the response of the microphone is not perfect, especially when the pressure amplitude is small, and noise starts to come around. This is true for some of the pixels of the hologram, as although the transmission is assumed to be uniform, we did observe small deviations of the amplitudes across the hologram.

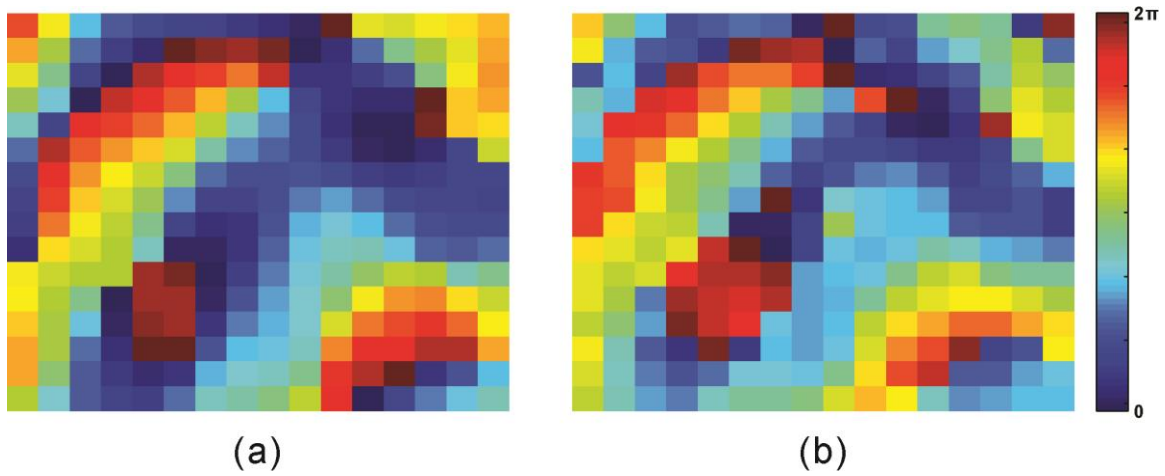


Figure 6.9 (a) Ideal and (b) Measured phase behind the hologram.

The generation of the acoustic image on each focal depth is shown in Fig. 6.10, varying from 5 cm to 30 cm. This can be compared with Fig. 6.5 and Fig. 6.6, again excellent agreement is observed. This confirms the validity of the proposed approach for designing the metasurface for holographic reconstruction.

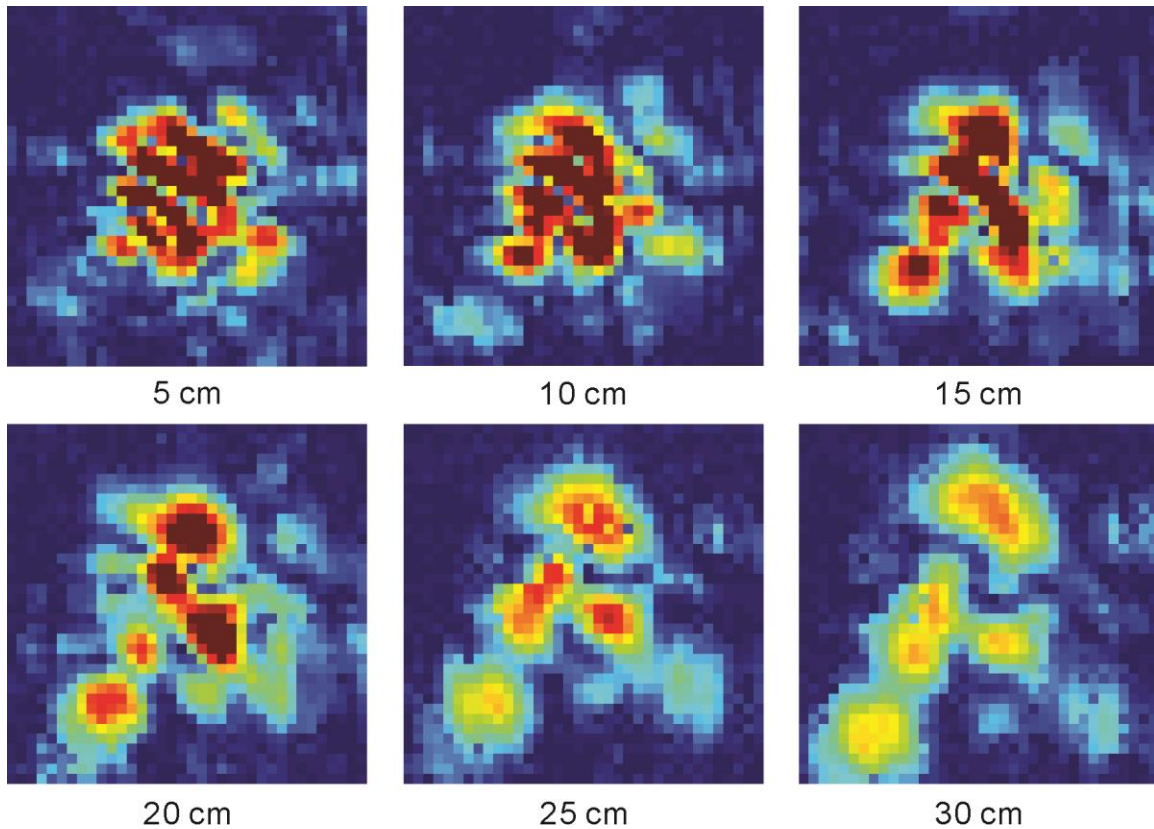


Figure 6.10 Generation of the acoustic pressure fields at different focal depth from measurements.

### 6.3 Multifocus Lens

The capabilities of the metasurface hologram are not restricted to holographic reconstructions. We now investigate the potential of the hologram as advanced acoustic lenses. Acoustic lensing techniques are highly desirable in the field of acoustics, and have brought about much research efforts. In practice, an advanced lens with complex focal patterns adds versatility in reshaping acoustic waves has great ability in acoustic energy deposition and imaging. Although metasurface-based single-focus acoustic lens has been demonstrated in 2D and 3D scenarios<sup>91,92</sup>, multi-focus lens with complex patterns using metasurfaces has rarely been demonstrated in literature.

Here we explore the potential of the hologram as a multi-focus lens. The general design procedure is the same with that of holographic reconstruction. The size of the multifocus lens is also 16 units on each axis ( $16 \times 16$ ). The designed focal spots, ideal and measured phase behind the lens are plotted in Fig. 6.11. The focal spots have different dimensions to demonstrate the complexity of the focal pattern.

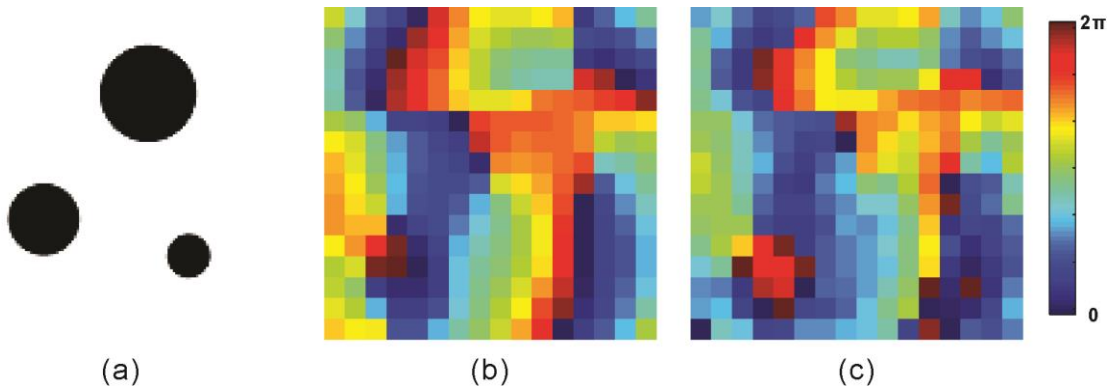


Figure 6.11 (a) Ideal focal pattern. (b) Ideal phase behind the multifocus lens. (c) Measured phase behind the multifocus lens.

Numerical simulations based on ASA are carried out in the same manner with the hologram; the results are shown in Fig. 6.12, with measurement results for comparison. Three focal spots of different sized can be observed at the designed focal depth. The good agreement between the two clearly demonstrates the capability of the metasurface hologram as advanced acoustic lens.

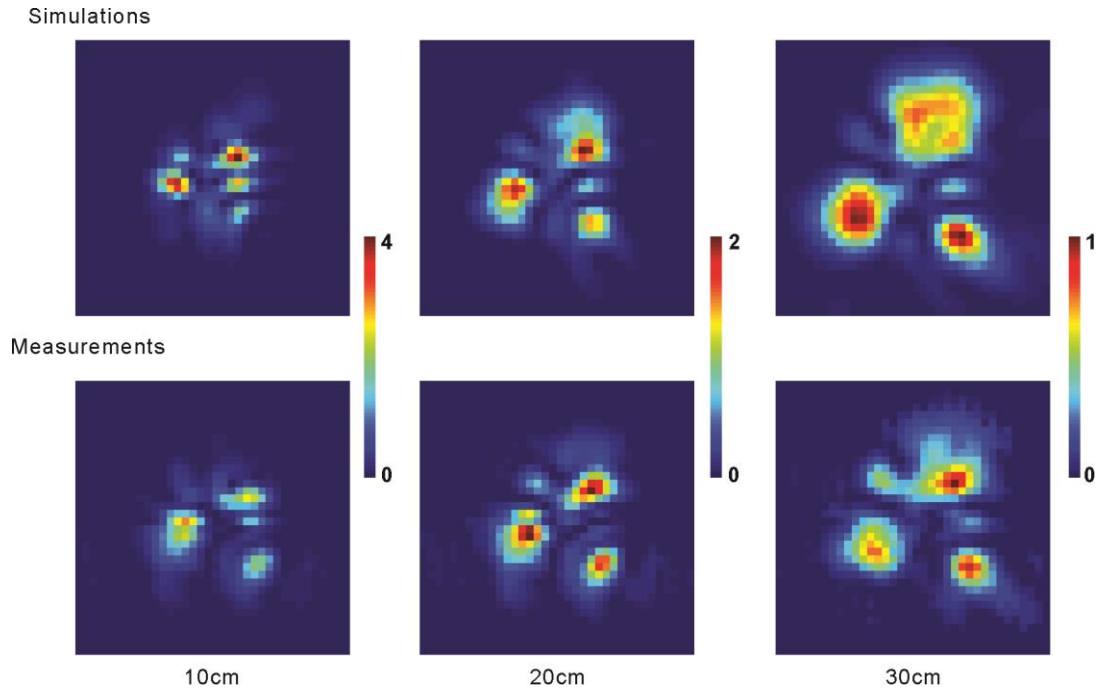


Figure 6.12 Simulation and measurement results of the acoustic intensity fields of the multifocus lens. Focal depth: left: 10 cm, middle: 20 cm, right: 30 cm.

#### 6.4 Summary

To conclude, we have designed, fabricated, and experimentally demonstrated an acoustic metasurface hologram. The capability of the hologram is verified by two different functionalities, the first is holographic reconstruction and the second is advanced acoustic lens. The experiment results match well with numerical simulations based on ASA and finite element analysis. The key feature of the proposed hologram is that it does not rely on active control of acoustic transducer elements and cumbersome circuits. It also does not require large energy input. The non-resonant nature of the unit cells also enables a certain bandwidth of the hologram. The hologram can in principle be scaled down to work at different frequency regions, such as ultrasound regime for applications in ultrasound imaging and therapy. It is hoped that the metasurface hologram can not only

be useful in audio reconstruction, but also in acoustic bottle beam generation<sup>93</sup>, acoustic levitation<sup>94</sup>, computational devices<sup>95</sup>, and so on.

## Chapter 7 Concluding Remarks and Future Work

### 7.1 Conclusions and Contributions

Acoustic metamaterials and metasurfaces offer a lot in achieving unprecedented possibilities in acoustics, in this dissertation, we focus on the design and application of these structures. A side-branch based acoustic metamaterial with broadband negative modulus is proposed, a lumped model is developed for the characterization of the structures, which agrees well with numerical simulations. For acoustic metamaterials with negative density, we designed a plate-type acoustic metamaterial which exhibits broadband negative effective density below a cutoff frequency. A lumped model is used to predict the behavior of the metamaterial, which verified by measurements. The plate-type metamaterial is then adopted to achieve a 2D hyperbolic metamaterial with hyperbolic dispersion relation. Numerical simulations and experiments are performed for partial focusing and subwavelength imaging. A complementary metamaterial is further proposed by combining these two structures, namely side holes and clamped plates, which shows extraordinary enhancement of sound transmission through aberrating layers. The designed structure is water based and is numerically verified to have applications in transcranial ultrasound.

For acoustic metasurfaces, we mainly use the labyrinthine structures with subwavelength features to achieve phase modulation across the metasurfaces. An asymmetric transmission device is proposed with two layers of metasurfaces. The device has a flat geometry and is easy for integration into larger scales. A 2D metasurface is further investigated based on the similar structure. Holographic reconstruction and multi-point

focusing are demonstrated both numerically and experimentally, which opens up new possibility in manipulating complex acoustic fields.

## 7.2 Future Work

To further explore the potentials of the acoustic metamaterials and metasurfaces, some future work is suggested based on the present dissertation:

1. Experimentally verify the side-branch based metamaterial with multiple branch openings, and investigate the capability of the integration of the structure into 2D scenarios.
2. The effect of material loss should be further investigated for the proposed complementary metamaterial, the working frequency and performance may be altered by introducing material loss, which is inevitable in practice. Experiments also need to be carried out to validate the design, other structures like labyrinthine metamaterial are also suggested for the design of complementary metamaterials.
3. More real world applications should be suggested for the hyperbolic acoustic metamaterial, like acoustic hyperlens which can work in nondestructive evaluation and imaging duties. The reliability and material loss of the structures should also be examined. For example, the non-uniformity of the plates may play an important role in various situations, the performance may be diminished.
4. The energy contrast and working frequency of the asymmetric transmission device needs to be further improved. The current design, although demonstrates the idea of utilizing acoustic metasurfaces for asymmetric transmission, has limited performance. The overall thickness of the device may be even thinner if alternative designs can be used.

5. Like has been suggested in chapter 6, the potential of acoustic metasurface hologram as acoustic levitation and computational devices deserves future investigation. It is expected that the metasurface hologram can achieve arbitrary control of transmitted acoustic waves.

## BIBLIOGRAPHY

1. Veselago, V. G. The electrodynamics of substances with simultaneously negative values of epsilon and  $\mu$ . *Sov. Phys. Uspekhi* **10**, 509–514 (1968).
2. Pendry, J., Holden, A., Stewart, W. & Youngs, I. Extremely low frequency plasmons in metallic microstructures. *Phys. Rev. Lett.* **76**, 4773–4776 (1996).
3. Pendry, J. B., Holden, A. J., Robbins, D. J. & Stewart, W. J. Magnetism from conductors and enhanced nonlinear phenomena. *IEEE Trans. Microw. Theory Tech.* **47**, 2075–2084 (1999).
4. Smith, D. R., Padilla, W. J., Vier, D. C., Nemat-Nasser, S. C. & Schultz, S. Composite Medium with Simultaneously Negative Permeability and Permittivity. *Phys. Rev. Lett.* **84**, 4184–4187 (2000).
5. Liu, Z., Zhang, X., Mao, Y., Zhu, Y. & Yang, Z. Locally resonant sonic materials. *Science* **289**, 1734–1736 (2000).
6. Ma, G. & Sheng, P. Acoustic metamaterials: From local resonances to broad horizons. *Sci. Adv.* **2**, e1501595 (2016).
7. Yu, N. & Capasso, F. Flat optics with designer metasurfaces. *Nat. Mater.* **13**, 139–50 (2014).
8. Li, J., Fok, L., Yin, X., Bartal, G. & Zhang, X. Experimental demonstration of an acoustic magnifying hyperlens. *Nat. Mater.* **8**, 931–4 (2009).
9. Zhu, J. *et al.* A holey-structured metamaterial for acoustic deep-subwavelength imaging. *Nat. Phys.* **7**, 52–55 (2011).
10. Zhang, S., Xia, C. & Fang, N. Broadband Acoustic Cloak for Ultrasound Waves. *Phys. Rev. Lett.* **106**, 024301 (2011).

11. Zigoneanu, L., Popa, B.-I. & Cummer, S. A. Three-dimensional broadband omnidirectional acoustic ground cloak. *Nat. Mater.* **13**, 352–5 (2014).
12. Shen, C. & Jing, Y. Side branch-based acoustic metamaterials with a broad-band negative bulk modulus. *Appl. Phys. A* **117**, 1885–1891 (2014).
13. Shen, C. *et al.* Broadband Acoustic Hyperbolic Metamaterial. *Phys. Rev. Lett.* **115**, 254301 (2015).
14. Shen, C. & Jing, Y. Loss-induced enhanced transmission in anisotropic density-near-zero acoustic metamaterials. *arXiv:1604.07272v1* 1–13 (2016).
15. Shen, C., Xu, J., Fang, N. X. & Jing, Y. Anisotropic Complementary Acoustic Metamaterial for Canceling out Aberrating Layers. *Phys. Rev. X* **4**, 041033 (2014).
16. Shen, C., Xie, Y., Li, J., Cummer, S. A. & Jing, Y. Asymmetric acoustic transmission through near-zero-index and gradient-index metasurfaces. *Appl. Phys. Lett.* **108**, 223502 (2016).
17. Xie, Y. *et al.* Acoustic Holographic Rendering with Two-dimensional Metamaterial-based Passive. *arXiv:1607.06014v1* 1–9 (2016).
18. Pendry, J. B. Negative refraction makes a perfect lens. *Phys. Rev. Lett.* **85**, 3966–9 (2000).
19. Shalaev, V. M. Optical negative-index metamaterials. *Nat. Photonics* **1**, 41–48 (2007).
20. Fang, N. *et al.* Ultrasonic metamaterials with negative modulus. *Nat. Mater.* **5**, 452–6 (2006).
21. Lee, S. H., Park, C. M., Seo, Y. M., Wang, Z. G. & Kim, C. K. Acoustic metamaterial with negative modulus. *J. Phys. Condens. Matter* **21**, 175704 (2009).

22. Lee, S. H., Park, C. M., Seo, Y. M., Wang, Z. G. & Kim, C. K. Composite Acoustic Medium with Simultaneously Negative Density and Modulus. *Phys. Rev. Lett.* **104**, 054301 (2010).
23. Bongard, F., Lissek, H. & Mosig, J. R. Acoustic transmission line metamaterial with negative/zero/positive refractive index. *Phys. Rev. B* **82**, 094306 (2010).
24. Kinsler, L. E., Frey, A. U., Coppens, A. B. & Sanders, J. V. *Fundamentals of Acoustics*. (Wiley, 1982).
25. Pierce, A. D. *Acoustics: An Introduction to Its Physical Principles and Applications*. (Acoustical Society of America, 1989).
26. Cheng, Y., Xu, J. & Liu, X. One-dimensional structured ultrasonic metamaterials with simultaneously negative dynamic density and modulus. *Phys. Rev. B* **77**, 045134 (2008).
27. Fokin, V., Ambati, M., Sun, C. & Zhang, X. Method for retrieving effective properties of locally resonant acoustic metamaterials. *Phys. Rev. B* **76**, 144302 (2007).
28. Yang, Z., Mei, J., Yang, M., Chan, N. & Sheng, P. Membrane-Type Acoustic Metamaterial with Negative Dynamic Mass. *Phys. Rev. Lett.* **101**, 204301 (2008).
29. Lee, S. H., Park, C. M., Seo, Y. M., Wang, Z. G. & Kim, C. K. Acoustic metamaterial with negative density. *Phys. Lett. A* **373**, 4464–4469 (2009).
30. Liang, Z. & Li, J. Extreme Acoustic Metamaterial by Coiling Up Space. *Phys. Rev. Lett.* **108**, 114301 (2012).
31. Huang, T.-Y., Shen, C. & Jing, Y. Membrane- and plate-type acoustic metamaterials. *J. Acoust. Soc. Am.* **139**, 3240–3250 (2016).

32. Huang, T., Shen, C. & Jing, Y. On the evaluation of effective density for plate- and membrane-type acoustic metamaterials I . Introduction. *J. Acoust. Soc. Am.* **140**, 908–916 (2016).
33. Leissa, A. W. *Vibration of Plates. Vibration of Plates* (NASA SP-160, 1969).
34. Xu, X., Li, P., Zhou, X. & Hu, G. Experimental study on acoustic subwavelength imaging based on zero-mass metamaterials. *EPL (Europhysics Lett.)* **109**, 28001 (2015).
35. Ao, X. & Chan, C. T. Far-field image magnification for acoustic waves using anisotropic acoustic metamaterials. *Phys. Rev. E* **77**, 025601 (2008).
36. Lu, D. & Liu, Z. Hyperlenses and metalenses for far-field super-resolution imaging. *Nat. Commun.* **3**, 1205 (2012).
37. Poddubny, A., Iorsh, I., Belov, P. & Kivshar, Y. Hyperbolic metamaterials. *Nat. Photonics* **7**, 948–957 (2013).
38. Christensen, J. & Garc ía de Abajo, F. Anisotropic metamaterials for full control of acoustic waves. *Phys. Rev. Lett.* **108**, 124301 (2012).
39. Garc ía-Chocano, V. M., Christensen, J. & S áncchez-Dehesa, J. Negative Refraction and Energy Funneling by Hyperbolic Materials: An Experimental Demonstration in Acoustics. *Phys. Rev. Lett.* **112**, 144301 (2014).
40. Park, C. M. *et al.* Amplification of Acoustic Evanescent Waves Using Metamaterial Slabs. *Phys. Rev. Lett.* **107**, 194301 (2011).
41. Smith, D. R., Schurig, D., Mock, J. J., Kolinko, P. & Rye, P. Partial focusing of radiation by a slab of indefinite media. *Appl. Phys. Lett.* **84**, 2244 (2004).
42. Smith, D. & Schurig, D. Electromagnetic Wave Propagation in Media with

- Indefinite Permittivity and Permeability Tensors. *Phys. Rev. Lett.* **90**, 077405 (2003).
43. Zhou, X. & Hu, G. Superlensing effect of an anisotropic metamaterial slab with near-zero dynamic mass. *Appl. Phys. Lett.* **98**, 263510 (2011).
  44. Liu, C., Xu, X. & Liu, X. Manipulating acoustic flow by using inhomogeneous anisotropic density-near-zero metamaterials. *Appl. Phys. Lett.* **106**, 081912 (2015).
  45. Gu, Y., Cheng, Y. & Liu, X. Acoustic planar hyperlens based on anisotropic density-near-zero metamaterials. *Appl. Phys. Lett.* **107**, 133503 (2015).
  46. Fleury, R. & Alù, A. Extraordinary Sound Transmission through Density-Near-Zero Ultranarrow Channels. *Phys. Rev. Lett.* **111**, 055501 (2013).
  47. Feng, S. Loss-induced omnidirectional bending to the normal in  $\epsilon$ -near-zero metamaterials. *Phys. Rev. Lett.* **108**, 193904 (2012).
  48. Sun, L., Feng, S. & Yang, X. Loss enhanced transmission and collimation in anisotropic epsilon-near-zero metamaterials. *Appl. Phys. Lett.* **101**, 241101 (2012).
  49. Ambati, M., Fang, N., Sun, C. & Zhang, X. Surface resonant states and superlensing in acoustic metamaterials. *Phys. Rev. B* **75**, 195447 (2007).
  50. Schurig, D. & Smith, D. R. Spatial filtering using media with indefinite permittivity and permeability tensors. *Appl. Phys. Lett.* **82**, 2215 (2003).
  51. Kadic, M., Bückmann, T., Schittny, R. & Wegener, M. Metamaterials beyond electromagnetism. *Reports Prog. Phys.* **76**, 126501 (2013).
  52. Cummer, S. A., Christensen, J. & Alù, A. Controlling sound with acoustic metamaterials. *Nat. Rev. Mater.* **1**, 16001 (2016).
  53. Pendry, J. & Ramakrishna, S. Focusing light using negative refraction. *J. Phys.*

- Condens. Matter* **15**, 6345–6364 (2003).
54. Lai, Y., Chen, H., Zhang, Z.-Q. & Chan, C. Complementary Media Invisibility Cloak that Cloaks Objects at a Distance Outside the Cloaking Shell. *Phys. Rev. Lett.* **102**, 093901 (2009).
  55. Lai, Y. *et al.* Illusion Optics: The Optical Transformation of an Object into Another Object. *Phys. Rev. Lett.* **102**, 253902 (2009).
  56. Zhu, X., Liang, B., Kan, W., Zou, X. & Cheng, J. Acoustic Cloaking by a Superlens with Single-Negative Materials. *Phys. Rev. Lett.* **106**, 014301 (2011).
  57. Liu, B. & Huang, J. P. Acoustically conceal an object with hearing. *Eur. Phys. J. Appl. Phys.* **48**, 20501 (2009).
  58. Yang, J., Huang, M., Yang, C., Peng, J. & Chang, J. An external acoustic cloak with N-sided regular polygonal cross section based on complementary medium. *Comput. Mater. Sci.* **49**, 9–14 (2010).
  59. Demirli, R., Amin, M. G., Shen, X. & Zhang, Y. D. Ultrasonic Flaw Detection and Imaging through Reverberant Layers via Subspace Analysis and Projection. *Adv. Acoust. Vib.* **2012**, 1–10 (2012).
  60. Jing, Y., Meral, F. C. & Clement, G. T. Time-reversal transcranial ultrasound beam focusing using a k-space method. *Phys. Med. Biol.* **57**, 901–917 (2012).
  61. Wang, T. & Jing, Y. Transcranial ultrasound imaging with speed of sound-based phase correction: a numerical study. *Phys. Med. Biol.* **58**, 6663–81 (2013).
  62. Clement, G. T. & Hynynen, K. A non-invasive method for focusing ultrasound through the human skull. *Phys. Med. Biol.* **47**, 1219–36 (2002).
  63. Pernot, M. *et al.* In vivo transcranial brain surgery with an ultrasonic time reversal

- mirror. *J. Neurosurg.* **106**, 1061–6 (2007).
64. Chen, H. & Chan, C. T. Acoustic cloaking and transformation acoustics. *J. Phys. D. Appl. Phys.* **43**, 113001 (2010).
  65. Pendry, J. B., Schurig, D. & Smith, D. R. Controlling electromagnetic fields. *Science* **312**, 1780–1782 (2006).
  66. Leonhardt, U. Optical conformal mapping. *Science* **312**, 1777–1780 (2006).
  67. Chen, H. & Chan, C. T. Acoustic cloaking in three dimensions using acoustic metamaterials. *Appl. Phys. Lett.* **91**, 183518 (2007).
  68. Popa, B.-I. & Cummer, S. A. Homogeneous and compact acoustic ground cloaks. *Phys. Rev. B* **83**, 224304 (2011).
  69. Akl, W. & Baz, a. Active Acoustic Metamaterial With Simultaneously Programmable Density and Bulk Modulus. *J. Vib. Acoust.* **135**, 031001 (2013).
  70. Wang, Y. *et al.* Applications of antireflection coatings in sonic crystal-based acoustic devices. *Phys. Lett. A* **375**, 1348–1351 (2011).
  71. Haldane, F. D. M. & Raghu, S. Possible realization of directional optical waveguides in photonic crystals with broken time-reversal symmetry. *Phys. Rev. Lett.* **100**, 013904 (2008).
  72. Li, B., Wang, L. & Casati, G. Thermal diode: Rectification of heat flux. *Phys. Rev. Lett.* **93**, 1–4 (2004).
  73. Fleury, R., Sounas, D. L., Sieck, C. F. & Haberman, M. R. Sound Isolation and Giant Linear Nonreciprocity in a Compact Acoustic Circulator. *Science* **343**, 516–519 (2014).
  74. Liang, B., Guo, X. S., Tu, J., Zhang, D. & Cheng, J. C. An acoustic rectifier. *Nat.*

- Mater.* **9**, 989–992 (2010).
75. Zhu, Y.-F. F., Zou, X.-Y. Y., Liang, B. & Cheng, J.-C. C. Acoustic one-way open tunnel by using metasurface. *Appl. Phys. Lett.* **107**, 113501 (2015).
  76. Yu, N. *et al.* Light Propagation with Phase Discontinuities: Generalized Laws of Reflection and Refraction. *Science* **334**, 333–337 (2011).
  77. Maznev, A. A., Every, A. G. & Wright, O. B. Reciprocity in reflection and transmission: What is a ‘phonon diode’? *Wave Motion* **50**, 776–784 (2013).
  78. Zhai, S. *et al.* Manipulation of transmitted wave front using ultrathin planar acoustic metasurfaces. *Appl. Phys. A* **120**, 1283–1289 (2015).
  79. Xie, Y., Popa, B.-I., Zigoneanu, L. & Cummer, S. A. Measurement of a Broadband Negative Index with Space-Coiling Acoustic Metamaterials. *Phys. Rev. Lett.* **110**, 175501 (2013).
  80. Xie, Y. *et al.* Wavefront modulation and subwavelength diffractive acoustics with an acoustic metasurface. *Nat. Commun.* **5**, 5553 (2014).
  81. Ward, G. P. *et al.* Boundary-Layer Effects on Acoustic Transmission Through Narrow Slit Cavities. *Phys. Rev. Lett.* **115**, 044302 (2015).
  82. Li, Y., Jiang, X., Liang, B., Cheng, J. & Zhang, L. Metascreen-Based Acoustic Passive Phased Array. *Phys. Rev. Appl.* **4**, 024003 (2015).
  83. Li, Y. & Assouar, M. B. Three-dimensional collimated self-accelerating beam through acoustic metascreen. *Sci. Rep.* **5**, 17612 (2015).
  84. Collier, R. *Optical Holography*. (Elsevier, 2013).
  85. Maynard, J. D., Williams, E. G. & Lee, Y. Nearfield Acoustic Holography: I - Theory of Generalized Holography and the Development of NAH. *J. Acoust. Soc.*

- Am.* **78**, 1395–1413 (1985).
86. Larouche, S., Tsai, Y.-J., Tyler, T., Jokerst, N. M. & Smith, D. R. Infrared metamaterial phase holograms. *Nat. Mater.* **11**, 450–454 (2012).
  87. Ni, X., Kildishev, A. V & Shalaev, V. M. Metasurface holograms for visible light. *Nat. Commun.* **4**, 2807 (2013).
  88. Zheng, G. *et al.* Metasurface holograms reaching 80% efficiency. *Nat. Nanotechnol.* **10**, 308–12 (2015).
  89. Leonardo, R. Di, Ianni, F. & Ruocco, G. Computer generation of optimal holograms for optical trap arrays. *Opt. Express* **15**, 299–308 (2007).
  90. Williams, E. G. *Fourier acoustics: sound radiation and nearfield acoustical holography*. (Academic press, 1999).
  91. Li, Y., Liang, B., Gu, Z., Zou, X. & Cheng, J. Reflected wavefront manipulation based on ultrathin planar acoustic metasurfaces. *Sci. Rep.* **3**, 2546 (2013).
  92. Li, Y. *et al.* Three-dimensional Ultrathin Planar Lenses by Acoustic Metamaterials. *Sci. Rep.* **4**, 6830 (2014).
  93. Zhang, P. *et al.* Generation of acoustic self-bending and bottle beams by phase engineering. *Nat. Commun.* **5**, 4316 (2014).
  94. Marzo, A. *et al.* Holographic acoustic elements for manipulation of levitated objects. *Nat. Commun.* **6**, 8661 (2015).
  95. Silva, A. *et al.* Performing Mathematical Operations with Metamaterials. *Science* **343**, 160–164 (2014).

## APPENDICES

A. Description of the finite difference method for the effective density and compressibility of acoustic metamaterials

Consider 2D acoustic waves traveling in the x-y plane, for acoustic processes with small amplitudes, the acoustic pressure and particle velocity have the following relationship<sup>24</sup>:

$$\frac{\partial p}{\partial x} = -j\omega\rho_x u_x \quad (\text{A.1})$$

$$\frac{\partial p}{\partial y} = -j\omega\rho_y u_y \quad (\text{A.2})$$

$$\frac{\partial u_x}{\partial x} + \frac{\partial u_y}{\partial y} = \frac{-j\omega p}{B} \quad (\text{A.3})$$

Here  $p$  is the acoustic pressure,  $\omega$  is the angular frequency,  $B$  is the bulk modulus of the medium,  $\rho_{x,y}$ ,  $u_{x,y}$  are the densities and particle velocities along x- and y-directions, respectively.

As discussed in chapters 3 and 4, for plate-type acoustic metamaterials, the effective properties can be estimated separately along orthogonal directions, here we focus on waves in the x-direction only. For a unit cell of plate-type acoustic metamaterial shown in Fig. A.1 with dimension  $d$  much smaller than the wavelength of interest, Eq. (A.1) can be expressed with a finite-difference approximation:

$$\frac{\Delta p}{d} = -j\omega\rho_x V \quad (\text{A.4})$$

where  $\Delta p = p_2 - p_1$  is the pressure difference across the unit cell,  $V$  is the average transverse velocity of the plate. These values can be estimated by finite element analysis using COMSOL. Note that both real and imaginary part of  $p_1$ ,  $p_2$  and  $V$  should be included in order to get accurate results.

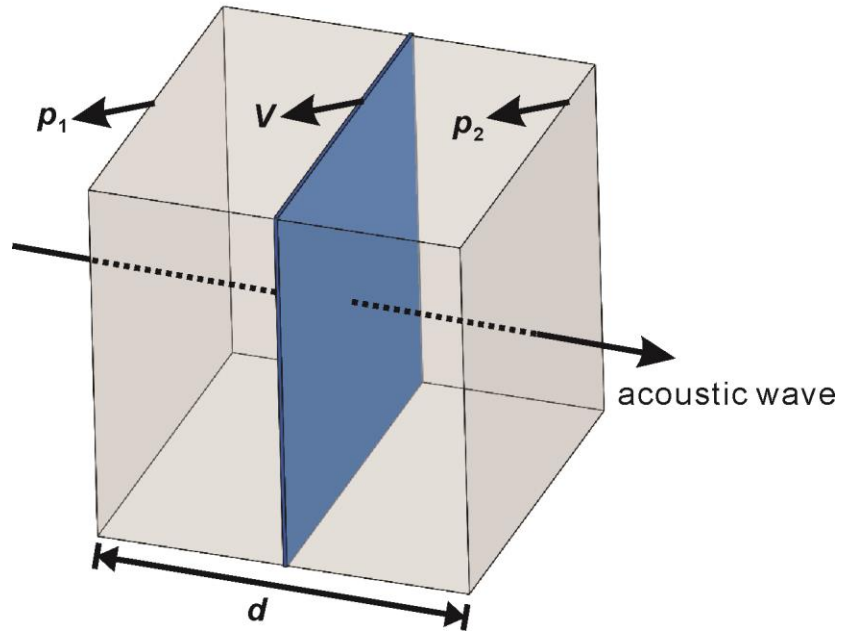


Figure A.1 Unit cell of a plate-type acoustic metamaterial for calculating effective density.

The effective density along the x-direction is therefore obtained by:

$$\rho_x = \frac{\Delta p}{d} \frac{j}{\omega V} \quad (\text{A.5})$$

The bulk modulus of the unit cell can be calculated using the same procedure. The unit cell for calculating effective bulk modulus is illustrated in Fig. A.2, where two plates are on the two sides of the unit cell.

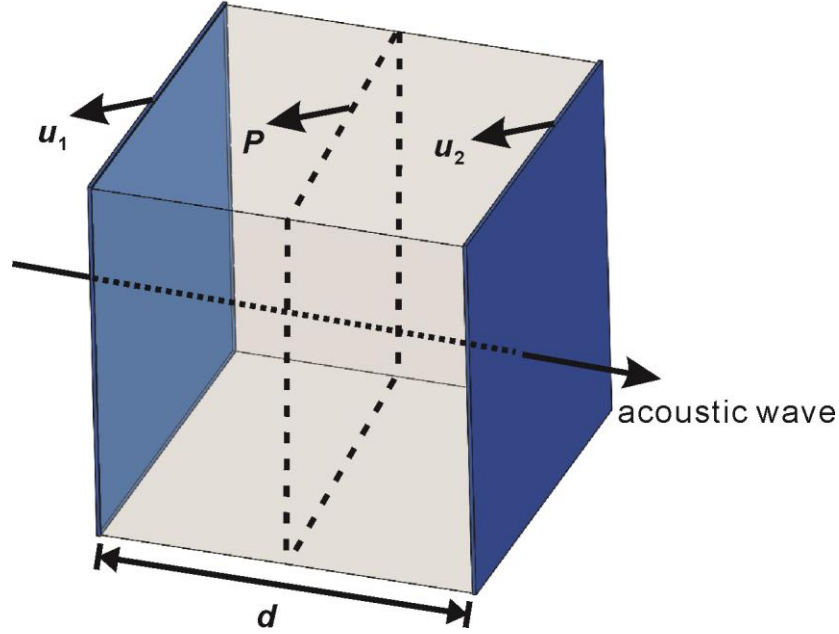


Figure A.2 Unit cell of a plate-type acoustic metamaterial for calculating effective bulk modulus.

The finite difference approximation of Eq. (A.3) in 1D case (x-direction) can be expressed as:

$$\frac{\Delta u}{d} = \frac{-j\omega P}{B} \quad (\text{A.6})$$

where  $\Delta u = u_2 - u_1$  is the transverse velocity difference across the unit cell,  $P$  is the average pressure on the mid-plane of the unit cell. Again, these values can be estimated numerically using COMSOL, and both real and imaginary parts should be taken into account.

Finally the effective bulk modulus of the medium is written as:

$$B = \frac{-j\omega P d}{\Delta u} \quad (\text{A.7})$$

## B. Band structure of 2D acoustic metamaterial lattice

The band structure of an acoustic metamaterial lattice shows the bandgap and wave behavior inside the acoustic metamaterial. For the plate-type acoustic metamaterial described in chapter 3, the metamaterial slab has a rectangular lattice, with center located at the  $\Gamma$  point. Numerical simulations based on COMSOL are used to calculate the band structure of the rectangular lattice. Figure B.1 shows the COMSOL geometry of a single unit cell, the blue regions represent the plates (fixed on the four sides), note that for the single unit cell, the thickness of the plates is set to be half of the real thickness because of periodicity.

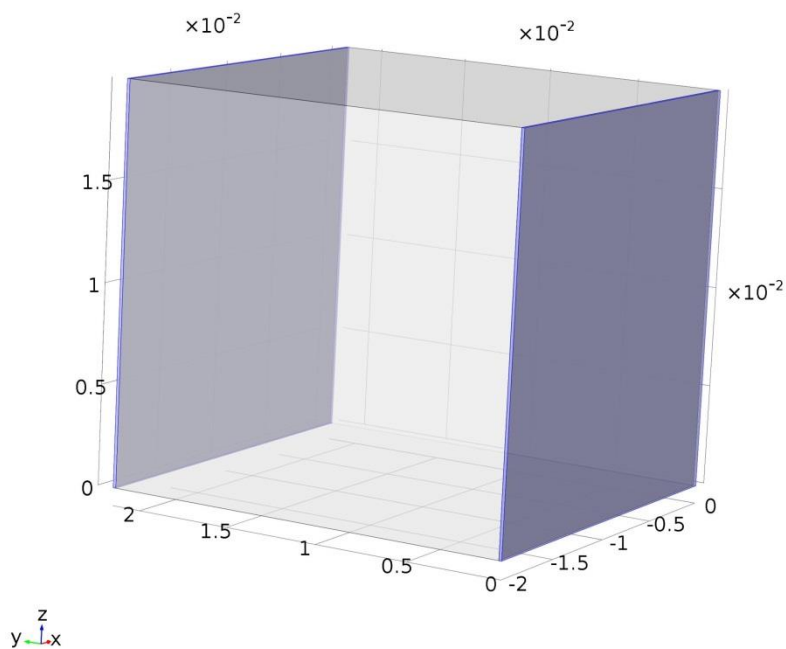


Figure B.1 Geometry of the unit cell in COMSOL. Unit: m.

To study the band structure of the unit cell, Floquet boundary conditions on two sides of the unit should be used. The COMSOL setting of the Floquet boundary conditions is given in Fig. B.2, where the  $k$ -vectors of Floquet periodicity are:

$$k_x = k_1 \frac{2\pi}{a_x} \quad (\text{B.1})$$

$$k_y = k_2 \frac{2\pi}{a_y} \quad (\text{B.2})$$

where  $a_x = 21.6$  mm and  $a_y = 20$  mm are the periodicity in the x- and y-directions, respectively. The band structure of the unit cell can then be obtained by calculating the eigenfrequencies of the unit cell with varying the values of  $k_1$  and  $k_2$  from 0 to 0.5. The settings of the sweeping study is shown in Fig. B.3.

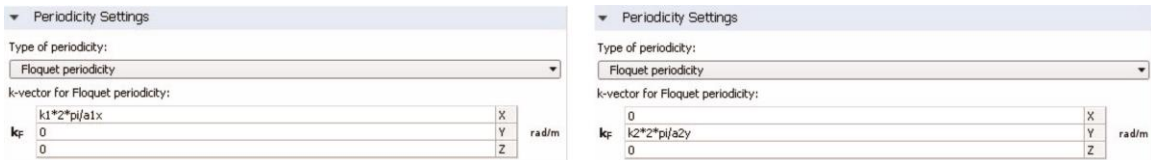


Figure B.2 Boundary conditions of the unit cell.

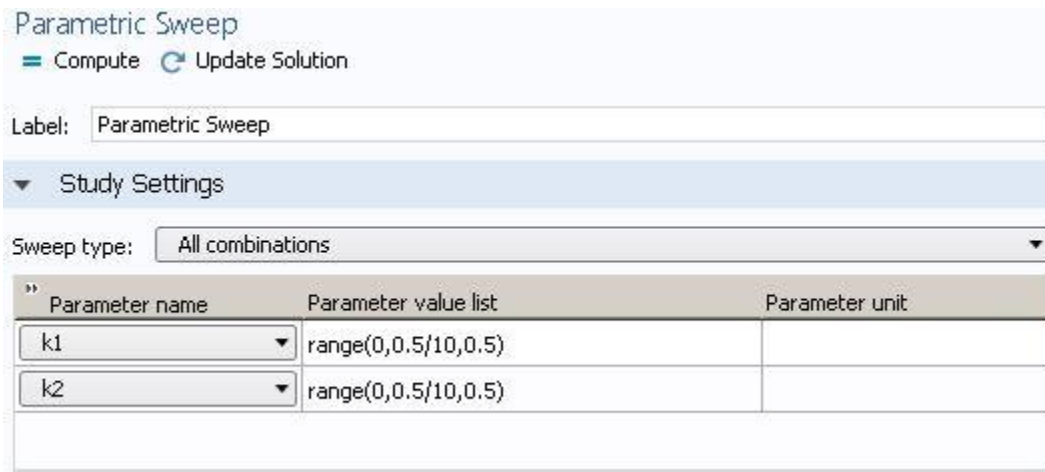


Figure B.3 Setting of the parametric sweep study in COMSOL.

The retrieved band structure is depicted in Fig. B.4, where the inset illustrates the directions in the unit cell. The eigenfrequency of 0 Hz points are omitted as they do not have physical meaning. The blank space where no eigenfrequency exist represents a bandgap. It can be seen that for the plate-type acoustic metamaterial under study here, the band structure match well with the theory outlined in chapter 3.

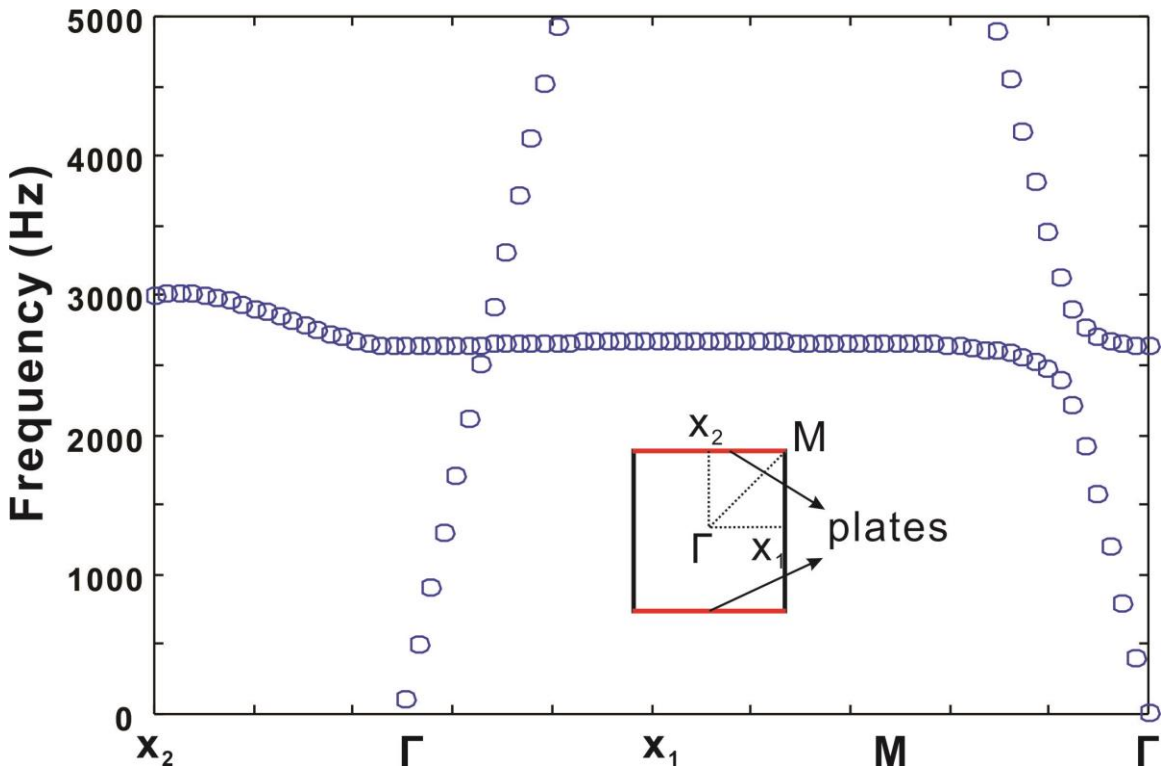


Figure B.4 Band structure of a plate-type acoustic metamaterial unit cell.

### C. Description of the inverse method for the properties of acoustic metamaterials

For other types of acoustic metamaterials, like the labyrinthine metamaterial described in chapters 5 and 6, the acoustic properties can be retrieved using an inverse method by analyzing the transmission and reflection coefficients of a single unit cell.

Consider a labyrinthine metamaterial unit shown in Fig. B.3, a plane incident wave  $I$  propagates normally to the unit cell, with reflection and transmission coefficients be  $R$  and  $T$ , respectively. Let the background medium to be air with density and speed of sound  $\rho_0$  and  $c_0$ , the unit cell be homogenized with properties  $\rho_{eff}$  and  $c_{eff}$ , the reflection and transmission coefficients can be written as<sup>27</sup>:

$$R = \frac{Z^2 - Z_0^2}{Z_0^2 + Z^2 + 2jZ_0Z \cot \phi} \quad (C.1)$$

$$T = \frac{1 + R}{\cos \phi - \frac{jZ \sin \phi}{Z_0}} \quad (C.2)$$

where  $Z_0 = \rho_0 c_0$ ,  $Z = \rho_{eff} c_{eff}$  are the characteristic impedances of the background medium and the unit cell, respectively,  $\phi = 2\pi f d / c_{eff}$  is the phase change across the layer,  $f$  is the frequency,  $d$  is the thickness of the unit.

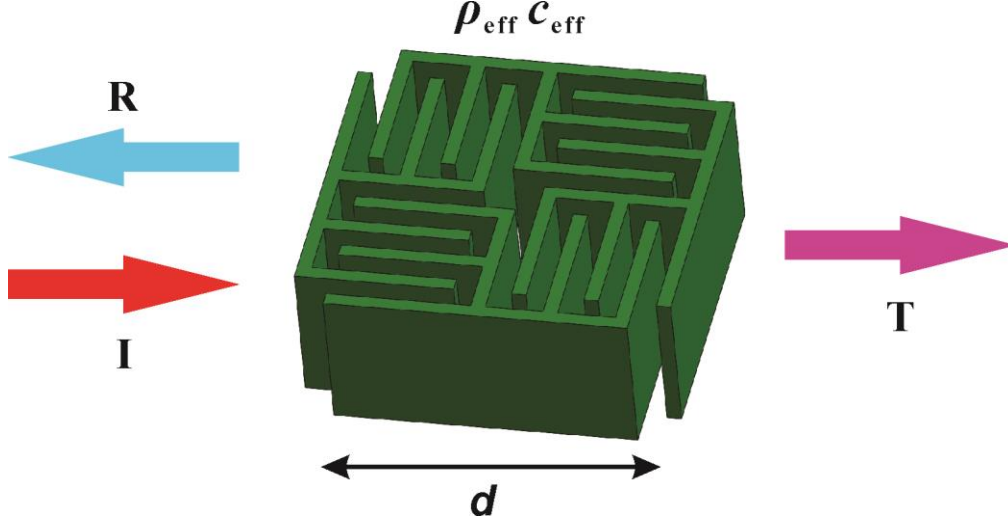


Figure C.1 Unit cell of a labyrinthine acoustic metamaterial.

Introducing the unit-free factor  $n = c_0 / c_{eff}$ ,  $\xi = Z / Z_0$ , Eq. (C.1) and Eq. (C.2) can be rewritten to retrieve these values<sup>27</sup>:

$$\xi = \frac{r}{1 - 2R + R^2 - T^2} \quad (C.3)$$

$$n = \frac{-j \ln x + 2\pi m}{kd} \quad (C.4)$$

where  $m$  is the branch number of the function  $\cos^{-1}\left(\frac{1 - R^2 + T^2}{2T}\right)$ ,  $k = \omega / c_0$  is the wave

vector,  $r$  and  $x$  are given by:

$$r = \mp \sqrt{(R^2 - T^2 - 1)^2 - 4T^2} \quad (C.5)$$

$$x = \frac{1 - R^2 + T^2 + r}{2T} \quad (C.6)$$

The sign of  $r$  should be chosen such that  $\text{Re}(\xi)$  is positive to be physically meaningful.

In practice, the reflection and transmission coefficients can be obtained by numerical

simulations. Since the size of the unit cell is much smaller than the wavelength,  $m$  is typically zero, for thick metamaterial slabs, however,  $m$  can have finite values as integers.

The effective density  $\rho_{eff}$  and effective speed of sound  $c_{eff}$  for the metamaterial unit can therefore be obtained by:

$$\rho_{eff} = \rho_0 n \xi \quad (C.7)$$

$$c_{eff} = \frac{c_0}{n} \quad (C.8)$$

The effective refractive index  $n$  can be calculated by Eq. (C.4).